Finite Element Modelling of Corrosion Damaged Reinforced Concrete Structures

by

Siavash Habibi

A thesis submitted in conformity with the requirements
For the degree of Master of Applied Science
Civil Engineering
University of Toronto

Finite Element Modelling of Corrosion Damaged Reinforced Concrete Structures

Siavash Habibi

Master of Applied Science

Graduate Department of Civil Engineering
University of Toronto
2017

Abstract

Corrosion of reinforcing steel is the predominant deterioration mechanism of reinforced concrete structures throughout the world. This thesis presents the work performed on VecTor2, a nonlinear finite element analysis (NLFEA) program developed at the University of Toronto, for analysis of corrosion damaged reinforced concrete structures. Two well-known types of corrosion, namely uniform and pitting, were considered for modelling. Corrosion damage was incorporated in the algorithms of VecTor2 through reduction of the sectional area of reinforcing steel, the bond strength between the reinforcement and concrete, and the mechanical properties such as yield strength of a corroded reinforcing bar. Cracking of the cover concrete due to corrosion was also introduced into the finite element models by inducing tensile strains in the concrete elements in the immediate vicinity of a corroded truss element.

The employed techniques for incorporating corrosion damage in VecTor2 successfully reproduced the load-deflection response of published experiments on corroded reinforced concrete beams. Stochastic simulation of the same beams, performed by employing the stochastic tools of VecTor2, demonstrated the sensitivity of response quantities such as the failure load to changes in various input parameters. Such information forms the basis for further research and future work. The statistics of the response quantities can also be used for reliability analysis by employing methods like the first order reliability method (FORM).

Acknowledgements

First and foremost, I would like to thank my supervisor, Professor Frank J. Vecchio, for his guidance and support throughout my studies. His expert advice, patience and approachability made this an enjoyable experience. I am grateful for the opportunity he provided me with. Working under his supervision has had a big impact on me which truly enriched me technically and personally. I would also like to thank Professor Fae Azhari for her valuable advice towards my work.

Next I would like to show my gratitude to my fellow research group members and friends at the University of Toronto for their friendship and help. They include Saif Shaban, Farhad Habibi, Vahid Sadeghian, Anca Jurcut, Bernard Isojeh, Simon Liu, Stamatina Chasioti, Mark Hunter, Andac Lulec, Raymond Ma, Olesya Zhychkovska, Natasa Jeremic, Zahra Kharal, and Sahar Hamedi. I am indebted to Saif Shaban, who as a colleague and a good friend, was always willing to read and review my thesis and give his best suggestions for improvement of my work.

Last but not the least, I would like to thank my family for their encouragement and understanding throughout my studies. Especially Mina Rahbarnejad for her unconditional love and endless patience. This thesis would not have been completed without their support.

Table of Contents

List of Tables

List of Figures

1 Introduction

1.1 Background

Reinforced concrete is a widely used construction material for bridges, buildings and platforms as well as many underground structures such as tunnels and pipelines (Bohni, 2005). In general, it is a durable, relatively cheap, and versatile material capable of withstanding severe environments. However, concrete deterioration can take place for a variety of reasons such as alkali-aggregate reactivity, freeze-thaw, and corrosion of the embedded steel reinforcement. Degradation of reinforced concrete structures caused by the aforementioned processes results in decreased performance with time which might be of concern for the government, owners, and engineers.

According to a U.S. Federal Highway Association (FHWA) report on U.S. concrete bridges in 1998, from the 581,862 bridges surveyed, about 101,518 were structurally deficient (FHWA-RD-98-088). While corrosion of the reinforcing steel was not the only cause of the deficiencies, it is now widely accepted that it is the major cause of deterioration of reinforced concrete structures. A more recent study by Koch et al. (2002) stated that 15% of the U.S. bridges are structurally deficient because of corroded steel. The annual direct cost of corrosion was estimated to be $8.3 billion, which includes replacement or maintenance of the deficient bridges. The indirect cost, such as traffic delays, was estimated to be 10 times that of the direct cost (Koch et al., 2002). In Canada, a total of $74 billion is required to restore the deteriorated reinforced concrete infrastructure back to its original state (NSERC 2012). Therefore, from an economic point of view, corrosion of reinforcement in concrete structures is a costly problem.

The high alkalinity of concrete pore solution (pH of 12 to 13), due to the presence of calcium hydroxide ($Ca(OH)_2$) in the cement paste, naturally protects the reinforcement from corrosion. At this high pH, a passive film (i.e. a thin layer of Fe_2O_3) forms around the reinforcement which insulates the steel and protects it from corrosion. Two processes that can disrupt this passive film are carbonation of concrete and chloride attack. Carbon dioxide in the atmosphere reacts with the concrete pore water alkali according to the following reactions:

$$\mathrm{CO_2 + H_2O \rightarrow H_2CO_3}$$

$$\mathrm{Ca(OH)_2 + H_2CO_3 \rightarrow CaCO_3 + 2H_2O}$$

which reduce the pore water pH to about 8, at which point the passive oxide layer becomes unstable. On the other hand, chloride ions, which come from several sources, act as catalysts to the corrosion reaction, facilitating the breakdown of the passive layer and initiating the corrosion process. (Broomfield, 2002). They can be introduced into concrete due to the use of saline water in the mix, addition of calcium chloride ($CaCl_2$) as a set accelerator, or use of contaminated aggregates. They can also diffuse into concrete due to sea salt spray, de-icing salt, or direct seawater wetting.

The corrosion process consists of two coupled electrochemical reactions, known as half-cell cathodic and anodic reactions. Iron is transformed from Fe to Fe^{2+} in the anodic reaction (oxidation of iron) whereas in the cathodic reaction the liberated electrons are consumed by oxygen in the presence of water (reduction of oxygen) as shown in Figure 1.1. The rates at which the anodic and cathodic reactions occur are equilibrated by each other. In the case of chloride attack, the reaction sites are spatially separated, forming a macrocell. In contrast, carbonation tends to be on a microcell level with uniformly distributed corrosion sites all around the perimeter and along the length of a reinforcing bar.

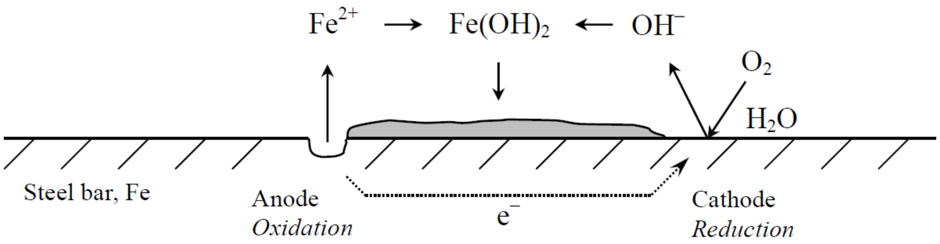

Figure 1.1: A schematic illustration of a steel corrosion in concrete. Taken from Markeset and Myrdal (2008)

1.2 Research significance

The serviceability and durability of reinforced concrete structures can be seriously affected by the cracking of the cover concrete caused by corrosion (Richard et al., 2010). Corrosion can also affect the strength by reducing the cross-sectional area of reinforcing steel. The degree to which the structural performance is degraded depends on the nature and severity of corrosion and the location of its occurrence. Considering the great number of old and defective reinforced concrete structures that are present within our built environment, there is a considerable need for reliable tools to assess the effects of corrosion on the behaviour of reinforced concrete (Kallias and Rafiq, 2010). In recent years, considerable research has been devoted to the development of structural deterioration models, which can be used throughout the whole life-performance assessment of corrosion-affected reinforced concrete structures. The focal point in the structural modelling of corrosion is the consideration of its physical effects on the materials and structural behaviour, illustrated graphically in Figure 1.2. In detail, the following aspects should be considered (Coronelli and Gambarova, 2004):

- Steel area reduction in the main longitudinal bars and stirrups
- Changes in the ductility of reinforcing steel bars due to pitting corrosion
- Reduction of concrete cover due to cracking or spalling
- Changes in strength and ductility of concrete in compression, because of micro-cracking induced by corrosion of the reinforcing bars
- Changes in tension stiffening because of cover cracking and bond deterioration
- Changes in the bond between the reinforcing bars and concrete

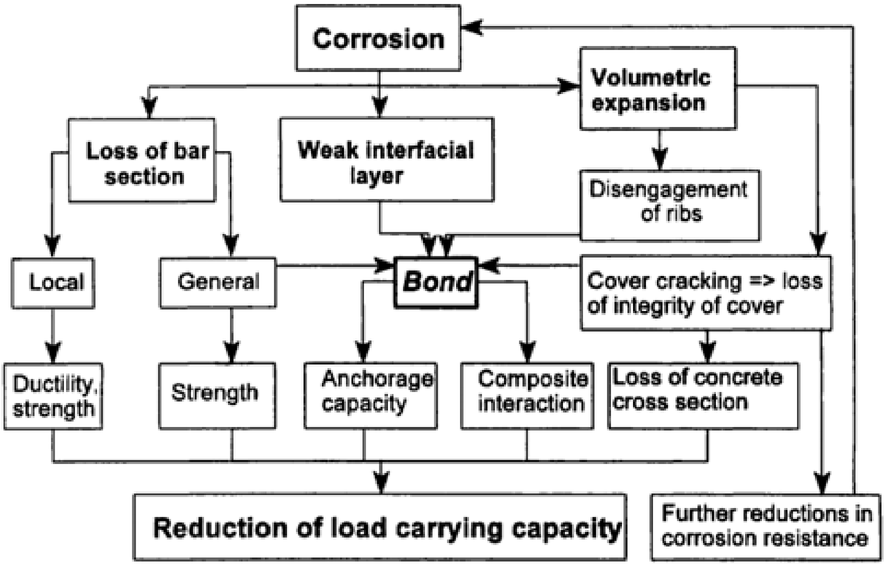

Figure 1.2: Effects of corrosion on reinforced concrete structures. Taken from fib Bulletin No. 10 (2000)

One of the tools that can assist in drawing proper conclusions on the state of a corroded reinforced concrete structure is finite element modelling. The VecTor programs, developed at the University of Toronto, are nonlinear finite element programs capable of analyzing beam sections (VecTor1), two-dimensional membrane structures (VecTor2), three-dimensional solid structures (VecTor3), plates and shells (VecTor4), plane frames (VecTor5), and axisymmetric solids (VecTor6). In light of the current development of numerical models for corrosion damage, the research presented in this thesis implements corrosion damage constitutive models within the algorithms of VecTor2. Utilizing the implemented formulation, the shortcomings of the existing models are identified and recommendations for future work are developed.

1.3 Outline of the thesis

Chapter 1 presented an overview of the corrosion reaction and the damage it causes to the reinforced concrete structures. The general scope and objectives of the research were also outlined.

Chapter 2 presents a review of the experimental and analytical literature related to the corrosion of reinforced concrete structures. The chapter begins with a brief overview of the electrochemistry of metallic corrosion followed by empirical models of corrosion rate found in literature. Fundamental mechanisms through which corrosion damages a reinforced concrete structure are also discussed. The chapter concludes with a discussion of the gaps in the literature.

Chapter 3 provides a detailed discussion of the formulations added to VecTor2 along with material-level verification studies and sample calculations. The presented models cover the key aspects related to this research project.

Chapter 4 presents the finite element modelling of four experimental series, carried out by other researchers, in VecTor2. The implementation of the formulations presented in Chapter 3 is validated by comparing the results obtained from VecTor2 with the experimental results.

Chapter 5 presents the stochastic modelling of corroded reinforced concrete beams through which the uncertainties associated with uniform and pitting corrosion are incorporated into finite element analysis. Based on experimental data found in literature, the characteristic parameters of a Gaussian random field defining the spatial variations of steel cross-sectional loss are quantified. Lastly, the accuracy and general applicability of the employed stochastic techniques are examined.

Chapter 6 closes the thesis with conclusions and recommendations for future work.

2 Literature Review

This chapter presents a literature review on the corrosion of steel reinforcement in reinforced concrete structures. To investigate the important aspects of finite element modelling of corrosion, the basic electrochemistry of corrosion reaction followed by a background summary of experiments and finite element models related to the key objective are briefly presented. Based on the reviewed literature, the effects of corrosion on mechanical properties and flexural response of reinforced concrete members are identified.

2.1 Electrochemistry of corrosion

The corrosion of steel in concrete is an electrochemical reaction that consists of two half-cell reactions as follows:

- Anodic reaction: $2\mathrm{Fe} \rightarrow 2\mathrm{Fe}^{2} + 4\mathrm{e}^{-}$
- Cathodic reaction: $\mathrm{O}_2 + 2\mathrm{H}_2\mathrm{O} + 4\mathrm{e}^{-} \rightarrow 4\mathrm{OH}^{-}$
- Sum of the reactions: $2\mathrm{Fe} + 2\mathrm{H}_2\mathrm{O} + \mathrm{O}_2 \rightarrow 2\mathrm{Fe}(\mathrm{OH})_2$

In order for the anodic reaction to occur, the passivity of the reinforcing bar should be broken down by carbonation or chloride attack. The cathodic reaction takes place in the presence of sufficient moisture and oxygen. These reactions involve the transfer of electrons and ions between the anode and cathode. Hence, a well-conductive environment or electrolyte should exist between the anodic and cathodic reaction sites to facilitate the flux of ions. Likewise, a metallic connection should exist to make possible the flux of electrons. In reinforced concrete, the concrete and reinforcing bar serve as the electrolyte and metallic connection, respectively. The necessary components of the corrosion reaction are graphically depicted in Figure 2.1.

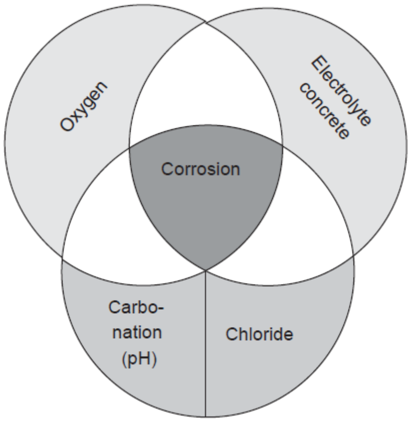

Figure 2.1: Components of the corrosion reaction. Taken from Bohni (2005)

The corrosion process occurs at a rate determined by an equilibrium between the anodic and cathodic reactions. It can be anodic controlled if the dissolution of iron is the limiting factor, or cathodic controlled when a limiting flux of oxygen exists. The rates of corrosion reactions are equivalent to an electrical current which depends on the electrical potentials of the anodic and cathodic sites. The value of either the anodic or cathodic current, whichever is the limiting, is referred to as corrosion current, I_{corr}, which determines the rate of steel consumption.

2.2 Rate of corrosion

The corrosion rate is the single determining parameter of the progress of corrosion-induced damage which gives a quantitative description of corrosion propagation (Andrade and Alonso, 1996). This rate can be described in terms of a current density that is equivalent to the loss of metal per unit of surface area per unit of time. For an accurate assessment of a damaged reinforced concrete structure, corrosion current density is one of the most important input parameters. Therefore, accurate prediction of the corrosion rate is a necessity if the damage prediction models are to be reliably used (Otieno et al., 2011). The corrosion rate can be obtained by measuring the weight loss of corroded reinforcement. ASTM G1-90 covers the procedures suggested for preparing test specimens, removing corrosion products, and evaluating the corrosion damage that has occurred. However, extraction of corroded reinforcing bars from a reinforced concrete structure might not be a feasible option (Lu et al., 2008). Non-destructive methods such as linear polarization resistance (LPR) estimate the rate of the corrosion in terms of corrosion current density, i_{corr}. A review of the available corrosion current density models is presented in subsequent sections.

2.2.1 Alonso et al. (1988)

Alonso et al. (1988) expressed i_{corr} as a function of concrete resistivity. Their formulation was derived based on a regression analysis of tests done on 20×55×80 mm mortars, built with various binders (Portland cement (PC), sulphate resistant PC, slag cement, pozzolanic cement, flay ash (FA) cement and 70/30 PC/FA). After 28 days of moisture curing, the mortar specimens were placed in a CO_2 filled chamber with 50-70% relative humidity. Corrosion of the steel bars embedded in the mortars was determined by weighing the specimens during the process. After carbonation took place, i_{corr} was measured while the specimens were subjected to partial immersion and consecutive humidity periods of 100% and 50% relative humidity. Corrosion current densities of 2.0 and 0.2 µA/cm^2 were measured at the beginning and end of the carbonation process. i_{corr} increased to quite high values of 3 to 10 µA/cm^2 while the mortars were partially immersed. On the contrary, i_{corr} was very low at 50% relative humidity showing an increase in concrete electrical resistivity. Based on the experimental results, the corrosion current density was defined as follows:

$$i_{corr} = \frac{k_{corr}}{\rho_{ef}} \tag{2.1}$$

where:

- k_{corr} = 3×10^4 µA/cm^2.kΩ-cm
- ρ_{ef} = resistivity of concrete

Electrical resistivity provides insight into the pore connectivity of concrete which can be a good indicator of durability (Andrade C., 2009). However, a wide range of values of electrical resistivity for the same service conditions have been reported by employing different measurement techniques. Therefore, formulating corrosion current density solely as a function of concrete resistivity might not be adequate. In addition, immersion of concrete in water can also decrease the rate of corrosion by limiting the supply of oxygen required for the cathodic reaction which is in conflict with the formulation of Alonso et al. (1988). Thus, the model is only valid for instantaneous corrosion current density measurements.

2.2.2 Yalcyn and Ergun (1996)

Yalcyn and Ergan (1996) investigated the effects of chloride and calcium acetate ions on corrosion current density by performing accelerated corrosion tests on cylindrical specimens of 150 mm diameter and 150 mm height. The specimens were made in three groups: Group A with no salt added, Group B having 6 kg/m^3 of NaCl, and Group C having 60 kg/m^3 of calcium acetate added to the concrete mixture. The corrosion current density was measured over a period of 90 days by employing linear polarization resistance technique as shown in Figure 2.2. In this technique, current density is measured by the application of an externally-imposed potential shift to the corroding electrode. The potential shift produces a measurable current flow which can be related to corrosion current density by the Stern-Geary equation:

$$i_{corr} = \frac{\beta_{\alpha}\beta_{c}}{2.3R_{p}(\beta_{\alpha} + \beta_{c})} \tag{2.2}$$

where R_p is the polarization resistance and β_α and β_c are Tafel constants which can be quantified empirically. Note that the formulation of Alonso et al. (1988) is basically the Stern-Geary equation.

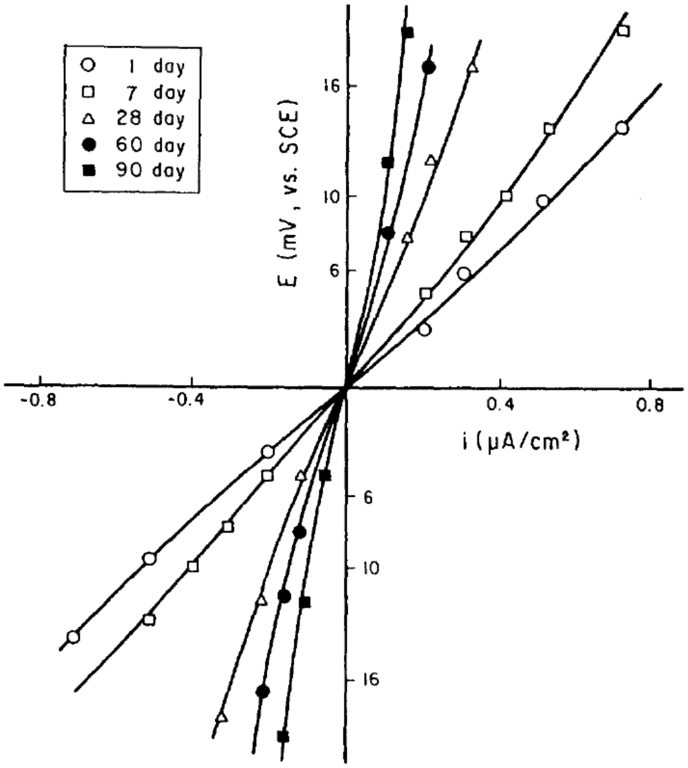

Figure 2.2: Linear polarization curves of Yalcyn and Ergun (1996) specimens. Taken from Yalcyn and Ergun (1996)

The moisture content, oxygen permeability of concrete, and presence of chloride ions in concrete were identified as the most important factors for the corrosion rate of reinforcing steel. Chloride ions contribute to corrosion by increasing the conductivity of the concrete pore solution, which acts as the electrolyte, and by forming a soluble complex of iron chlorides which breaks the protective oxide layer over the reinforcement. Based on the test results an exponential quantitative relation between i_{corr} and exposure time as shown in Figure 2.3 was proposed:

$$i_{corr} = i_0 e^{-Ct} \tag{2.3}$$

where:

- i_0 = initial corrosion rate
- C = concrete corrosion constant taken as $1.1\text{x}10^{-3}$ day^{-1}
- t = corrosion time in days

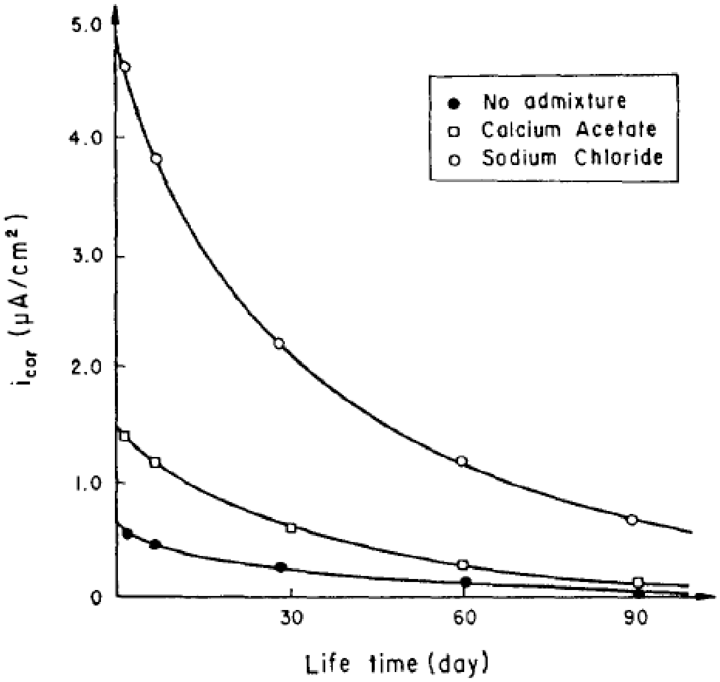

Figure 2.3: Corrosion current density versus exposure time of specimens cast from concrete with and without admixtures. Taken from Yalcyn and Ergun (1996)

2.2.3 Liu and Weyers (1998)

The Liu and Weyers (1998) experiments consisted of 44 bridge deck slabs with dimensions of 1180 × 1180 × 216 mm. The design variables of the tests were the amount of added chloride, cover thickness, and bar diameter. Three different bar diameters of 12, 16, and 19 mm were used in the construction of the slabs. The concrete ohmic resistance and ambient temperature were monitored over a period of five years. The temperature at the reinforcement surface was measured by Type T thermocouples placed at the steel-concrete interface. The effect of the linear polarization measurement technique on the measured corrosion rate was clearly demonstrated by employing two types of measuring devices, namely the 3LP and Gecor devices. The difference between the two measurements was approximately an order of magnitude. The exact corrosion rate was calculated by measuring the weight loss of the reinforcement in accordance with Method C3.5 of ASTM G1-90. As shown in Table 2.1, the rate of corrosion was overestimated by the 3LP device while underestimated by the Gecor device. From statistical analysis of the results, the following conclusions were drawn:

- corrosion rate increases with an increase in chloride content
- corrosion rate has a direct relationship with temperature

- cover thickness does not have a noticeable effect on corrosion rate.

From the regression analysis of 2927 measurements, the following relationship shown in Figure 2.4 was suggested:

$$\ln 1.08 i_{corr} = 7.89 + 0.7771 \ln(1.69 Cl) - \frac{3006}{T} - 0.000116 R_c + 2.24 t^{-0.215} \quad (2.4)$$

where:

- i_{corr} = corrosion current density (µA/cm^2)
- Cl = chloride content (kg/m^3) measured by the acid soluble test method (ASTM C115)
- T = temperature at the steel-concrete interface (K^o)
- R_c = resistance of cover concrete (Ω)
- t = corrosion time (years)

Table 2.1: Mean corrosion rates of Liu and Weyers (1998) measured using three methods

Test series	Exposure period (year)	Mean corrosion rate (µA/ft^2)		
		Weight loss method	3LP	Gecor
OA2859.6	1.84	2.35	8.49	0.54
OB3859.6	3.67	1.80	4.99	0.42
OE185512.0	0.87	3.77	8.63	0.67
OF18512.0	0.87	3.77	8.85	0.59
Block9.6	2.38	1.81	6.49	0.39

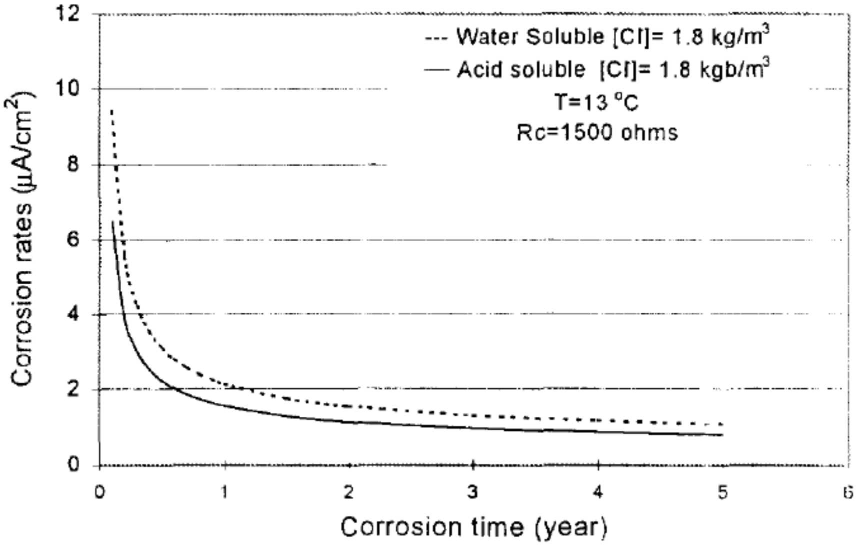

Figure 2.4: Corrosion current density versus time. Taken from Liu and Weyers (1998)

2.2.4 Vu and Stewart (2000)

Based on the experimental results of Liu and Weyers (1998), Vu and Stewart (2000) proposed the following corrosion rate model:

$$i_{corr} = i_{corr}(l) \cdot 0.85t^{-0.29}(\frac{\mu A}{cm^2}) \tag{2.5}$$

where:

- t = time since corrosion initiation
- $i_{corr}(l)$ = corrosion current density at the start of corrosion

For an ambient relative humidity of 75% and temperature of 20ºC, the following formulation for initial corrosion rate was suggested:

$$i_{corr}(l) = \frac{37.8(1-\frac{w}{c})^{-1.64}}{C} (\frac{\mu A}{cm^2}) \tag{2.6}$$

where:

- C = concrete cover (cm)
- w/c = water-cement ratio

Although oxygen and moisture are the main components of corrosion, the availability of oxygen was assumed to be the only limiting parameter of the corrosion reaction as the relative humidity in many locations including Australia, US, Europe, and Asia is over 70%. The effect of concrete quality, reflected by water-cement ratio, on oxygen diffusion rate has been considered in the formulation of the initial corrosion rate as illustrated in Figure 2.5.

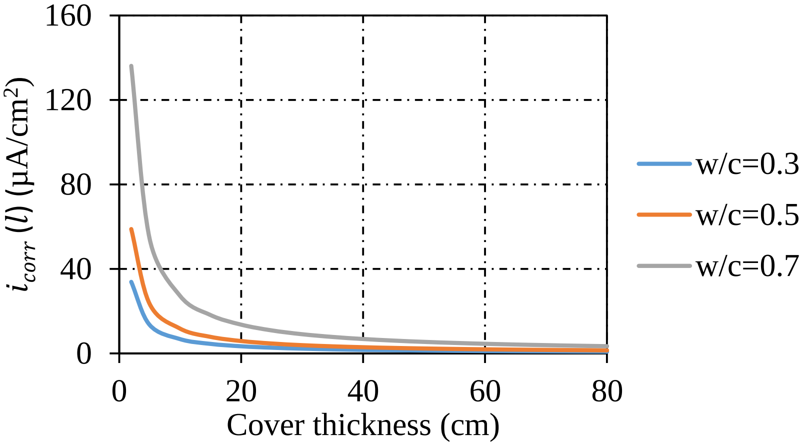

Figure 2.5: Influence of cover thickness and w/c ratio on corrosion rate. Reproduced from Vu and Stewart (2000)

2.2.5 Lu et al. (2008)

Lu et al. (2008) improved the Vu and Stewart (2000) formulation by including the effects of ambient relative humidity and temperature as follows:

$$i_{corr}(l) = \frac{T_k H_r (w/c)}{d_c} (\frac{\mu A}{cm^2}) \tag{2.7}$$

where:

- $i_{corr}(l)$ = initial corrosion current density at the start of corrosion propagation
- T_k = average temperature (K^o)
- H_r = average relative humidity

An inconsistency with the experimental evidence of the Vu and Stewart (2000) formulation was noted by Lu et al. (2008): for t<0.5, the instantaneous corrosion current density, i_{corr}, is greater than the initial corrosion current density. Theoretically, the corrosion current density is expected to reduce with time as the accumulation of rust over reinforcement decreases the rate of corrosion. Hence, Lu et al. (2008) suggested an improved time-variant model of the corrosion current density as follows:

$$i_{corr}(t) = \frac{i_{corr}(l)}{\sqrt[3]{1+t}} (\frac{\mu A}{cm^2}) \tag{2.8}$$

2.3 Bond strength

The bond between reinforcement and concrete makes the composite action between the two materials possible. The mechanisms which transfer the bond stresses are known to be chemical adhesion, mechanical interlocking, and friction. However, the degree to which the transfer mechanisms are degraded due to corrosion is a matter of further study. Corrosion affects the bond strength in several ways. An enhanced bond strength for lightly corroded bars has been reported in literature. Before cracking, the frictional component of bond increases as a result of increased radial stresses between the reinforcement and concrete. A firmly adherent layer of rust may also contribute to the enhancement of the bond strength at early stages of corrosion (Al-Sulaimani et al., 1990). Reduced height of the ribs on a deformed bar, disengagement of the ribs and concrete, flaky corrosion products, and longitudinal cracking of the cover are the possible causes of the reduction in the bond strength at more advanced stages of corrosion. Experimental studies confirming the mentioned influences of corrosion on the bond strength are presented in the following sections.

2.3.1 Almusallam et al. (1996)

Almussalam et al. (1996) reviewed several test methods for bond strength of deformed reinforcing bars such as the concentric pull-out test (ASTM C234), the tension pull-out test, the bond beam test, and the cantilever bond test. The commonly used concentric pull-out test was perceived to be unrealistic as the concrete around the reinforcement is in compression, which increases the bond strength, whereas in a real beam the concrete around the reinforcement is in tension and cannot provide any confinement. Although the beam bond test is representative of the bond stress condition of flexural members, it is costly and the confinement provided by support reactions might increase the bond strength over the supports. For the reasons above, the cantilever bond test was regarded as the most appropriate testing method and was used to examine the effects of corrosion on the bond strength of deformed bars. The dimensions of the specimens were 152 × 254 × 279 mm. A tension bar with 12 mm diameter and a bonded length of 102 mm was selected. A sketch of the test specimen is shown in Figure 2.6. In order to avoid shear and compression failures of the specimens, sufficient compression and transverse reinforcement were provided. The stirrups were placed in such a way that they did not provide any confinement for the tension reinforcement.

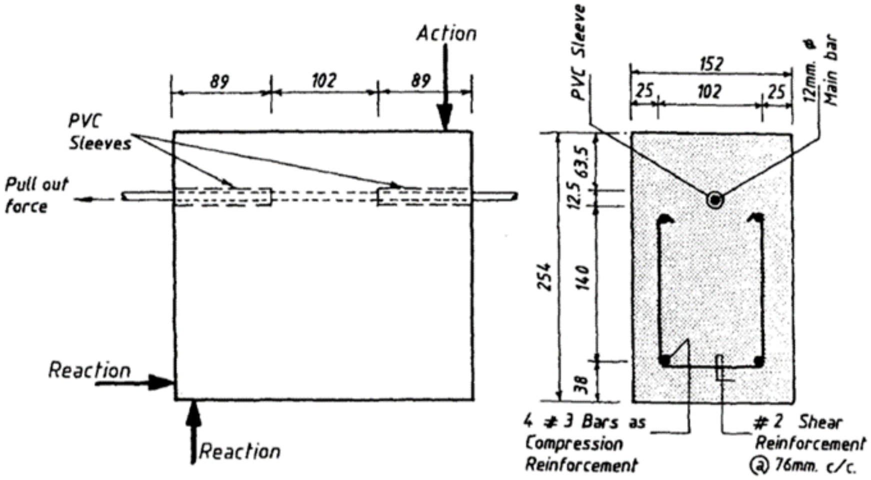

Figure 2.6: Sketch of Almusallam et al. (1990) test specimen. Taken from Almusallam et al. (1996)

The tension reinforcing bar was corroded by means of a direct current of 0.4 A. The corrosion was recorded by the gravimetric method. The stirrups and compression reinforcement were protected against corrosion by an epoxy coating. The appearance of the first crack over the surface of the member was carefully recorded to mark the transition from the pre-cracking stage to the cracked stage. The result of the tests, depicted in Figure 2.7, showed a slight increase in the bond strength for up to 4% corrosion, mainly due to the confining action of the corrosion products accumulated around the reinforcement before cracking of the concrete. On the other hand, the slip at the ultimate load was considerably reduced. Up to this stage, the bond failure was governed by crushing of concrete keys adjacent to the reinforcement ribs. After cracking, the bond strength was substantially reduced due to the loss of confinement and the bond failure was governed by splitting failure of the concrete. At about 12% corrosion, complete loss of confinement was observed and the failure mode altered from splitting to continuous slip of the reinforcement.

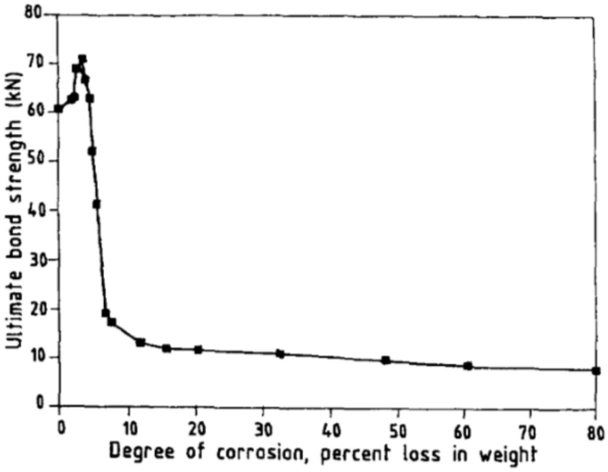

Figure 2.7: The ultimate bond strength versus corrosion degree. Taken from Almusallam et al. (1996)

2.3.2 Al-Sulaimani et al. (1990)

Al-Sulaimani et al. (1990) examined the effects of reinforcement corrosion on bond behaviour by performing four series of tests. Series 1 consisted of pull-out tests on 150 mm cubic specimens with 10, 14, and 20 mm embedded bars. Reinforcing bars were embedded centrally to allow for a ratio of cover to bar diameter of 7.50, 5.36, and 3.75. The embedment length to diameter ratio for each test was 4.0. The concrete used in casting of the specimens had a compressive strength of 30 MPa and a water-cement ratio of 0.55. Series 2 specimens had the same properties as Series 1 except they had 0.2% polypropolene fibers by volume added to the concrete mix. In Series 3, flexural tests on simply supported beams reinforced with corroded tension bars were conducted. The specimens had a 150 × 150 mm cross section and were 1000 mm long. The concrete mixture had a water-cement ratio of 0.45 and a compressive strength of 40 MPa. The beams were reinforced with a single 12 mm diameter bar at the top and two 10 mm bars at the bottom. Double-legged 6 mm closed stirrups with 50 mm spacing were used as transverse reinforcement. To promote bond failure, the tension reinforcement had an embedment length of 144 mm. In accordance with the ACI building code, the development length for Series 4 tests was increased to 300 mm. The geometry and properties of Series 4 beams were identical to that of Series 3.

The reinforcing bars used in every specimen had an average yield strength of 450 MPa and were subjected to different levels of corrosion by a constant current density of 2 mA/cm^2. The experimental setup for the accelerated corrosion tests is shown in Figure 2.8. The specimens were soaked in water to facilitate an even passage of current over the whole length of the reinforcing bars. The direction of the current was set in such a way that the stainless steel plate, placed in water, served as the cathode whereas the reinforcement was the anode.

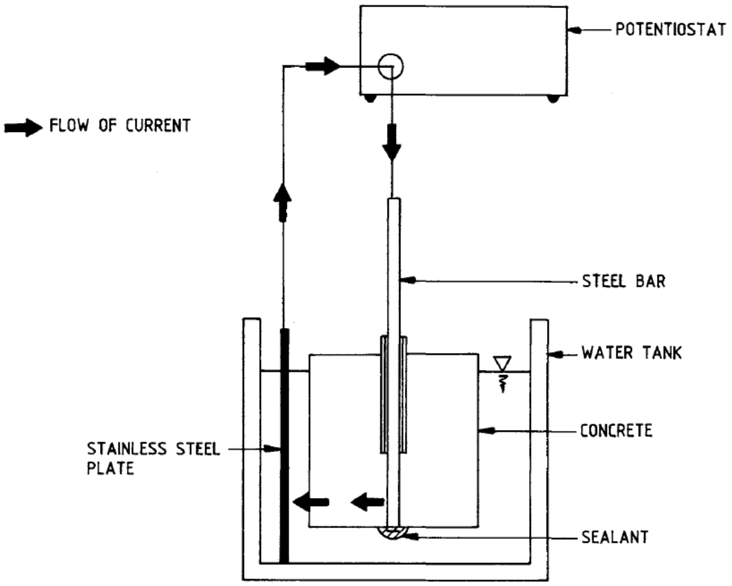

Figure 2.8: Schematic drawing of accelerated corrosion test setup. Taken from Al-Sulaimani et al. (1990)

Pull-out tests were conducted on Series 1 and Series 2 specimens in a universal testing machine with 250 kN maximum capacity. The bond-slip curves for 10 mm bars with different levels of corrosion are shown in Figure 2.9. Prior to the cracking of the cover concrete, an increase in the bond strength was observed which was attributed to increased surface roughness of the bars due to corrosion. With increasing levels of corrosion, the bond strength was mainly affected by the lubricating effect of the corrosion products that disturbs the interlock action between the ribs of the bar and the concrete. The bond strength became negligible at 8.5, 7.5, and 6.5 percent corrosion for 10, 14, and 20 mm bars, respectively. The corrosion degree at which the bond strength became negligible was mainly a function of the cover to bar diameter ratio which had the smallest value for the largest bar diameter. At this level, the concrete cover had no confining action and the residual bond strength was mainly due to friction. There was 8% improvement in the bond strength of fiber reinforced concrete in pre-cracking and cracking stages. The beneficial effect of fibres was more significant in the post-cracking stage at which the increase in the bond strength was in the order of 100 percent. Al-Sulaimani et al. (1990) postulated that the improved bond behaviour of fibre reinforced concrete was due to the reduced level of damage at the concrete-steel interface and increased confining and holding capacity of the cover concrete.

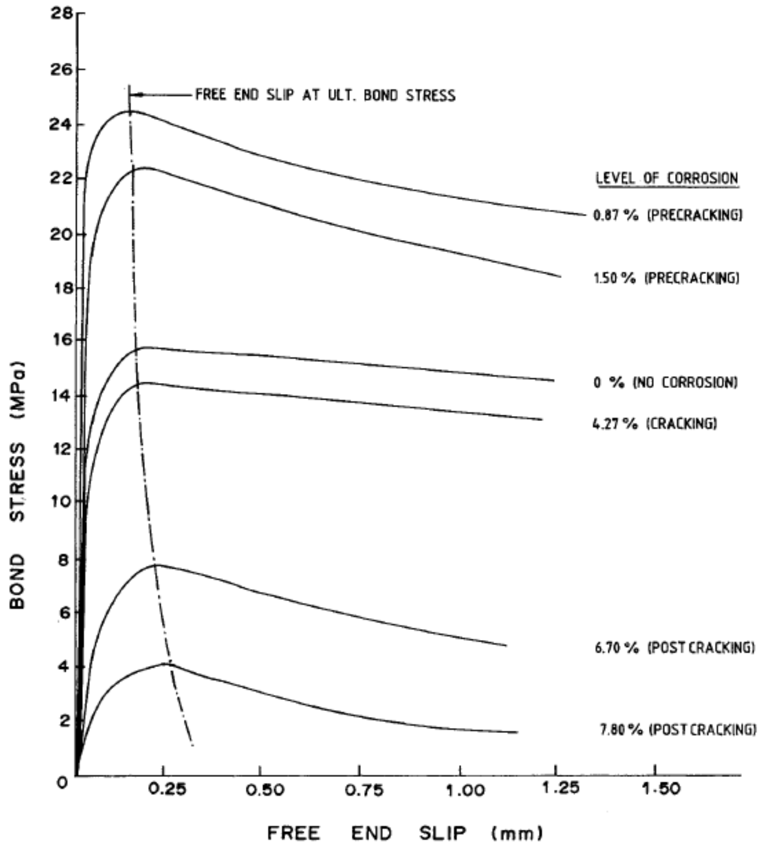

Figure 2.9: Bond stress versus free end slip of a corroded 10 mm diameter bar. Taken from Al-sulaimani et al. (1990)

The beam specimens were examined with a four-point bending test with a shear span of 300 mm. The deflections of the beams and the free-end slips of the reinforcing bars were measured by means of five LVDTs which were connected to the bottom fibre of the beams and the two ends of reinforcement as depicted in Figure 2.10. The failure of the Series 4 beams occurred at a small free-end slip and ultimate loads similar to the design capacity. However, in the Series 3 specimens the free-end slip increased at a fast rate, signaling bond breakdown. This rate was higher for post-cracking stages due to the loss of bar confinement. The load-deflection curves of the Series 3 and Series 4 beams are plotted in Figure 2.11. The authors defined the force at which bond break down took place in the Series 3 beams as P_e.

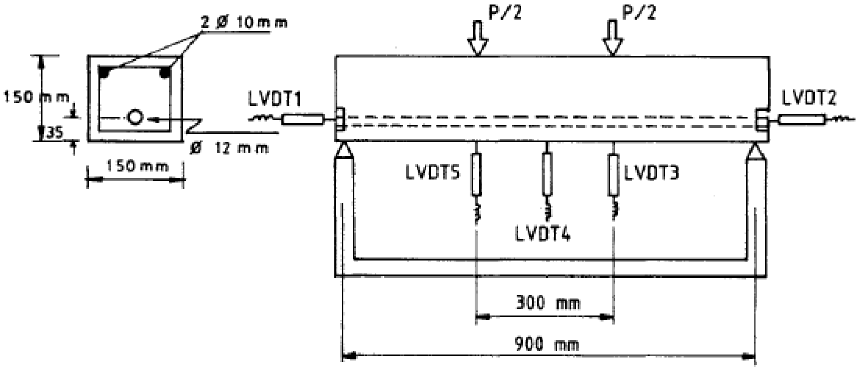

Figure 2.10: Test setup of Series 3 and Series 4 beams. Taken from Al-Sulaimani et al. (1990)

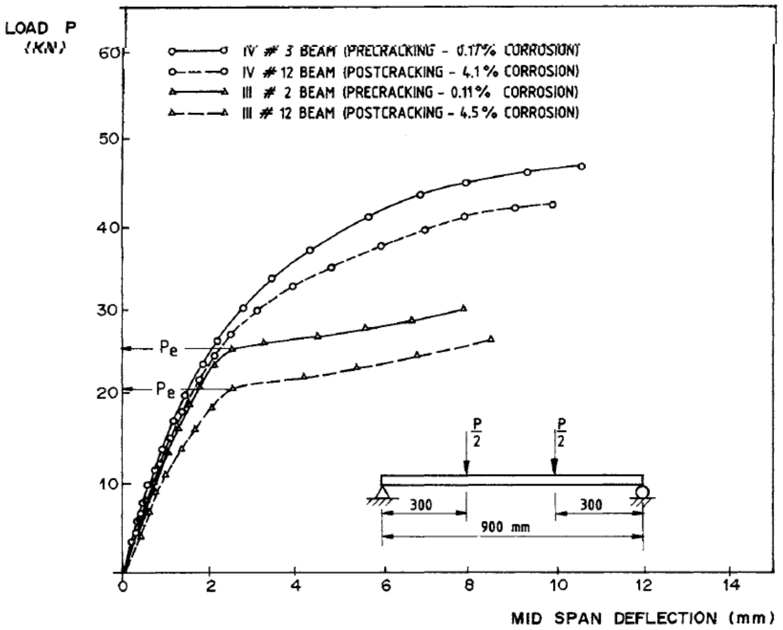

Figure 2.11: Typical load versus mid-span deflection of Series 3 and Series 4 beam. Taken from Al-Sulaimani et al. (1990)

2.3.3 Abosrra et al. (2011)

Abosrra et al. (2011) studied the influence of concrete compressive strength on the bond strength of corroded bars. Pullout tests were performed on corroded 12 mm diameter bars embedded in 150 mm concrete cubes. The specimens were divided into three groups having a concrete compressive strength of 20, 30, and 46 MPa. The embedment length of the bars was five times the diameter. The specimens were kept in moulds for 3 days and then cured for 25 days before being immersed in a 3% NaCl solution by weight of water. The corrosion process was accelerated by an externally applied current of 0.4 A. The corrosion test setup was almost identical to that of Al-Sulaimani et al. (1990) shown in Figure 2.8. The average rate of corrosion was measured after 1, 7, and 15 days of accelerated corrosion. The specimens with the highest concrete compressive strength had the lowest rate of corrosion, due to lower water-cement ratio and permeability which provided a barrier against chloride penetration. After one day of corrosion, small cracks could be observed on the concrete-steel contact edges of the specimens with 20 MPa concrete whereas the specimen with 46 MPa concrete did not show any signs of corrosion. After 15 days, wide cracks filled with rust were observed on the surface of the cubes as depicted in Figure 2.12 and Figure 2.13. However, the width of the cracks and the amount of rust stain on the surface were much less for specimens with 46 MPa concrete.

Figure 2.12: Effect of accelerated corrosion on cube specimens with concrete of 20 MPa compressive strength after 1 day (left) and 15 days (right). Taken from Abosrra et al. (2011)

Figure 2.13: Effect of accelerated corrosion on cube specimens with concrete of 46 MPa compressive strength after 1 day (left) and 15 days (right). Taken from Abosrra et al. (2011)

The results of the pullout tests, shown in Figure 2.14, manifested a slight increase in the bond strength after one day of corrosion and then a sudden drop for 15 days of accelerated corrosion that is in agreement with the observations of other researchers. Based on macroscopic observation of the corroded bars shown in Figure 2.15, a significant amount of red and brown rust was detected on the bars embedded in the 30 and 46 MPa concrete specimens. Severe and deep pitting corrosion was observed on the surface of reinforcement after 15 days of corrosion. Such localized corrosion covered a wider length of the bar when corrosion exposure extended to over 15 days. Deep grooves were observed on the steel surface of the 46 MPa concrete specimens after 15 days of corrosion. The authors attributed this somewhat new observation to the ability of high strength concrete to keep the corrosive environment in a narrow zone.

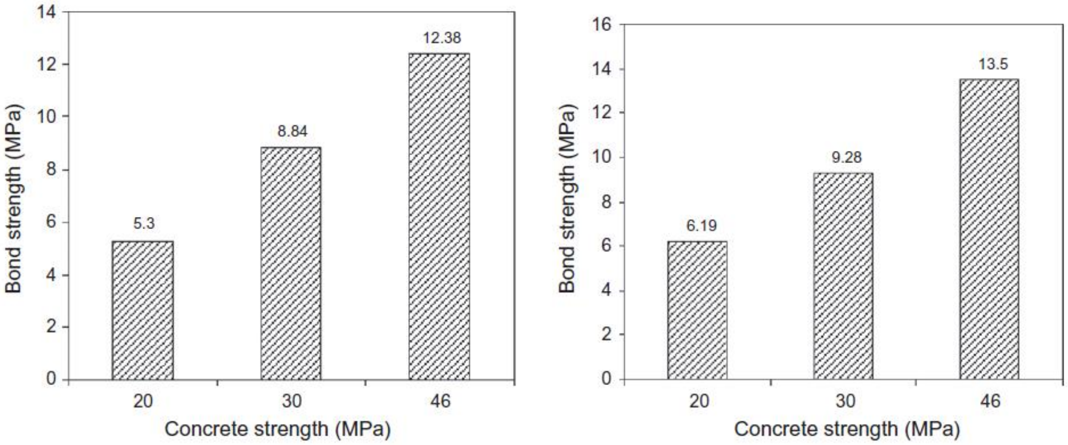

(a) Un-corroded, control specimens (b) 1 day accelerated corrosion

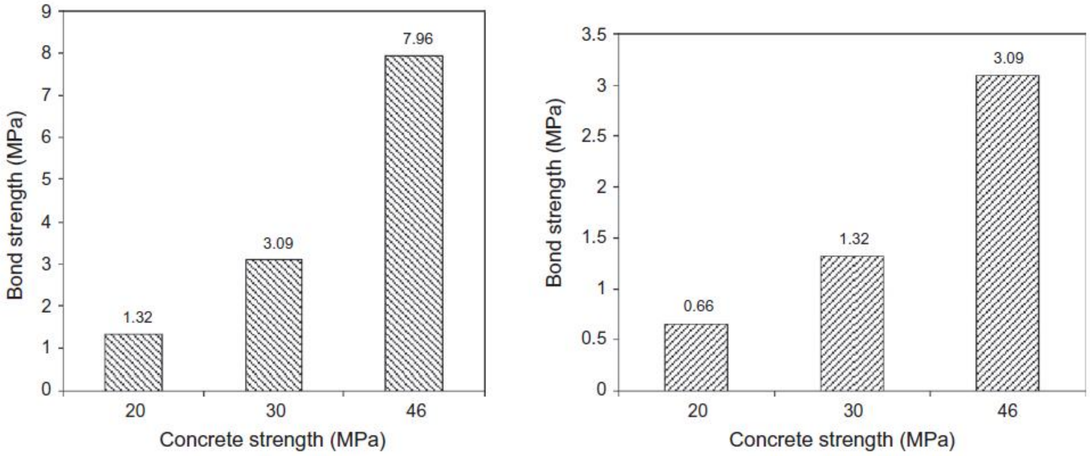

(c) 7 days accelerated corrosion (d) 15 days accelerated corrosion

Figure 2.14: Bond strength versus concrete compressive strength. Taken from Abosrra et al. (2011)

Figure 2.15: Macroscopic examination of the corroded steel bars embedded in concrete. Taken from Abosrra et al. (2011)

2.4 Cover cracking

When the corrosion reaction occurs, depending on environmental conditions such as relative humidity and availability of oxygen, a combination of corrosion products forms around the reinforcement. These products occupy a much greater volume than the original iron consumed in the reaction. This increase in the volume applies radial pressure to the steel-concrete interface and develops hoop tensile stresses in the surrounding concrete, which eventually results in cracking of the cover concrete. Generated hoop tensile stresses in the cover are highly dependent on the ratio of the volume of unit mass of rust to that of iron, denoted by α_1. Table 2.2 shows this ratio for different compositions of rust.

Table 2.2: α_1 for different types of corrosion products. Taken from Bhargava et al. (2005)

Corrosion product	α_1
FeO	1.80
Fe_3O_4	2.00
Fe_2O_3	2.20
$Fe(OH)_2$	3.75
$Fe(OH)_3$	4.20
$Fe(OH)_3 \cdot 3H_2O$	6.40

The appearance of visible cracks on the surface of a reinforced concrete member is a serviceability limit state at which appropriate remedial actions should be taken. Since reinforcement corrosion is the predominant deterioration process of reinforced concrete structures, a wide range of models have been developed to predict the time it takes for the corrosion cracks to appear on the surface of a member (Jamali et al., 2013). These cracks also contribute to the acceleration of other deteriorating processes such as sulfate attack or alkali-silica reactions (ASR). In the case of uniform corrosion, reactions occur uniformly along the surface of the reinforcement which favors the deposition of products such as $Fe(OH)_2$, $Fe(OH)_3$, Fe_3O_4, and Fe_2O_3. On the other hand, due to the conditions associated with localised (pitting) corrosion, such as the limited supply of oxygen inside the pit, iron ions have to travel a further distance from the pit mouth to react with the hydroxide ions and a less expansive form of rust is produced. This has been reflected in Figure 2.16 and Figure 2.17. The experimental studies reviewed in the following sections cover the important aspects of corrosion-induced cracking of the cover concrete.

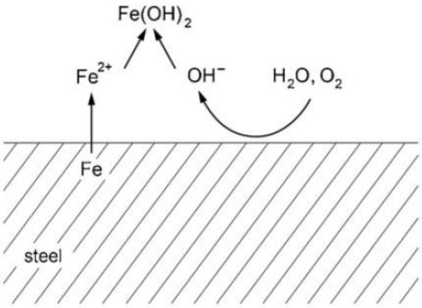

Figure 2.16: Electrochemical reactions of uniform corrosion. Taken from Angst et al. (2012)

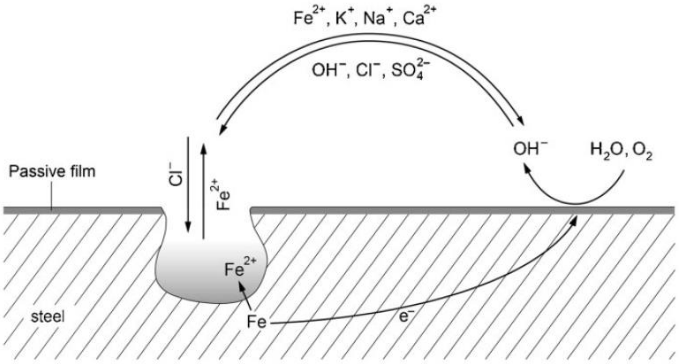

Figure 2.17: Electrochemical reactions of pitting corrosion. Taken from Angst et al. (2012)

2.4.1 Andrade et al. (1993)

Andrade et al. (1993) studied the time elapsed between steel depassivation and concrete cracking. Four concrete blocks with dimensions of 150 × 360 × 150 mm were fabricated. Specimen I was reinforced with one 16 mm diameter rebar located at the top right corner which had 20 mm and 30 mm vertical and horizontal clear covers, respectively. Specimens II and IV had a reinforcing bar at the top center area with a 20 mm vertical cover. The clear cover was increased to 30 mm for Specimen III. The concrete mix used in casting the blocks had a water-cement ratio of 0.5 with 3% $CaCl_2$ by weight of cement added to the mix. The average splitting tensile strength of concrete was 3.55 MPa. The corrosion process was accelerated by the application of a current density of 100 µA/cm^2 to Specimens I, II, and III and 100 µA/cm^2 to Specimen IV.

The deformations recorded on the concrete surface of Specimen I are shown in Figure 2.18. Tensile strain was measured in eight locations by means of strain gauges. Maximum elongation was observed in strain gauge No.6. Unexpectedly, strain gauge No. 4, which was located on the same surface as the strain gauge No.6, experienced a much smaller strain. Due to the addition of $CaCl_2$, the rebar had a 1.9 µm radius loss before the application of the current. The appearance of the first visible crack was observed through a magnifying glass. At this point, the width of the crack was less than 0.05 mm. The distribution of deformations over the top surface of other specimens was more homogenous. Regardless of the cover thickness and the applied current, a radius loss of about 20 µm was sufficient to crack the surface of the cover concrete. However, the radius loss required for a crack width of 0.3-0.4 mm was significantly lower for Specimen IV. The crack width reached this value with only 50 µm radius loss in Specimen IV, where the current density was 10 µA/cm^2. Other specimens had to undergo a 100 µm radius loss to have the same crack width. This shows a dependency between the type of the produced rust and the magnitude of the applied current.

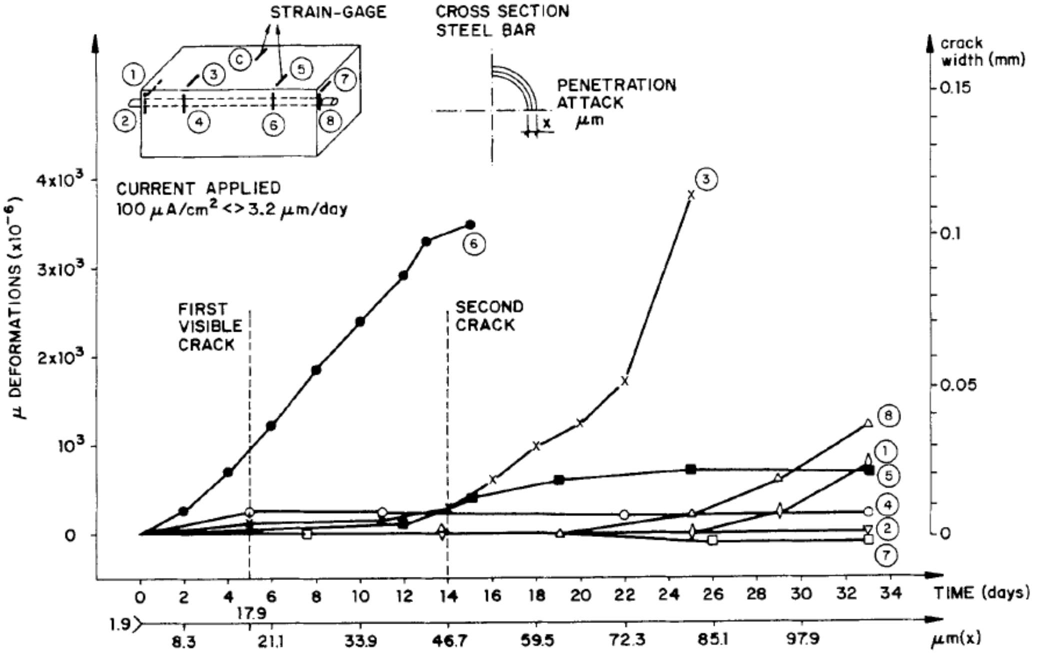

Figure 2.18: Deformations recorded in the surface Andrade et al. (1993) Specimen I. Taken from Andrade et al. (1993)

2.4.2 Vu et al. (2005)

Vu et al. (2005) constructed eight reinforced concrete 700 × 1000 mm rectangular slabs with a thickness of 250 mm. The slabs were reinforced with five bars, four of which were exposed to corrosion over their full 1000 mm length and one partially exposed to corrosion over the middle 100 mm portion of its length. The design variables of the tests were concrete covers of 20 and 50 mm and water-cement ratios of 0.45, 0.5, and 0.58. Three percent $CaCl_2$ by weight of cement was added to the concrete mixture to induce corrosion along the exposed length of the bars. An accelerated corrosion rate of 100 $\mu A/cm^2$ was used. The tests were further accelerated by immersion of the specimens in a 5% NaCl solution. The time of appearance and propagation of cracks was recorded using visual observations, a magnifying glass, and potentiometer displacement transducers (POTs) glued on both sides of a crack. The tests were terminated when the average crack width reached 1.0 to 1.5 mm.

The first visible cracks, referred to as hairline cracks with a width of 0.05 mm, were observed at random locations on the concrete surface above and parallel to the reinforcement. Thereafter, the width and length of the cracks increased in a non-homogenous manner until the cracks joined together to create 0.25 to 0.4 mm wide longitudinal cracks. Cracks propagated at a much smaller rate on the concrete surface over the bar with 100 mm exposed length. The rate of corrosion calculated from the gravimetric weight loss method was generally higher than the applied 100 $\mu A/cm^2$. The authors attributed this to the spallation of fragments of the metal from the reinforcement without dissolving electrochemically. Signs of pitting corrosion with depths of pits varying from 1.4 to 5 mm were also detected. Although the localized nature of pitting corrosion results in the production of a less expansive form of rust, Vu et al. (2005) postulated that localized corrosion can happen over a noticeable length of a bar, stressing the cover concrete in a uniform manner, and crack models based on general corrosion can be used for modelling of structures subjected to chloride induced corrosion. Figure 2.19 depicts the measured crack width versus exposure time. The crack initiation time, defined as the period of time between corrosion initiation and appearance of the hairline crack, was longer for the specimens with 50 mm cover. No meaningful correlation between water-cement ratio and crack initiation time was found.

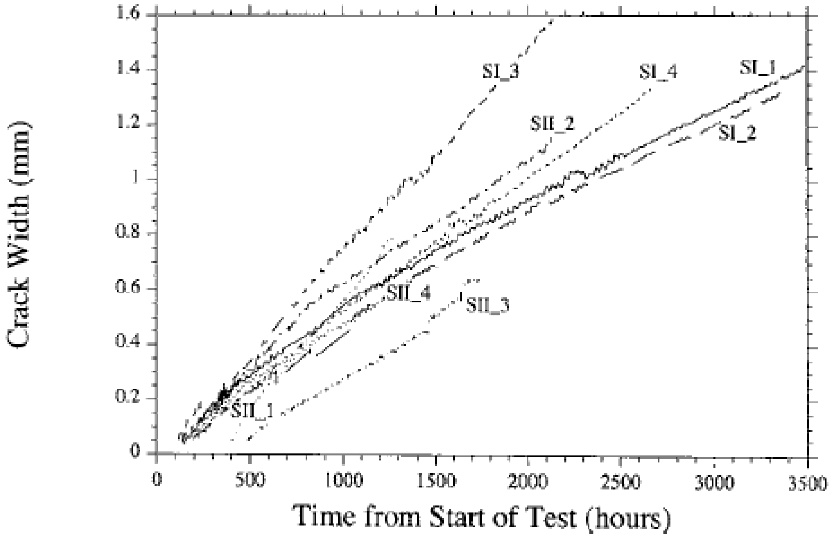

Figure 2.19: Crack width versus corrosion time. Taken from Vu et al. (2005)

2.4.3 Zhang et al. (2010)

As part of a long-term experimental program, Zhang et al. (2010) studied the corrosion pattern of two beams exposed to salt fog (35 g/L NaCl) for 14 and 23 years. The full-size beams had dimensions of 3000 × 280 × 150 mm. The average concrete compressive strength measured from cylindrical specimens was 45 MPa. Instead of using an electrical current or adding $CaCl_2$ to the concrete mix, the authors believed that corrosion induced by salt fog represents the on-site situation more realistically. The beams were loaded by a point load at the mid-span during the exposure period. The cracking maps of the corroded beams are presented in Figure 2.21 and Figure 2.20. After a period of 14 years, randomly distributed cracks were observed on the compression surface which were less than 0.5 mm wide. Due to easier diffusion of the salt fog through the flexural cracks caused by loading of the beams, corrosion cracks in the tension zone were significantly wider. Longer and wider corrosion cracks, with a maximum width of 3.3 mm, were observed on the beam exposed to corrosion for 23 years. Cover spalling was also observed in the hatched parts of the beam depicted in Figure 2.21. Careful examination of the corrosion pattern along the length of the reinforcing bars revealed signs of isolated pitting attacks in addition to general corrosion. Various types of corrosion products, depending on the location along the beam, were detected on the same reinforcing bar. The locations of pitting attacks corresponded with corrosion cracks less than 0.5 mm wide. In general, the corrosion pattern evolved from a localized form towards a more uniformly distributed pattern observed in general corrosion and the flexural cracks did not have significant effect on the corrosion rate in the long term.

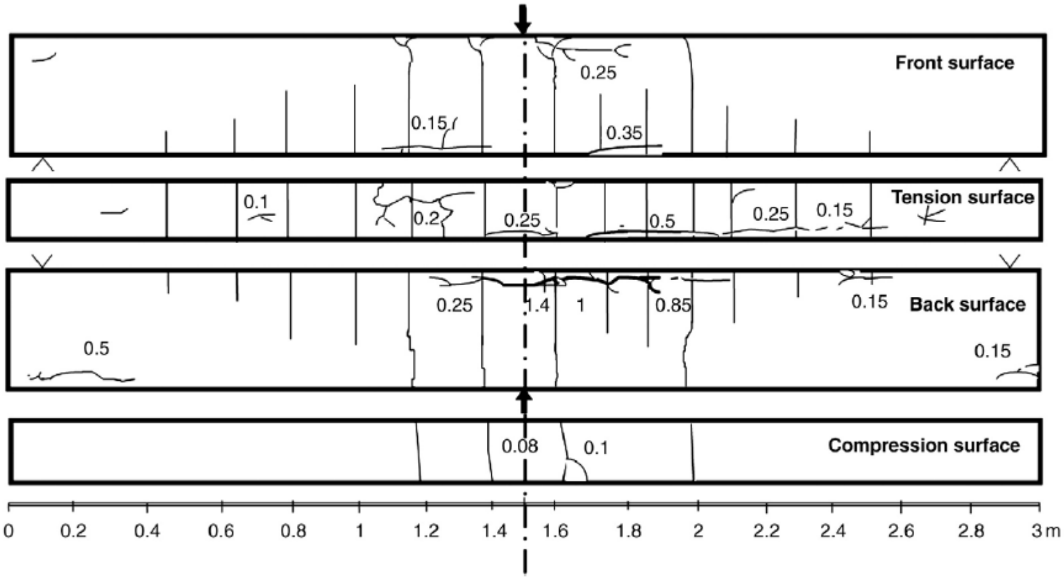

Figure 2.20: Cracking map of the beam exposed to salt fog for 14 years. Taken from Zhang et al. (2010)

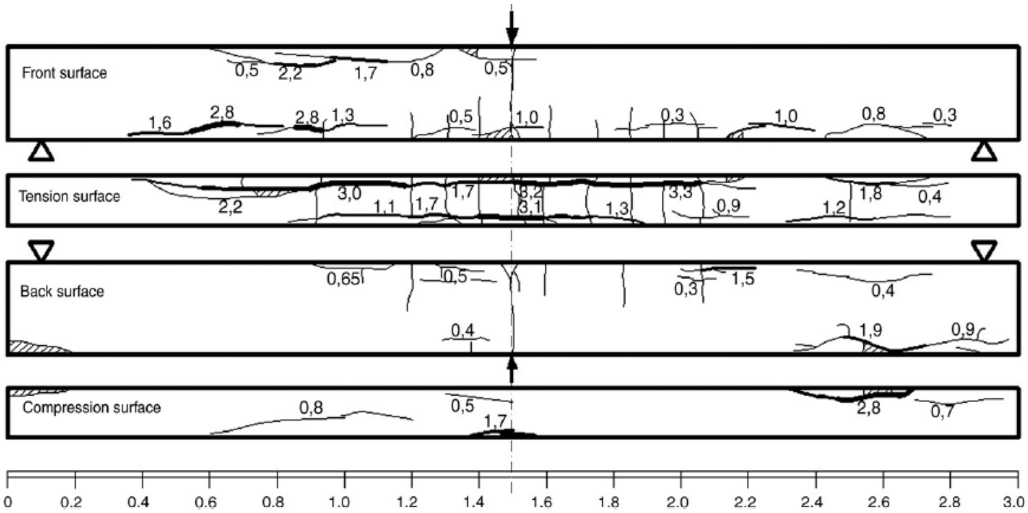

Figure 2.21: Cracking map of the beam exposed to salt fog for 23 years. Taken from Zhang et al. (2010)

2.5 Pitting corrosion

Pitting corrosion is more likely to occur in structures exposed to an oceanic environment or de-icing salt. The localized nature of pitting corrosion along with a less expansive form of oxidation products can cause substantial cross section loss without any visible warning signs such as the appearance of longitudinal cracks with significant width on the surface of the member (Cairns et al., 2005). In order for the chloride ions to break down the protective iron oxide layer around the reinforcement, chloride ion concentration in the pore solution must exceed a threshold. In general, when the chloride concentration in reinforced concrete members exceeds 0.4% (for chlorides cast into concrete) or 0.2% by weight of cement (for chlorides diffusing in), the reinforcement is prone to pitting corrosion (Apostolopoulos et al., 2013). ACI 318-95 “Building Code Requirements for Reinforced Concrete” stipulated the limits shown in Table 2.3 for protection against chloride corrosion. Experimental studies related to pitting corrosion are reviewed and the important aspects of them are briefly summarized in the following sections.

Table 2.3: Maximum chloride ion content for corrosion protection of reinforcement. Taken from ACI 318-95

Type of member	Maximum water soluble chloride ion (Cl^-) in concrete, percent by weight of cement
Prestressed concrete	0.06
Reinforced concrete exposed to chloride in service	0.15
Reinforced concrete that will be dry or protected from moisture in service	1.00
Other reinforced concrete construction	0.30

2.5.1 Tuutti (1982)

Tuutti (1982) conducted accelerated corrosion tests on plain bars with dimeters of 5 and 10 mm. To study the effects of concrete porosity and permeability, the concrete used in the casting of the specimens had a water-cement ratio of 0.50 and 0.81. The bars were fixed at a certain distance from the bottom of the moulds to allow for 10 and 30 mm concrete covers. Corrosion of the reinforcement was accelerated by means of an externally applied current as shown in Figure 2.22. Unlike the recent accelerated corrosion tests in which the applied current is controlled, the external voltage was kept constant at 0.9 V in these tests.

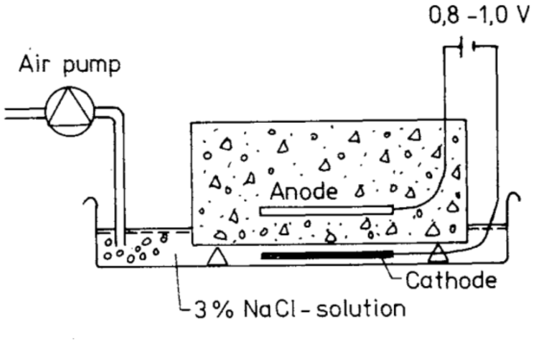

Figure 2.22: Sketch of Tuutti (1982) test specimen. Taken from Tuutti (1982)

The first sign of corrosion was observed after a period of one month when the 3% NaCl solution discoloured to a rust brown colour, indicating the presence of ferric hydroxide in the solution. After one more month, the same colour was observed at the concrete surface. After 1.5 years of exposure, corrosion cracks parallel to the reinforcement were observed on the specimen with the water-cement ratio of 0.81 and 10 mm concrete cover. After two years, the specimens were broken down, and the mean corrosion rate was evaluated by measuring the weight loss due to corrosion of the bars. The maximum pitting depths were also estimated utilizing a sliding caliper. The results are presented in Table 2.4. Most of the corrosion products were magnetite (Fe_3O_4) which has a volume twice that of iron and is black in colour. An average corrosion attack of 0.06 mm was sufficient to crack the concrete cover. The maximum pit depth was about 3 to 14 times the average attack. In conclusion, the specimens with high porosity, small bar diameter, and thick cover showed the highest capacity against corrosion cracking.

Table 2.4: Tuutti (1982) experimental results

Diameter (mm)	w/c	Cover (mm)	Corrosion depth (mm)		
			Mean	maximum	Maximum/Mean
5.0	0.50	10	0.52	3.5	6.73
9.5	0.50	30	0.37	3.0	8.11
5.0	0.81	10	0.34	1.0	2.94
5.0	0.81	30	0.43	3.0	6.98
5.0	0.81	30	0.07	1.0	14.29
9.5	0.81	10	0.35	3.0	8.57
10.5	0.81	10	0.21	1.0	4.76
10.5	0.81	30	0.39	1.5	3.85

2.5.2 Gonzalez et al. (1995)

In this study, the average corrosion penetration was compared to the maximum depth of corrosion through natural and accelerated corrosion tests. For the natural tests, two types of specimens with dimensions of 500 × 500 × 100 mm and 200 × 150 × 100 mm were built. The first type had 3% of $CaCl_2$ by weight of cement added to its concrete mixture and was subjected to repeated cycles of wetting and drying. The second type had no admixtures but it was submerged into natural sea water with 28 g/L of salt content.

After six years, the specimens were broken down and the corroded reinforcement was inspected. The average weight loss was measured by weighing a unit length of the reinforcement after removal of concrete and adhered corrosion products. Measurement of the pit depths was done in two ways: where the pits were large enough the depth was measured using a micrometer, while in the other cases an optical microscope was used.

Table 2.5: Experimental results of Gonzalez et al. (1995)

Diameter (mm)	Cover (cm)	I_{corr} ($\mu A/cm^2$)	Exposure time (days)	No. of tests	Corrosion attack (mm)		
					Avg.	Max.	Max./ Avg.
-	-	Natural[1]	6x365	1	0.26	1.20	4.4
-	-	Natural[1]	6x365	1	0.08	0.50	5.9
1N	-	Natural[2]	6x365	1	0.62	5.50	8.9
2N	-	Natural[2]	6x365	1	0.41	1.51	3.7
3N	-	Natural[2]	6x365	1	0.41	1.51	3.7
5N	-	Natural[2]	6x365	1	0.43	2.15	5.0
17N	-	Natural[2]	6x365	1	0.53	2.20	4.2
19N	-	Natural[2]	6x365	1	0.42	1.15	2.7
20N	-	Natural[2]	6x365	1	0.47	2.50	5.3
28N	-	Natural[2]	6x365	1	0.38	1.72	4.6
32N	-	Natural[2]	6x365	1	0.54	2.19	4.1
33N	-	Natural[2]	6x365	1	0.40	1.10	2.8
16	2	10	30	2	0.09	1.20	12.6
16	2	100	30	3	0.28	1.68	6.1
16	3	100	30	5	0.31	1.86	5.9
16	5	10	30	1	0.09	1.50	16.7
16	5	100	30	3	0.26	2.15	8.2

For accelerated corrosion tests two types of specimens, mortar samples of 20 × 55 × 80 mm dimensions and concrete samples of 150 × 150 × 400 mm, were built. The diameters of the embedded bars were 6 and 16 mm for the mortar samples and concrete samples, respectively. A cover thickness of 6 mm for the mortar samples and 20 to 50 mm for the concrete samples was considered. In both types, the concrete used had 2% and 3% (by weight) of admixed $CaCl_2$. Anodic current ranging from 10 to 100 $\mu A/cm^2$ was applied to accelerate the corrosion process. The ratio of the maximum to average corrosion attack ranged from 4 to 8 in the natural corrosion tests, and from 5 to 13 in the accelerated tests as summarized in Table 2.5. Based on the frequent obtaining of ratios ranging from 4 to 8, the authors postulated that pit growth proceeds 4 to 8 times faster than the average corrosion rate.

2.5.3 Rodriguez et al. (1997)

Rodriguez et al. (1997) tested a total of 31 beams with dimensions of 2300×200×150 mm with different levels of corrosion. The detailing of the beams, namely the ratios of the tensile and compression reinforcement, was the main design variable. Corrosion of the reinforcement was facilitated by adding 10.5 kg/m^3 of calcium chloride (3% of cement weight) to the mixing water. A current density of 100 μA/cm^2 was used to accelerate the process.

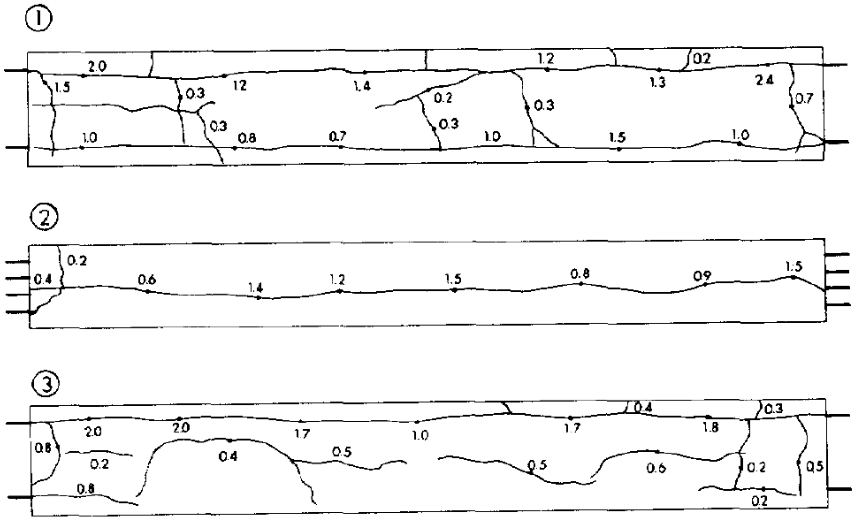

Figure 2.23: Crack map of a corroded beam. Taken from Rodriguez et al (1997)

The mean value of the attack penetration was measured using the gravimetric method. Wherever pitting corrosion occurred, the maximum pit depth was measured geometrically. Noticeably deeper pits were found over the surfaces of the stirrups, possibly due to the lesser cover over them. After having corroded the bars, the beams were loaded up to failure. Regardless of the degree of corrosion, the beams with low tensile reinforcement ratio had a flexural failure. On the other hand, the failure mode of the beams with a high ratio of tensile reinforcement and large stirrups spacing was altered from the crushing of the concrete at the top to a shear failure. The shear failure was attributed to a significant reduction of the transverse reinforcement section area due to pitting. Detailed mapping of cracks caused by corrosion showed a maximum crack width of 2.4 mm parallel to the longitudinal bars as depicted in Figure 2.23. The ratio of the maximum to average corrosion depth of the longitudinal bars, tabulated in Table 2.6, ranged from 2.5 to 4.3 whereas that of the stirrups was noticeably larger, ranging from 6.8 to 8.5.

Table 2.6: Experimental results of Rodriguez et al. (1997)

D (mm)	f’c (MPa)	w/c	Exposure time (days)	Corrosion attack (mm)					
				Longitudinal bars			Stirrups		
				Avg.	Max.	Max./Avg.	Avg.	Max.	Max./Avg.
10	34	0.5	101	0.36	1.00	2.78	0.37	3.00	8.11
10	34	0.5	117	0.45	1.10	2.44	0.39	3.10	7.95
10	34	0.5	160	0.49	1.30	2.65	0.49	3.90	7.96
12	35	0.5	104	0.32	1.30	4.06	0.39	3.10	7.95
12	35	0.5	114	0.35	1.40	4.00	0.39	3.20	8.21
12	35	0.5	163	0.41	1.60	3.90	0.49	3.80	7.76
12	35	0.5	175	0.4	1.60	4.00	0.53	4.50	8.49
12	37	0.5	108	0.32	1.30	4.06	0.34	2.70	7.94
12	37	0.5	116	0.35	1.40	4.00	0.36	2.90	8.06
12	37	0.5	164	0.4	1.60	4.00	0.50	3.80	7.60
12	37	0.5	175	0.39	1.60	4.10	0.53	4.50	8.49
12	35	0.5	108	0.37	1.50	4.05	0.37	2.50	6.76
12	35	0.5	127	0.31	1.20	3.87	0.44	3.50	7.95
12	35	0.5	154	0.43	1.70	3.95	0.52	3.80	7.31
12	35	0.5	181	0.53	2.10	3.96	0.63	5.00	7.94
12	37	0.5	111	0.3	1.30	4.33	0.35	2.80	8.00
12	37	0.5	128	0.48	1.50	3.12	0.50	4.00	8.00
12	37	0.5	164	0.42	1.80	4.29	0.54	4.30	7.96

2.5.4 Torres-Acosta et al. (2003)

Twelve concrete slabs with dimensions of 90 × 190 × 310 mm were tested at the University of South Florida. The slabs contained three #3 (U.S.) plain bars placed 32 mm away from the surface as depicted in Figure 2.24. The concrete mix had a water-cement ratio of 0.42 and was contaminated with chloride. Anodic current was not applied to accelerate the tests. The experiments lasted 700 days, after which the specimens were thoroughly examined.

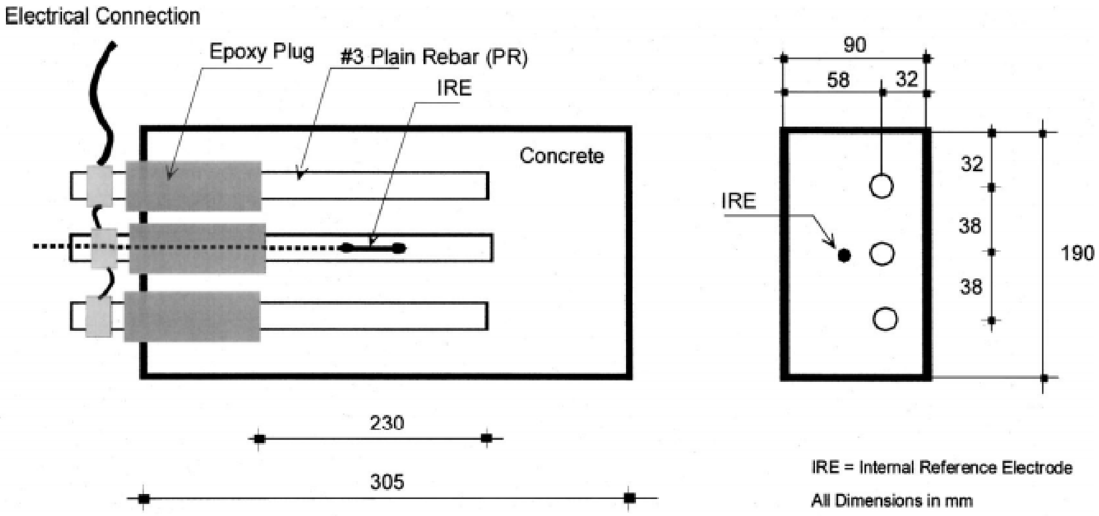

Figure 2.24: Sketch of Torres-Acosta et al. (2003) concrete slabs. Taken from Torres-Acosta et al. (2003)

The average and maximum corrosion attacks were measured by the gravimetric method and a magnifying lens, respectively. The results are graphically summarized in Figure 2.25. The maximum to average corrosion attack ratios had a mean of 5.08 mm and a variance of 4.46 mm^2. The highest ratios were found in the specimens with the smallest corrosion attacks. This can be explained by to the presence of corrosion cracks on the surface of slabs with high corrosion attacks which can cause a more uniform corrosion pattern.

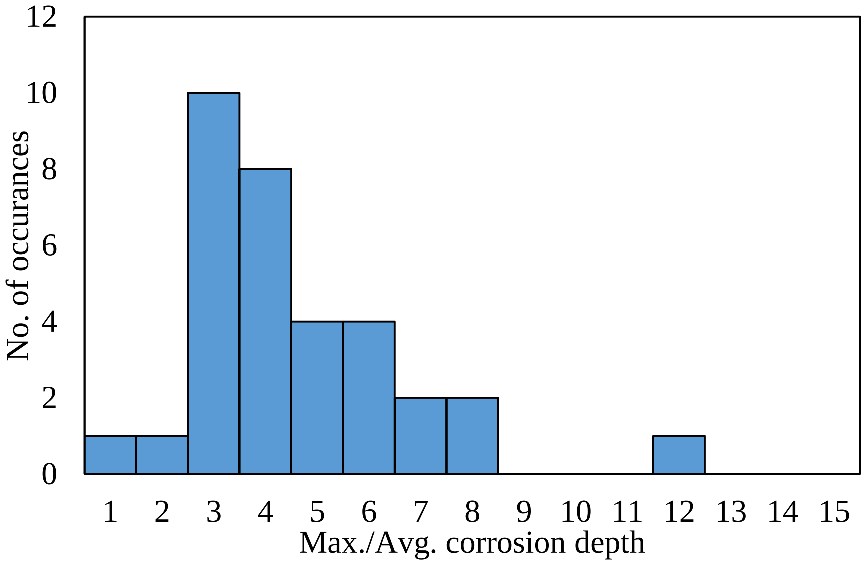

Figure 2.25: The ratio of maximum to average corrosion attack observed in Torres-Acosta et al. (2003) slabs

2.5.5 Cairns et al. (2005)

Cairns et al. (2005) studied the effects of localized corrosion damage on the mechanical properties of reinforcing bars. Pitting corrosion was artificially simulated by removing a section of a bar using a multifluted, hemispherical end mill with cylinder shank. Bars having diameters of 12, 16, 20, and 24 mm were subjected to tensile tests after the removal of 5, 10, 20, 30, 40 and 50% of the nominal area of the bar section as shown in Figure 2.26. The yield and ultimate strengths of the bars were slightly reduced. However, the ductility of the bars with 5 and 50% section loss was reduced by approximately 40% and 80%, respectively. The loss of ductility was attributed to the variability of the attack along the length of the bars.

In the second series of tests, cubic and cylindrical specimens with embedded 16 mm plain and 20 mm deformed bars were built. The cubic specimens were conditioned under a cyclic wetting-drying regime of one day of wetting by 3% NaCl solution followed by 6 days of drying at a relative humidity of 70%. To obtain the test results within a reasonable time, current densities between 0.01 to 0.05 mA/cm^2 were applied to the bars during the drying period. Afterwards, the cylinder specimens were immersed in a 5% salt solution while connected to an anodic potential. The procedure produced a mixture of general and pitting corrosion with varying degrees over the length of the bars (Cairns et al. 2005).

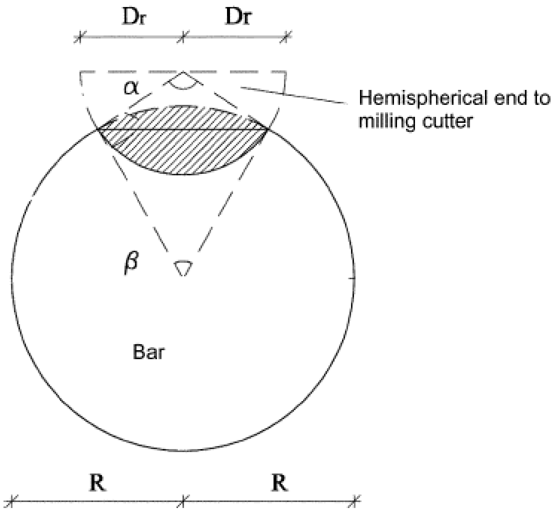

Figure 2.26: Simulated pitting corrosion damage. Taken from Cairns et al. (2005)

Examination of the bars confirmed that pits are circular and the section area lost at a pit can be approximated as π/4 times the depth and breadth of the pit. The average maximum loss of section at a pit was approximately twice the average sectional loss while the ratio of the maximum pit depth to the mean penetration ranged from 10 to 50. In agreement with the findings of Torres-Acosta et al. (2005), this ratio tended to decrease as corrosion progressed, which is depicted in Figure 2.27. From a linear regression analysis, it was found that the ultimate force developed in the bars was reduced by approximately 1% for a 7% cross section loss at a pit. However, the ultimate stress was increased by 5%. The yield stress did not show significant change. The fracture of a reinforcing bar is expected to take place where the steel is weakest. However, the stresses will be overestimated if the location of the deepest pit and the weakest steel are not coincident. Thus, the authors attributed the observed increase in the ultimate stress to the non-uniform material composition over the length of the bar. This increase, in disagreement with the experimental results obtained by other researchers, vanished when the remaining section area was calculated based on the mean section loss instead of the maximum loss.

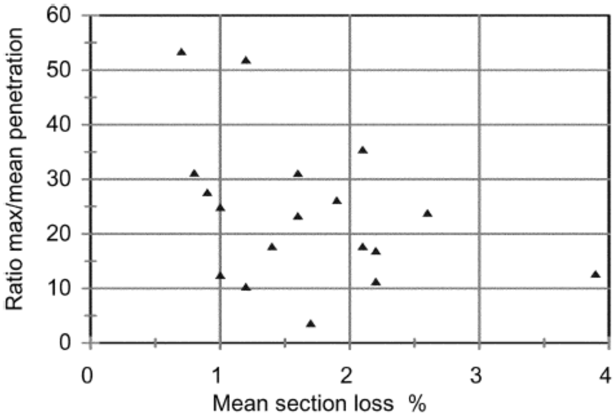

Figure 2.27: Ratio of the maximum to the average corrosion penetration versus the average cross section loss. Taken from Cairns et al. (2005)

2.5.6 Stewart et al. (2008)

Stewart et al. (2008) conducted two series of accelerated corrosion tests on singly-reinforced concrete slabs to study the temporal and spatial variability of pitting corrosion. Specimens were reinforced with 16 and 27 mm diameter bars. Three percent $CaCl_2$ by weight of cement was added to the concrete mix and the specimens were moist cured for 28 days before an anodic current was applied to the reinforcing bars to accelerate the tests. The dimensions of the slabs were 550 × 1000 × 250 mm. The accelerated corrosion test set-up is shown in Figure 2.28.

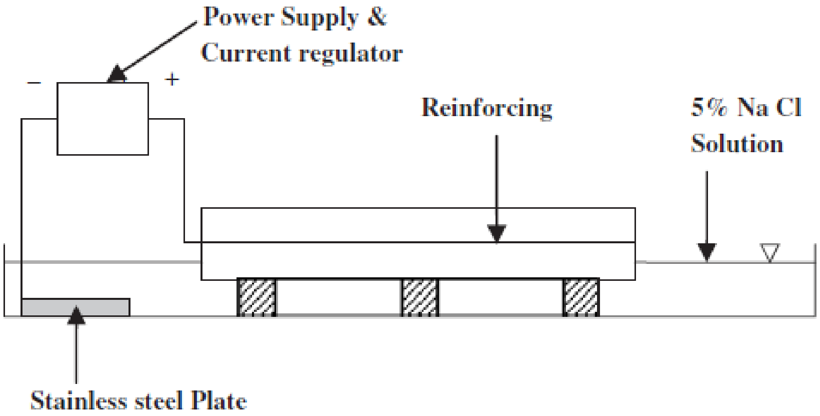

Figure 2.28: Accelerated corrosion test setup. Taken from Stewart et al. (2008)

After completion of the tests, the slabs were broken and corroded bars were cleaned and weighed according to ASTM G1-03. The maximum pit depth was measured for each 100 mm length of the reinforcing bars using a micrometer gauge. The pit density had great scatter with some portions having a single pit while others contained up to six pits at different locations. It was also observed that the ratio of the maximum pit depth to the average corrosion loss decreased with time. The results are summarized in Table 2.7.

Table 2.7: Stewart et al. (2008) experimental results. Taken from Stewart et al. (2008)

Specimen	i_{corr} (μA/cm^2)	L (mm)	Diameter (mm)	Time (days)	No. of samples	Max./Avg. corrosion attack	
						Mean	COV
1	160-185	100	16	78	32	6.2	0.18
2	125-150	100	27	78	32	7.1	0.17

Using the inverse cumulative distribution function (CDF^{-1}) method, Stewart et al. (2008) fitted a range of probability distributions to the pitting data. It was concluded that the Gumbel distribution provides the best fit for the ratio of the maximum corrosion attack to the average corrosion penetration.

2.5.7 Apostolopolous et al. (2013)

Apostolopolous et al. (2013) tested the tensile properties of bare and embedded-in-concrete B500c bars of 8 mm diameter. Bare bars were exposed to salt-spray for a period of up to 120 days. The bars embedded in concrete were salt sprayed for one year. At different time intervals the tensile strength of the specimens was tested and the mass loss due to corrosion was measured. An almost linear reduction of mass, yield strength, ultimate stress, and uniform elongation of the bars was observed. The ductility of the bars had the most significant degradation. For the same mass loss, the bare bars had less reduction of the mechanical properties. Due to the surrounding concrete cover, corrosion damage to embedded bars was in favour of pitting corrosion (Apostolopoulos et al., 2013). Three-dimensional surface plots of the pits, illustrated in Figure 2.29, suggest that the idealization of the shape of a pit in the form shown in Figure 2.26 may not be a reasonable assumption. The spatial non-uniformity of corrosion damage is also evident from the measured values of pit depths and areas presented in Table 2.8.

Table 2.8: Pit depth and area of bars subjected to pitting corrosion. Taken from Apostolopolous et al. (2013)

		Bare bar	Embedded bar
Pit depth (mm)	Minimum (d_{min})	0.23	0.36
	Average (d_{avg})	0.27	0.47
	Maximum (d_{max})	0.32	0.59
Area (mm^2)	Minimum (A_{min})	0.70	0.64
	Average (A_{avg})	2.42	7.14
	Maximum (A_{max})	7.64	29.83

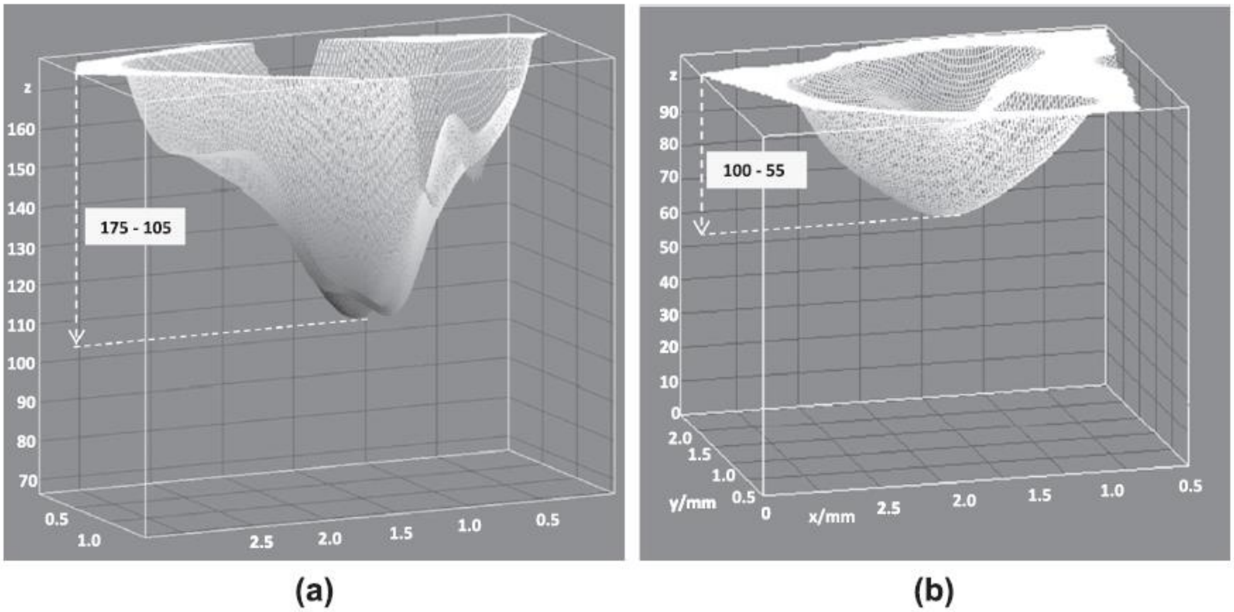

Figure 2.29: 3D surface plots of pits of corroded (a) embedded and (b) bare bars. Taken from Apostolopolous et al. (2013)

3 Implemented Models and VecTor Methodology

This chapter describes the models added to VecTor2, the software used for finite element modeling of corroded structures. VecTor2 is a nonlinear finite element program developed at the University of Toronto which can be used for analysis of two-dimensional reinforced concrete membrane structures. The formulations added to VecTor2 account for the degrading effects of corrosion through a reduction in the steel cross-sectional area and bond strength, and by inducing tensile strains in the cover concrete due to the expansive nature of corrosion products. The formulations pertaining to two types of corrosion, namely uniform and pitting corrosion, and the methods used to verify the implementation of each are discussed in the subsequent sections.

3.1 Rate of Corrosion

Once the protective layer around the reinforcement is broken down by either chloride attack or carbonation of the cover concrete, the rate of corrosion determines the degree of reinforcing steel cross-sectional loss (Andrade et al., 1993). It's also the main input of many corrosion damage prediction models. The reduction in the diameter of the reinforcement, the bond strength, the area of the pits formed over the reinforcing bars, and the extent of cover cracking are defined by the corrosion attack penetration which is directly proportional to the corrosion rate. VecTor2 models the reinforcing bars with truss elements. In order to distinguish a normal truss element from a corroding truss element, a new material type, corroded reinforcing steel, was added to the materials library of VecTor2. Employing Faraday's law, the rate of corrosion can be expressed as the loss of metal per unit of surface area per unit of time (Alonso et al., 1998):

$$Corrosion\ rate = \frac{dr_b}{dt} = i_{corr}/nF \tag{3.1}$$

where:

- i_{corr} = corrosion current density ($\frac{A}{m^2}$)
- F = Faraday constant (96494 $\frac{C}{mol\ .e^-}$ or $\frac{A.s}{mol\ .e^-}$)
- n = electrons per mole of iron

For $i_{corr} = 1\mu A/cm^2$:

$$\frac{dr_b}{dt} = \frac{1\cdot 10^{-6}\left(\frac{A}{cm^2}\right)\cdot 55.85\left(\frac{g}{mol\ Fe}\right)\cdot 86400\left(\frac{s}{day}\right)\cdot \frac{1}{7.86}\left(\frac{cm^3}{g}\right)\cdot 365\left(\frac{day}{year}\right)}{2\left(\frac{mol\ e^-}{mol\ Fe}\right)\cdot 96494\left(\frac{A.s}{mol\ e^-}\right)} = 0.0116\left(\frac{mm}{year}\right)$$

Thus:

$$\frac{dr_b}{dt} = 0.0116.\, i_{corr}(\frac{mm}{year}) \tag{3.2}$$

Note that the corrosion current density, i_{corr}, should be expressed with the unit $\mu A/cm^2$ which is the typical unit used in accelerated corrosion tests. Assuming that the corrosion rate (or corrosion current density) is time invariant, Eq. 3.3 can be used to evaluate the remaining diameter of a rebar after t years of uniform corrosion.

$$d_b(t) = d_{b0} - 0.0232.\, i_{corr}.\, t \quad (mm) \tag{3.3}$$

In the case of pitting corrosion, the cross-sectional area of the reinforcing steel is locally reduced. The formulation suggested by Stewart and Al-Harthy (2008), expressed in Eq. 3.4, was employed to calculate the reduced steel cross-sectional area. A pitting factor R, defined as the ratio of the maximum pit depth to the corrosion penetration calculated based on uniform corrosion, is used to define the degree of pitting.

$$R = p/P_{avg} \tag{3.4}$$

where:

- R = pitting factor
- P_{avg} = corrosion penetration calculated based on uniform corrosion
- p = maximum pit depth

The pit configuration shown in Figure 3.1 is used to predict the cross-sectional area of the pit as follows:

$$A_{pit} = \begin{cases} A_1 + A_2 & p \leq \frac{D_0}{\sqrt{2}} \\ \frac{\pi D_0^2}{4} - A_1 + A_2 & \frac{D_0}{\sqrt{2}} \leq p \leq D_0 \\ \frac{\pi D_0^2}{4} & p \geq D_0 \end{cases} \tag{3.5}$$

where:

- $b = 2p\sqrt{1 - (\frac{p}{D_0})^2}$
- $A_1 = 0.5(\theta_1 \left(\frac{D_0}{2}\right)^2 - b\left|\frac{D_0}{2} - \frac{p^2}{D_0}\right|)$
- $A_2 = 0.5(\theta_2 p^2 - b\frac{p^2}{D_0})$
- $\theta_1 = 2\arcsin(\frac{b}{D_0})$
- $\theta_2 = 2\arcsin(\frac{b}{2p})$

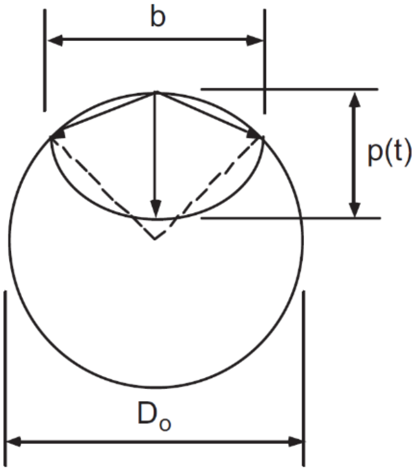

Figure 3.1: Pit configuration. Taken from Stewart and Al-Harthy (2008)

Despite the common assumption of a constant corrosion rate made in the previous formulations, Liu and Weyers (1998) suggested that the rate of corrosion is inversely proportional to the ionic diffusion distance. Thus, as the thickness of the produced rust layer increases, the rate of rust production (or corrosion) decreases (Bhargava et al., 2005). In their formulation, growth of rust products is given by:

$$\frac{dW_{rust}}{dt} = \frac{k_p}{W_{rust}} \tag{3.6}$$

where:

- k_p = $2.59 \times 10^{-6}(\frac{1}{\alpha})\pi d_{bo} i_{corr}$
- W_{rust} = weight of rust products (lb/ft)
- α = ratio of molecular weight of rust to that of iron

Using Eq. 3.6 to calculate the weight of the produced rust, W_{rust}, the weight of the consumed steel, W_s, can be evaluated from Eq. 3.7 where α is the ratio of the molecular weight of rust to that of iron, given in Table 3.1 for common types of rust.

$$W_s = \frac{W_{rust}}{\alpha} \tag{3.7}$$

Table 3.1: Ratio of molecular weight of common corrosion products to that of iron (Bhargava et al., 2005)

Corrosion product	α
FeO	0.777
Fe_3O_4	0.724
Fe_2O_3	0.699
$Fe(OH)_2$	0.622
$Fe(OH)_3$	0.523
$Fe(OH)_3.3H_2O$	0.347

3.1.1 Sample Calculation

Utilizing the formulations explained in the previous section, a sample calculation for a corroded rebar, under the assumption of uniform corrosion, with the following properties were done. Figure 3.2 illustrates the evolution of cross section loss with time.

- $d_{b0} = 16\ mm$
- $i_{corr} = 100 \frac{\mu A}{cm^2}$ (equivalent to a corrosion rate of 1.16 mm/year)
- $\alpha = 0.523$
- $\rho_s = 7.85 \times 10^{-3}\ \frac{gr}{mm^3}$

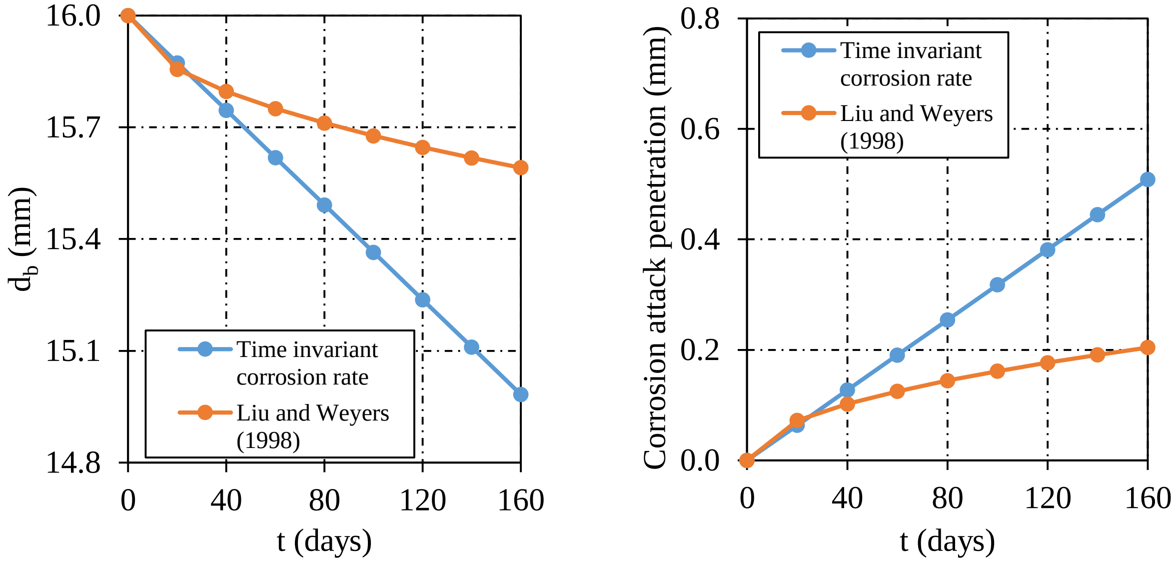

Figure 3.2: Reduced diameter of a corroded rebar (left), Corrosion attack penetration (right) versus time

The results of two experiments, chosen from the literature, were used to assess the accuracy of Faraday's law and the formulation suggested by Liu and Weyers (1998). Rodriguez et al. (1997)

conducted accelerated corrosion tests on five beams with dimensions of 2300×200×150 mm. 3% calcium chloride by weight of cement was added to the mixing water and a current density of $100\,\mu A/cm^2$ was used to accelerate the tests. The mean value of the attack penetration was measured using the gravimetric method (i.e. weighing the bars before and after the tests). Maaddawy and Soudki (2003) tested 12 concrete prisms reinforced with two No. 10 bars. Depassivation of the reinforcing bars was done by adding 5% NaCl by weight of cement to the concrete mixture. Results of the Maaddawy et al. (2003) and Rodriguez et al. (1997) experiments are presented in Table 3.2 and Table 3.3, respectively.

Table 3.2: Mass loss of reinforcing bars corroded with different corrosion current densities (Maaddawy and Soudki, 2003)

Group	Specimen	Current density ($\mu A/cm^2$)	Corrosion time (hr)	Mass loss (%)	
				Bar 1	Bar 2
[A]	P-D	100	815	3.87	5.57
	K-R	100	815	4.31	4.12
	H-G	100	815	3.87	4.55
[B]	M-Z	200	766	7.75	7.29
	X-B	200	766	6.57	7.30
	C-O	200	766	7.17	7.73
[C]	N-A	350	380	6.63	7.01
	E-I	350	380	6.16	6.58
	T-Y	350	380	6.14	6.46
[D]	U-F	500	306	8.35	5.98
	L-V	500	306	7.36	6.98
	J-Q	500	306	7.11	7.76

The values of corrosion attack penetration calculated with Faraday's law and Liu and Weyers' (1998) model are shown in Figure 3.3. On average the errors associated with Faraday's law predictions were 8.8% and 5.3% while that of Liu and Weyers' (1998) model were 33.7% and 20.9% for the values extracted from the Maaddawy and Soudki (2003) and Rodriguez et al. (1997) experiments, respectively. Thus, it was concluded that the formulation based on the assumption of a time invariant corrosion rate is more accurate than the Liu and Weyers' (1998) model. However, further investigation is required as several utilizations of the second model have been reported in the literature. Moreover, the experiments used here were all done in a short period of time with minor corrosion damage. The assumption of a linear reduction of diameter throughout the life of a corroding member seems unrealistic unless the rate of corrosion is constantly controlled in a laboratory test. For the sake of consistency, only the formulation based on time invariant corrosion rate is used in the remainder of this thesis.

Table 3.3: Corrosion attack penetration of reinforcing bars corroded in an accelerated corrosion test (Rodriguez et al., 1997)

D_0 (mm)	Corrosion time (day)	Corrosion penetration (mm)	D_0 (mm)	Corrosion time (day)	Corrosion penetration (mm)	D_0 (mm)	Corrosion time (day)	Corrosion penetration (mm)
12	149	0.54	8	149	0.26	6	149	0.37
10	101	0.36	8	101	0.52	6	101	0.39
10	117	0.45	8	117	0.56	6	117	0.49
10	160	0.49	8	160	0.56	6	160	0.49
12	104	0.32	8	104	0.27	6	104	0.39
12	115	0.35	8	115	0.44	6	115	0.39
12	163	0.41	8	163	0.57	6	163	0.49
12	175	0.4	8	175	0.41	6	175	0.53
12	108	0.32	8	108	0.3	6	108	0.34
12	116	0.35	8	116	0.31	6	116	0.36
12	164	0.40	8	164	0.43	6	164	0.5
12	175	0.39	8	175	0.56	6	175	0.53
12	108	0.37	8	108	0.24	6	108	0.37
12	127	0.31	8	127	0.35	6	127	0.44
12	154	0.43	8	154	0.38	6	154	0.52
12	181	0.53	8	181	0.47	6	181	0.63
12	111	0.3	8	111	0.20	6	111	0.35
12	128	0.48	8	128	0.26	6	128	0.50
12	164	0.42	8	164	0.37	6	164	0.54

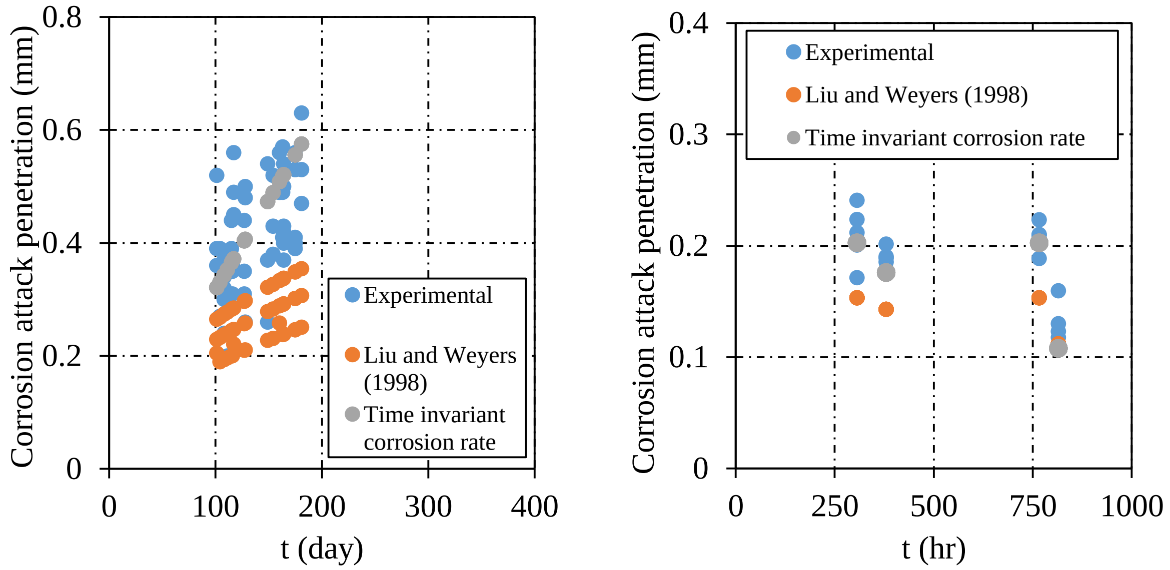

Figure 3.3: Predicted corrosion attack penetration with Faraday's law and Liu and Weyers (1998) model

3.2 Cover Cracking

Many of the empirical, analytical, and numerical models for cracking of the cover concrete caused by corrosion of the steel reinforcement are based on the assumption of the formation of a circular rust layer around the corroded rebar. The stresses induced in the cover concrete are typically calculated by employing the formulations of a thick-wall cylinder under uniform internal pressure. Other than the expansive nature of the corrosion products, other factors also influence the cracking of cover concrete. A decisive factor in this regard is the existence of a porous network around the steel-concrete interfacial zone referred to as the 'diffusion' or 'porous' zone (Angst et al., 2012). This region should be completely filled with corrosion products before any internal pressure can be applied to the cover concrete. The diffusion zone can be modelled as a hollow cylinder around the corroded rebar with a thickness of 100-200 μm (Angst, 2011). In addition, penetration of the corrosion products into the radial cracks formed in the cover reduces the net volume of the rust that applies pressure to the cover concrete. Thus, from the total amount of produced rust, only the net volume of corrosion products, given in Eq. 3.8, contributes to cracking of the cover concrete.

$$V_{net} = V_{produced\,rust} - V_{radial\,cracks} - V_{diffusion\,zone} \tag{3.8}$$

The service life of a corroding reinforced concrete structure is typically divided into three stages. At the beginning, the high alkalinity of the hydration products of the cement results in the formation of a very thin layer of iron hydroxide around the reinforcement. In the first stage, the chloride or carbon dioxide content of the cover concrete reaches a threshold value enough to reduce the alkalinity of the concrete pore solution to the point where the protective iron hydroxide layer is destabilized, exposing the surface of the reinforcement to corrosion. Once enough oxygen and moisture are present, this stage ends and the reinforcing steel starts to corrode. This stage can be simulated by employing Fick's law of diffusion. In the second phase, also referred to as free expansion of corrosion products, solid iron is transformed to ferrous or ferric ions, accumulating in the diffusion zone. Thus, there are no stresses developed in the cover concrete during this stage. Once the diffusion zone is filled with rust, the third stage starts. During this stage tensile stresses are developed in the cover concrete due to corrosion of the reinforcing steel. Radial cracks form and propagate in the concrete surrounding the reinforcement until a serviceability limit state such as the spalling or delamination of the cover concrete occurs. Throughout this thesis and in the formulations added to VecTor2, only the third stage of the service life was considered. Corrosion induced cracking was treated as an initial strain generated in the elements in the vicinity of a corroded reinforcing bar. The first and second stage were not included for two main reasons. First, the first stage is typically bypassed in the accelerated corrosion tests by the addition of a chlorine compound in excess of the minimum threshold value required for steel depassivation to the concrete mixture. Second, there is great disagreement between the reported volumes of the porous zone around the reinforcement in the literature. In addition, the total time of the first and second stages can be treated as a time shift in the service life of a corroded RC member. The current implementation consists of two models embodied in VecTor2:

1. Wang and Liu (2004)
2. Pantazopoulou and Papoulia (2001)

The formulation of the models and their implementation in VecTor2 are explained in the following sections.

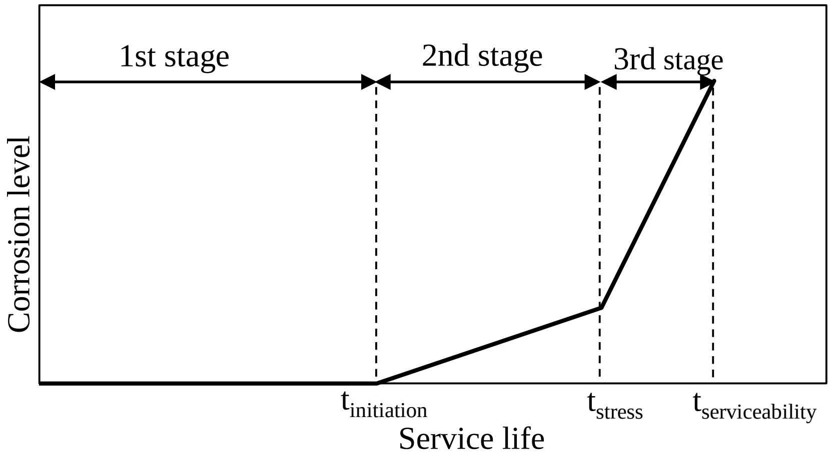

Figure 3.4: Service life of a corroding reinforced concrete member

3.2.1 Wang and Liu (2004)

The formulation of Wang and Liu (2004) treats the cover concrete as two thick-wall cylinders under uniform internal pressure. At any time during the third stage, the inner cylinder is cracked while the outer one is not cracked. Cracking of the concrete is modelled by a bilinear softening branch which concludes at a hoop tensile strain corresponding to zero tensile strength as shown in Figure 3.5 and formulated in Eq. 3.9. The softening modulus is calculated based on fracture energy, the energy dissipated per unit length of a localized crack (Pantazopoulou and Papoulia, 2001).

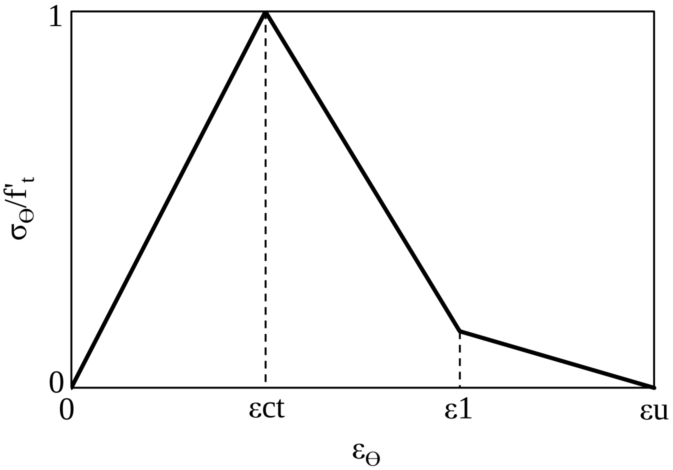

Figure 3.5: Bilinear tension softening behaviour of plain concrete in tension

$$\begin{cases} \sigma_\theta(r) = E_c\varepsilon_\theta(r) & \varepsilon_\theta \le \varepsilon_{ct} \\ \sigma_\theta(r) = f_t'\left[1 - 0.85\dfrac{\varepsilon_\theta(r) - \varepsilon_{ct}}{\varepsilon_1 - \varepsilon_{ct}}\right] & \varepsilon_{ct} < \varepsilon_\theta(r) \le \varepsilon_1 \\ \sigma_\theta(r) = 0.15f_t'\dfrac{\varepsilon_u - \varepsilon_\theta(r)}{\varepsilon_u - \varepsilon_1} & \varepsilon_1 < \varepsilon_\theta(r) \le \varepsilon_u \end{cases} \tag{3.9}$$

From the CEB-FIP (1990) model code, the fracture energy, G_f , is defined by Eq. 3.10 where G_{fo} is the base value for fracture energy, f_{cm} is the mean compressive strength of concrete ($f_{cm} < 80\ MPa$), and f_{cmo} is taken as 10 MPa (Pantazopoulou and Papoulia, 2001).

$$G_f = G_{fo}(\frac{f_{cm}}{f_{cmo}})^{0.7} \quad (N/mm) \tag{3.10}$$

Crack openings corresponding to ε_1 and ε_u are given by Eq. 3.11 and Eq. 3.12. The values of G_{fo} and α_F are evaluated based on the maximum aggregate sizes given in Table 3.4.

$$w_u = \alpha_F\frac{G_f}{f_t'} \tag{3.11}$$

$$w_1 = 2\frac{G_f}{f_t'} - 0.15w_u \tag{3.12}$$

Table 3.4: Base fracture energy and α_F (Hilsdorf, 1991)

Max. aggregate size (mm)	G_{Fo} (N/mm)	α_F
8	0.025	8
16	0.030	7
32	0.058	5

Assuming that the characteristic crack band width, h_c, is equal to five times the maximum aggregate size, the coordinates of the points on the softening branch in Figure 3.5 are defined by Eq. 3.13 and Eq. 3.14 (Bazant, 1983).

$$\varepsilon_1 = \frac{w_1}{h_c} \tag{3.13}$$

$$\varepsilon_u = \frac{w_u}{h_c} \tag{3.14}$$

The total volume of produced rust, V_{rust}, is calculated as the sum of the part that penetrates into the radial cracks formed in the cover, V_{crack}, and the part that applies radial pressure to the cover concrete, V_{net}, as given in Eq. 3.15 where t_r is the thickness of rust layer, R_s is the reduced radius of the reinforcing bar, R_r is the radius of the reinforcing bar and the rust around it, $\sum w$ is the theoretical radial crack opening, and R_i is the radius up to which the cover is cracked (at R_i, $\varepsilon_\theta = f_t/E_c$).

$$V_{rust} = V_{net} + V_{crack} = \pi t_r(2R_s + t_r) + (\sum w)(R_i - R_r)/2 \tag{3.15}$$

The second term in Eq. 3.15 accounts for the volume of rust that penetrates into the radial cracks. Although cracking of the cover concrete is modelled as a smeared cracking process in this formulation, V_{crack} is calculated based on a theoretical model of a single radial crack shown in Figure 3.6. Reduction of the radius of the reinforcing steel and the necessary radial displacement of the steel-concrete interface are referred to as x and u_r. Thus, the dashed circle in Figure 3.6, which shows the initial location of the steel-concrete interface, should be elongated relative to its perimeter by $2\pi u_r$. If the strain caused by this deformation is greater than the cracking strain of concrete, this increase in the perimeter will be compensated for by a radial crack opening equal to $2\pi u_r$ as expressed in Eq. 3.16. Utilizing the law of conservation of mass, the total volume of rust can also be calculated based on the volume of consumed steel in corrosion reaction as given by Eq. 3.17.

$$\sum w = 2\pi u_r(R_0) = 2\pi(R_r - R_0) \tag{3.16}$$

$$V_{rust} = \alpha_1 \Delta V_{steel} = \alpha_1 \pi(2R_0 x - x^2) \tag{3.17}$$

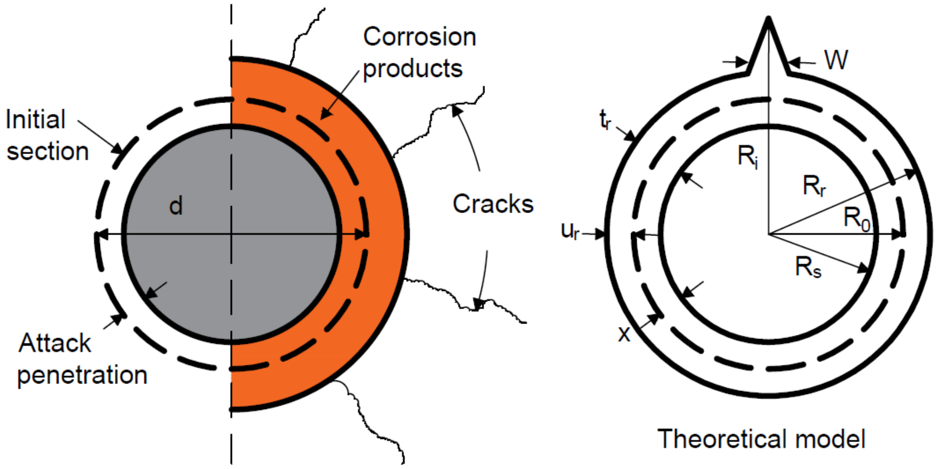

Figure 3.6: Theoretical model of cover cracking

By equating Eq. 3.15 and Eq. 3.17 the thickness of the rust layer, t_r, can be quantified as a function of the corrosion attack penetration, x, as follows :

$$t_r = \frac{\alpha_1(2R_0x - x^2) + x(R_i - R_0 + x)}{R_i + R_0} \tag{3.18}$$

The radial displacement of the steel-concrete interface should be large enough to accommodate the increase in the volume of the iron that is transformed to rust. Thus, treating this physical interpretation of corrosion reaction as a boundary condition, $u(R_0)$ should be equal to $t_r - x$:

$$u(R_0) = t_r - x = \frac{(\alpha_1 - 1)(2R_0x - x^2)}{R_i + R_0} \tag{3.19}$$

The radial displacement at any radius is given by:

$$u(r) = \frac{f_t'}{E_c}.r.\frac{(R_c/r)^2 + 1}{(R_c/R_i)^2 + 1} \tag{3.20}$$

It is assumed that the radial displacement in the inner cracked cylinder follows the same pattern as the elastic part. Consequently, when the cover concrete is not fully cracked ($R_i \leq R_c$), the radius of cracked concrete, R_i, can be obtained by calculating the thickness of the rust layer and equating Eq. 3.19 and Eq. 3.20 for $r = R_0$. Having the radial displacement defined as a function of radius, the tangential strain is simply:

$$\varepsilon_\theta(r) = \frac{u(r)}{r} = \frac{f_t'}{E_c} . \frac{(R_c/r)^2 + 1}{(R_c/R_i)^2 + 1} \quad (3.21)$$

At this point the pressure that corrosion products apply to the cover, p_{corr}, can be calculated from Eq. 3.22.

$$p_{corr} . R_0 = f_t' \frac{R_c^2 - R_i^2}{R_c^2 + R_i^2} . R_i + \int_{R_0}^{R_i} \sigma_\theta(r) d_r \quad (3.22)$$

The integration on the tangential stresses is approximated by calculating two other variables defined as:

$$RR1 = \frac{R_c}{\sqrt{\varepsilon_1 . \frac{E_0}{f_t'} . \left[\left(\frac{R_c}{R_i} \right)^2 + 1 \right] - 1}} \quad (3.23)$$

$$RRu = \frac{R_c}{\sqrt{\varepsilon_u . \frac{E_0}{f_t'} . \left[\left(\frac{R_c}{R_i} \right)^2 + 1 \right] - 1}} \quad (3.24)$$

where $RR1$ is defined as the radial distance where the hoop strain reaches ε_1 (σ_θ=0.15f'_t) and RRu is the radial distance where the hoop strain reaches ε_u (σ_θ=0). Thus, Eq. 3.22 can be reformulated as follows:

$$p_{corr} . R_0 = f_t' \frac{R_c^2 - R_i^2}{R_c^2 + R_i^2} . R_i + \frac{1.15 f_t'}{2} (R_i - RR1) + \frac{0.15 f_t'}{2} (RR1 - RRu) \quad (3.25)$$

When the cover is fully cracked, $R_i = R_c$ and the radial displacement is given by:

$$u(r) = \varepsilon_{\theta c} . r . \frac{(R_c/r)^2 + 1}{2} \quad (3.26)$$

where $\varepsilon_{\theta c}$ is the hoop strain at $r = R_c$. In order to calculate $\varepsilon_{\theta c}$, the same boundary condition is used and Eq. 3.19 and Eq. 3.26 are equated and solved for $\varepsilon_{\theta c}$. Because at this stage the outer radius of the cracked inner cylinder is constant and equal to R_c, and because the hoop strain at the interface of the inner cracked and outer elastic cylinders is $\varepsilon_{\theta c}$, Eq. 3.23 and Eq. 3.24 can be simplified to:

$$RR1 = \frac{R_c}{\sqrt{\frac{2\varepsilon_1}{\varepsilon_{\theta c}} - 1}} \tag{3.27}$$

$$RRu = \frac{R_c}{\sqrt{\frac{2\varepsilon_u}{\varepsilon_{\theta c}} - 1}} \tag{3.28}$$

3.2.1.1Sample Calculation

A sample calculation using the formulation of Wang and Liu (2004) for a corroded reinforcing bar with a radius of 8 mm and a clear cover of 76 mm was performed. A corrosion rate of 20.9 mm/year equivalent to a corrosion current density of 1.8 µA/cm^2 was assumed. The cover concrete had a compressive strength of 31 MPa, a tensile strength of 3.3 MPa, and a modulus of elasticity of 27000 MPa. The ratio of the volume of unit mass of rust to that of iron, referred to as expansion ratio, was taken as 3.75. The computed radius of the radial crack, $RR1$, and RRu for a time span of 100 years are shown in Figure 3.7. The cover concrete starts to crack at 6 days. The cracks reach the surface of the cover in 5.75 years. However, it takes about 80 years for the hoop strain of the external surface of the cover concrete to reach ε_u. The internal pressure starts to build up rapidly and reaches its maximum value when the outer surface of the cover is about to crack. Three important points at which the surface strain reaches ε_{ct}, ε_1, and ε_u are shown in Figure 3.8.

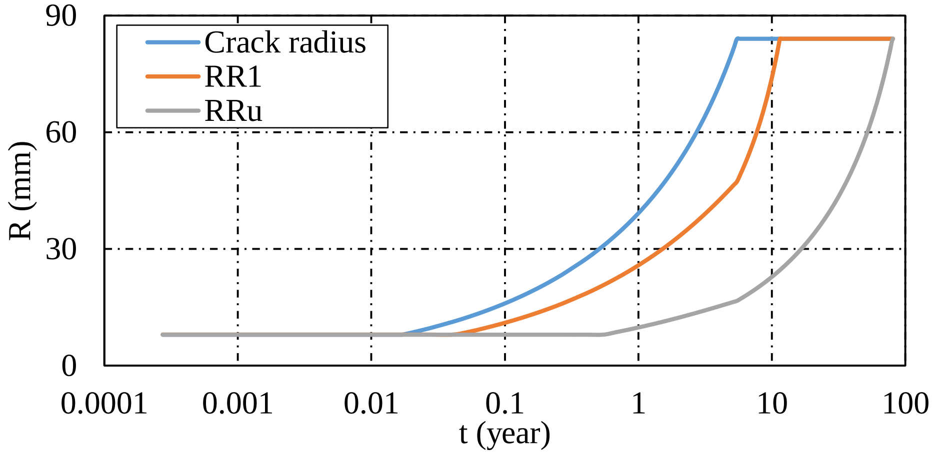

Figure 3.7: Evolution of crack radius, RR1, and RRU with time

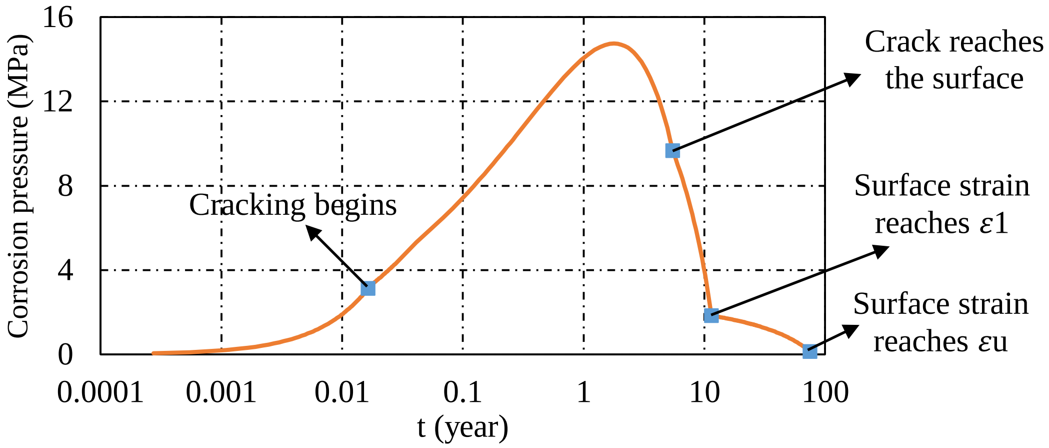

Figure 3.8: Internal pressure applied to the cover concrete by expansive corrosion products

The formulation by Wang and Liu (2004) was used against the experiments of Liu and Weyers (1998), shown in Table 3.5, to calculate the time it takes for the radial cracks to reach the surface. This time is referred to as the time to cover cracking, t_{cr}, and marks an important point in the service life of a corroding structure. The predcited t_{cr} for each specimen versus the observed time of cover cracking reported by Liu and Weyers (1998) are shown in Table 3.6.

Table 3.5: Specimens of Liu and Weyers (1998)

Specimen	Reinforcing bar diameter (mm)	Cover depth (mm)	Corrosion rate (μm/year)	Observed t_{cr} ($year$)
1	16	47.5	27.26	1.84
2	16	69.5	20.88	3.54
3	16	27.2	43.73	0.72
4	12.7	52.0	20.88	2.38

Table 3.6: Predicted time of cover cracking

Specimen	α_1						Observed
	1.80	2.00	2.20	3.75	4.20	6.40	t_{cr} ($year$)
1	4.40	3.52	2.93	1.27	1.09	0.65	1.84
2	15.13	12.06	10.02	4.34	3.72	2.20	3.54
3	0.77	0.61	0.51	0.22	0.19	0.11	0.72
4	10.28	8.20	6.82	2.96	2.54	1.50	2.38

For each specimen, t_{cr} falls within a wide interval based on the assumed type of corrosion product (or the assumed value of expansion ratio α_1). As a result, no conclusions can be made about the accuracy of the employed formulation. This shows a requirement for calibration of the cover cracking models, by identifying the type of corrosion product produced. A simple method for evaluation of the type of rust cannot be found in the literature. Most of the methods are related to the field of chemical engineering and utilizing them requires expertise in that field. The method proposed here for identifying the type of rust is measurement of the density of the produced rust. The densities of the main corrosion products are shown in Table 3.7. They can be divided into two groups: the first group consists of FeO, Fe_3O_4, and Fe_2O_3 having an average density of 5.38 ($\frac{gr}{cm^3}$); the second group consists of $Fe(OH)_2$, $Fe(OH)_3$, and $Fe(OH)_3.3H_2O$ with an average density equal to 3.49 ($\frac{gr}{cm^3}$). Having the density of the produced rust, α_1 can be chosen more accurately and any necessary calibrations or changes to the available models in the literature can be identified. Also it is noteworthy that the produced rust is typically a compound of different types of rust. However, the procedure suggested here can give a rough but helpful estimation of the composition of rust.

Table 3.7: Density of the corrosion products

Corrosion product	FeO	Fe_3O_4	Fe_2O_3	$Fe(OH)_2$	$Fe(OH)_3$	$Fe(OH)_3 \cdot 3H_2O$
ρ_{rust} ($\frac{gr}{cm^3}$)	5.61	5.42	5.10	3.36	3.57	3.53

3.2.2 Pantazopoulou and Papoulia (2001)

Pantazopoulou and Papoulia (2001) modelled the cracking of cover concrete with a finite difference scheme in which the cover thickness is discretized into N segments as illustrated in Figure 3.9. A mesh-centered grid is assumed and the governing differential equation of a hollow cylinder under uniform internal pressure, Eq. 3.29, is solved for the points on the cover simultaneously. In order to define Eq. 3.29 in a finite difference form, the radial and tangential stresses are defined as a function of the strains in Eq. 3.30 and Eq. 3.31 and the radial and tangential strains are given as a function of the radial displacements as shown in Eq. 3.32. Substituting Eq. 3.30, Eq. 3.31, and Eq. 3.32 into Eq. 3.29, the equilibrium equation simplifies to Eq. 3.33. Utilizing the central difference approximation of the derivatives given in Eq. 3.34 and Eq. 3.35, Eq. 3.33 can be expressed in a finite difference scheme as shown in Eq. 3.36.

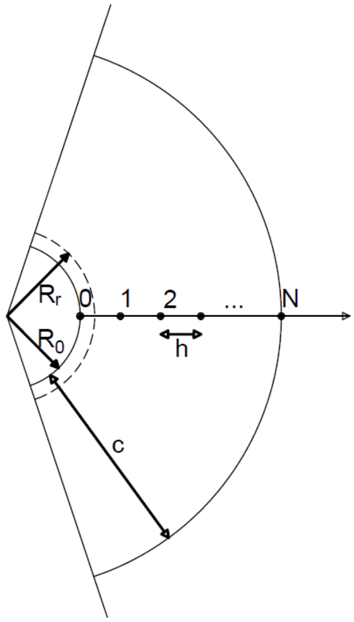

Figure 3.9: Discretization of the cover concrete

$$\sigma_r + \frac{d\sigma_r}{dr} r - \sigma_\theta = 0 \tag{3.29}$$

$$\sigma_r = \frac{1}{1 - \nu_{r\theta}\nu_{\theta r}} (E_r \varepsilon_r + \nu_{r\theta} E_\theta \varepsilon_\theta) \tag{3.30}$$

$$\sigma_\theta = \frac{1}{1 - \nu_{r\theta}\nu_{\theta r}} (E_\theta \varepsilon_\theta + \nu_{\theta r} E_r \varepsilon_r) \tag{3.31}$$

$$\varepsilon_r = \frac{du_r}{dr} \quad \& \quad \varepsilon_\theta = \frac{u_r}{r} \tag{3.32}$$

$$\frac{d^2 u_r}{dr^2} + \frac{1}{r} \cdot \frac{du_r}{dr} - \frac{u_r}{r^2} \cdot \frac{E_\theta}{E_r} = 0 \tag{3.33}$$

$$\frac{du_r}{dr} = \frac{u_{r,i+1} - u_{r,i-1}}{2h} \tag{3.34}$$

$$\frac{d^2 u_r}{dr^2} = \frac{u_{r,i+1} - 2u_{r,i} + u_{r,i-1}}{h^2} \tag{3.35}$$

$$u_{r,i-1}\left(\frac{1}{h^2}-\frac{1}{2r_ih}\right)-u_{r,i}\left(\frac{2}{h^2}+\frac{1}{r_i^2}\cdot\frac{E_{\theta,i}}{E_{r,i}}\right)+u_{r,i+1}\left(\frac{1}{h^2}+\frac{1}{2r_ih}\right)=0 \tag{3.36}$$

Eq. 3.36 can be expressed in a matrix form as defined in Eq. 3.37 where the stiffness matrix, $[K]$, is given by Eq.3.39 and $\{B\}$ is given by Eq. 3.38. The matrix $\{B\}$ defines the boundary conditions of the problem which are $u_r(R_0) = R_r - R_0$ (i.e. the steel-concrete interface should be radially displaced to accommodate the produced rust) and $\sigma_r(R_c) = 0$. Thus, given R_r, the radial displacements through the width of the cover concrete can be calculated by solving Eq. 3.37. The bilinear tension softening model shown in Figure 3.5 can be used to evaluate the radial and tangential stiffness of every point. An iterative procedure should be undertaken to update the secant stiffness of every point until the average change of the secant stiffness in two subsequent iterations is negligible.

$$[K]\{u_r\}^T = \{B\} \tag{3.37}$$

$$\{B\}^T = \{(R_r - R_0)\left(\frac{1}{h^2}-\frac{1}{2r_1h}\right) \quad 0 \quad 0 \;\; . \; . \; . \;\; 0\} \tag{3.38}$$

$$[K]=\begin{bmatrix} (\frac{2}{h^2}+\frac{1}{r_1^2}\cdot\frac{E_{\theta,1}}{E_{r,1}}) & -(\frac{1}{h^2}+\frac{1}{2r_1h}) & 0 & 0 & \cdots & 0 \\ -(\frac{1}{h^2}-\frac{1}{2r_2h}) & (\frac{2}{h^2}+\frac{1}{r_2^2}\cdot\frac{E_{\theta,2}}{E_{r,2}}) & -(\frac{1}{h^2}+\frac{1}{2r_2h}) & 0 & \cdots & 0 \\ 0 & \cdots & \cdots & \cdots & \cdots & 0 \\ 0 & \cdots & \cdots & \cdots & \cdots & 0 \\ 0 & 0 & 0 & -(\frac{1}{h^2}-\frac{1}{2r_{N-1}h}) & (\frac{2}{h^2}+\frac{1}{r_{N-1}^2}\cdot\frac{E_{\theta,N-1}}{E_{r,N-1}}) & -(\frac{1}{h^2}+\frac{1}{2r_{N-1}h}) \\ 0 & 0 & 0 & \cdots & \frac{-2}{h^2} & (\frac{2}{h^2}+\frac{1}{r_N^2}\cdot\frac{E_{\theta,N}}{E_{r,N}}\cdot\frac{2h}{r_N}(\frac{1}{h^2}+\frac{1}{2r_Nh})) \end{bmatrix} \tag{3.39}$$

3.2.2.1Sample calculation

Utilizing the formulation by Pantazopoulou and Papoulia (2001), the maximum corrosion pressure and the strains induced in the cover concrete were calculated for a corroded rebar with the same properties as given in Section 3.2.1.1. The bursting pressure exerted on the cover concrete was calculated by discretizing the thickness of the cover to 10, 20, 50, 100, and 200 points as illustrated in Figure 3.10. Discretizing the cover thickness to more than 20 points didn't have a significant influence on the results. Thus, a mesh-centered grid with 20 points was used as the reference finite difference discretization. The pressure buildup resulting from rust accumulation around the rebar reached a maximum value of 16.32 MPa in 1.1 years which is in reasonable agreement with 14.73 MPa reached in 1.92 years calculated with the Wang and Liu (2004) model. However, the formulation of Wang and Liu (2004) overestimated the strength of the cover concrete in terms of the induced tensile strain and the radius up to which the cover concrete is cracked as depicted in Figure 3.11 and Figure 3.12. This was mainly due to the fact that the reduced stiffness of the cracked part of the cover concrete was not considered in the formulation of Wang and Liu (2004) and the same radial displacement pattern for the elastic and cracked cylinders was assumed.

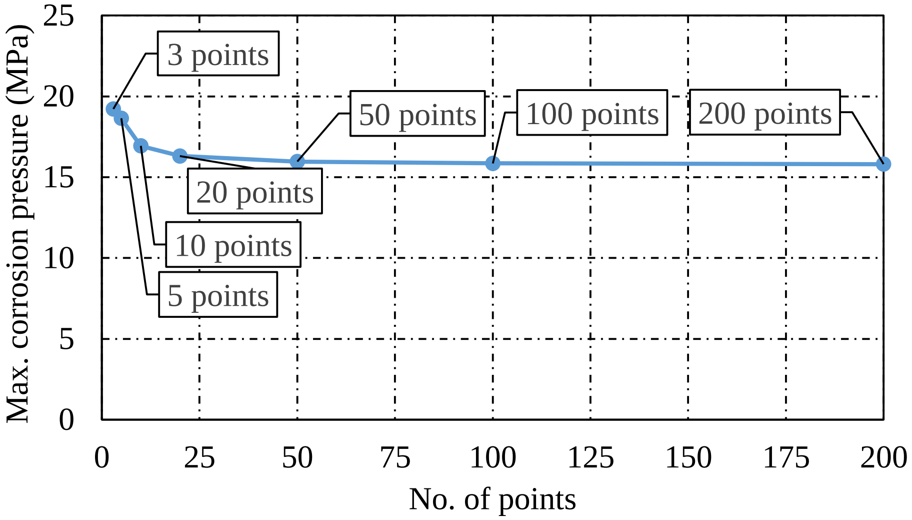

Figure 3.10: Internal pressure applied to the cover concrete by expansive rust products

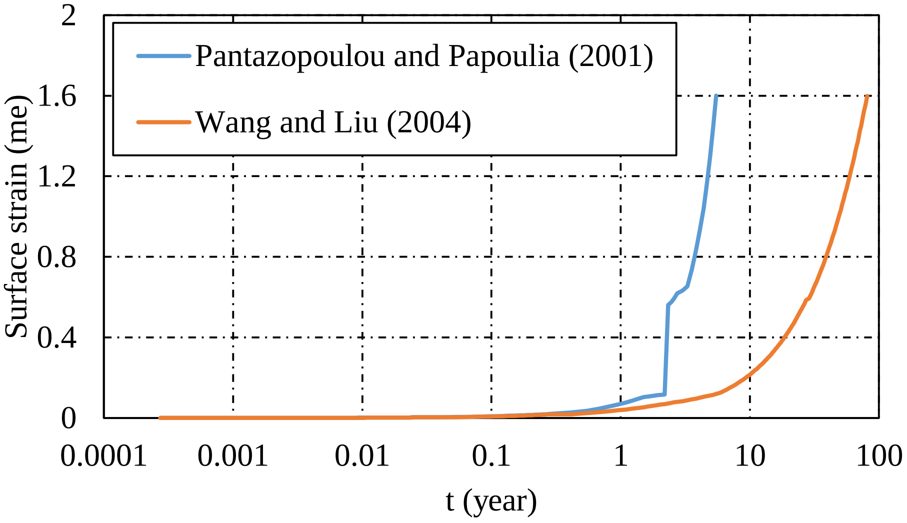

Figure 3.11: Hoop strain induced by expansive corrosion products at the surface of cover

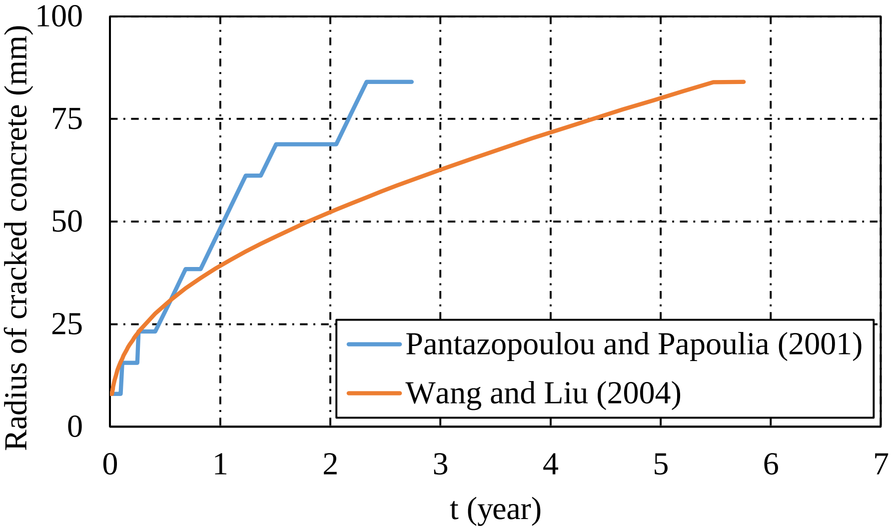

Figure 3.12: Radius of cracked concrete

3.2.3 VecTor Methodology

VecTor is a suite of nonlinear finite element analysis programs developed at the University of Toronto which can be used for the analysis of different types of structural members such as beams, plates and shells. This project was mainly focused on VecTor2 which can be used for analysis of two-dimensional reinforced concrete membrane structures. The formulation of VecTor2 is mainly based on the Distributed Stress Field Model (DSFM) which is an extension of the Modified Compression Field Theory (MCFT). The Compression Field Theory (CFT) developed by Collins and Mitchell in the 1970s is the basis of the MCFT and the DSFM. Although, the original CFT is still valid, it doesn't consider many second-order effects like compression softening or tension stiffening. These deficiencies were addressed in the MCFT (Vecchio, 1986). Subsequently, the DSFM (Vecchio, 2000) improved the shortcomings of the MCFT in predicting the response of lightly reinforced elements by decoupling the orientation of principal stresses and strains and distinguishing the deformations due to crack shear slip deformations and stress induced strains.

In general, VecTor2 treats reinforced concrete as an orthotropic material based on a total load, rotating smeared crack formulation. Three sets of equations, namely compatibility, equilibrium and constitutive relations, are used in an iterative algorithm to calculate the stress and strain state of a given element under a certain loading condition. Considering the reinforced concrete element shown in Figure 3.13, the total strains are made up of net (stress induced) concrete strains, elastic strain offsets, plastic strain offsets and crack shear slip strains, as such:

$$[\varepsilon] = [\varepsilon_c] + [\varepsilon_c^o] + \left[\varepsilon_c^p\right] + [\varepsilon_c^s] \tag{3.40}$$

Using compatibility equations, the strain in the i^{th} smeared reinforcement is the sum of the total strain, $[\varepsilon]$, elastic strain offsets, $[\varepsilon_s^o]_i$ and plastic strain offsets, $[\varepsilon_s^p]_i$, as follows:

$$[\varepsilon_s]_i = [\varepsilon] + [\varepsilon_s^o]_i + [\varepsilon_s^p]_i \tag{3.41}$$

In every iteration, the secant stiffness of the concrete is updated based on the assumed constitutive model for concrete in tension and compression. The stresses in the composite element, $[\sigma]$, are related to the total strains, $[\varepsilon]$, by the composite material stiffness matrix, $[D]$, which is comprised of concrete material stiffness matrix, $[D_c]$, and the reinforcement component material stiffness matrices, $[D_s]_i$, as shown in Eq. 3.42 and Eq. 3.43.

$$[\sigma] = [D][\varepsilon] - [\sigma^o] \tag{3.42}$$

$$[D] = [D_c] + \sum_{i=1}^{n} [D_s]_i \tag{3.43}$$

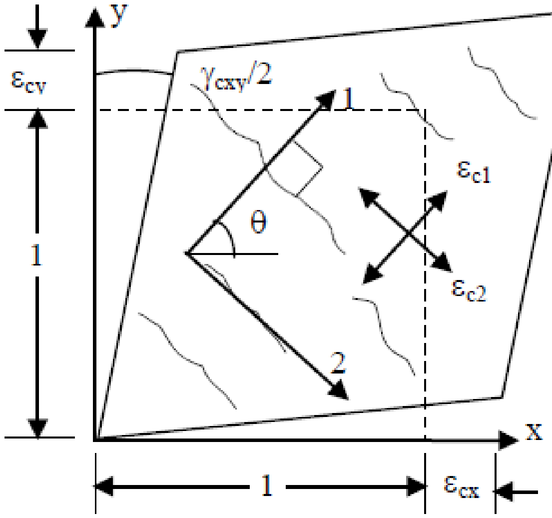

Figure 3.13: Reinforced concrete membrane element

Because the total strains in an element are not all due to the stress and the composite stiffness matrix operates on the total strains, the stress contribution of the strain offsets and the shear slip strain should be subtracted by the use of pseudo-stress vector, $[\sigma^o]$, which is defined as:

$$[\sigma^{o}] = [D_c]\{[\varepsilon_c^{o}] + [\varepsilon_c^{p}] + [\varepsilon^{s}]\} + \sum_{i=1}^{n}[D_s]_i\{\,[\varepsilon_s^{o}]_i + [\varepsilon_s^{p}]_i\} \tag{3.44}$$

The element stiffness matrix, $[k]$, is determined from the composite stiffness matrix, $[D]$, and the strain-displacement matrix, $[B]$, computed as:

$$[k] = \int [B]^{T}\,[D][B]dV \tag{3.45}$$

Combining Eq. 3.43 and Eq. 3.45, the element stiffness matrix can be separated into the contributions from the stiffness of the concrete, $[k_c]$, and the smeared reinforcements, $[k_s]_i$:

$$[k_c] = \int [B]^{T}\,[D_c][B]dV \tag{3.46}$$

$$[k_s]_i = \int [B]^{T}\,[D_s]_i[B]dV \tag{3.47}$$

Analogous to the pseudo-stress vector, equivalent nodal displacements due to strain offsets and crack shear slip strains should be accounted for as the element stiffness matrix operates on the total nodal displacements. The pseudo nodal loads, $[F^{*}]$, is determined by:

$$[F^{*}] = [k_c]\{[r_c^{o}] + [r_c^{p}] + [r_c^{s}]\} + \sum_{i=1}^{n}[k_s]_i\{[r_s^{o}] + [r_s^{p}]\} \tag{3.48}$$

where $[r_c^{o}]$, $[r_c^{p}]$, $[r_c^{s}]$ are free nodal displacements due to concrete offset strains and shear slip, and $[r_s^{o}]$ and $[r_s^{p}]$ are the displacements due to reinforcement strain offsets which are quantified by integration of their respective strain component:

$$[r_c^{o}] = \int [\varepsilon_c^{o}]dA \;;\; [r_c^{p}] = \int [\varepsilon_c^{p}]dA \;;\; [r_c^{s}] = \int [\varepsilon^{s}\,]dA \tag{3.49}$$

$$[r_s^{o}] = \int [\varepsilon_s^{o}]dA \;;\; [r_s^{p}] = \int [\varepsilon_s^{p}]dA \tag{3.50}$$

In order to incorporate the strains applied to the concrete due to expansion of the corrosion products, Eq. 3.48 was modified. The strains due to corrosion were evaluated from either of the two models presented in Section 3.2.1 and Section 3.2.2. The strain components in polar coordinates are as follows:

$$\varepsilon_r = \frac{\partial u_r}{\partial r}\ ;\ \varepsilon_\theta = \frac{u_r}{r} + \frac{\partial u_\theta}{r\partial\theta}\ ; \varepsilon_z = \frac{\partial u_z}{\partial z}$$

$$\gamma_{r\theta} = \frac{\partial u_r}{r\partial\theta} + \frac{\partial u_\theta}{\partial r} - \frac{u_\theta}{r}\ ;\ \gamma_{rz} = \frac{\partial u_r}{\partial z} + \frac{\partial u_z}{\partial r}\ ;\ \gamma_{z\theta} = \frac{\partial u_r}{\partial z} + \frac{\partial u_z}{r\partial\theta} \tag{3.51}$$

The deformation of a cylinder under uniform internal pressure is symmetrical with respect to z-axis resulting in the stress components being independent of the angle θ. Thus, all the derivatives with respect to θ are equal to zero. On account of symmetry, u_θ will also be equal to zero. Consequently, $\gamma_{r\theta}$ will be zero and the radial and tangential strains, ε_r and ε_θ, will be the principal strains. Assuming the deformations along the z-axis are equal to zero, the strain components will simplify to:

$$\varepsilon_r = \frac{\partial u_r}{\partial r}\ ;\ \varepsilon_\theta = \frac{u_r}{r} + \frac{\partial u_\theta}{r\partial\theta}\ ;\ \varepsilon_z = 0$$

$$\gamma_{r\theta} = 0\ ;\ \gamma_{rz} = \frac{\partial u_r}{\partial z}\ ;\ \gamma_{z\theta} = \frac{\partial u_r}{\partial z} \tag{3.52}$$

When uniform corrosion is modelled, radial displacement of the points located on an axis parallel to z-axis are equal to each other resulting in any derivation with respect to z-axis to be zero too. The only non-zero strain components, ε_r and ε_θ, which are the principal strains, are transformed from the principal axes to the reference system of VecTor2 as shown in Figure 3.14 using the following relationships:

$$\begin{Bmatrix} \varepsilon_z \\ \varepsilon_y \\ \varepsilon_{yz} \end{Bmatrix} = \begin{bmatrix} cos^2(\alpha) & sin^2(\alpha) & \sin(2\alpha) \\ sin^2(\alpha) & cos^2(\alpha) & -\sin(2\alpha) \\ -\frac{\sin(2\alpha)}{2} & \frac{\sin(2\alpha)}{2} & \cos(2\alpha) \end{bmatrix} \begin{Bmatrix} \varepsilon_1 \\ \varepsilon_2 \\ 0 \end{Bmatrix} \tag{3.53}$$

$$\alpha = \frac{\pi}{2} + \theta$$

Corrosion-induced nodal displacements are evaluated by integration of the strains in x, y directions due to corrosion, $[\varepsilon_c^{corr}]$, as follows:

$$[\varepsilon_c^{corr}] = \begin{Bmatrix} \varepsilon_x \\ \varepsilon_y \\ \gamma_{xy} \end{Bmatrix} = \begin{Bmatrix} 0 \\ sin^2(\alpha)\varepsilon_1 + cos^2(\alpha)\varepsilon_2 \\ 0 \end{Bmatrix} \tag{3.54}$$

$$[r_c^{corr}] = \int [\varepsilon_c^{corr}]dA \tag{3.55}$$

Eventually, the formulation of the pseudo nodal loads, $[F^*]$, in Eq. 3.48 is modified as below :

$$[F^*] = [k_c]\{[r_c^o] + [r_c^p] + [r_c^s] + [r_c^{corr}]\} + \sum_{i=1}^{n} [k_s]_i\{[r_s^o] + [r_s^p]\} \tag{3.56}$$

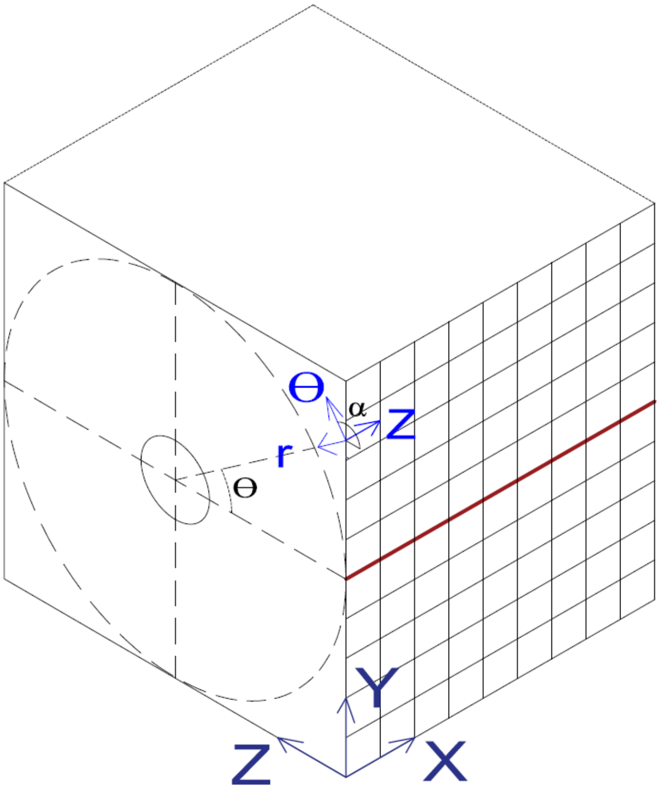

Figure 3.14: Strain transformation to VecTor2 reference axes

The flowcharts shown in Figure 3.15 and Figure 3.16 depict the implementation of the Wang and Liu (2004) and the Pantazopoulou and Papoulia (2001) formulations in VecTor2. The corrosion-induced strain matrix is calculated for the concrete elements in the vicinity of a corroding truss element before the iterations start. Then, in every subsequent iteration, strains due to corrosion are treated in the same way as strain offsets and are taken into account in the calculation of pseudo nodal loads.

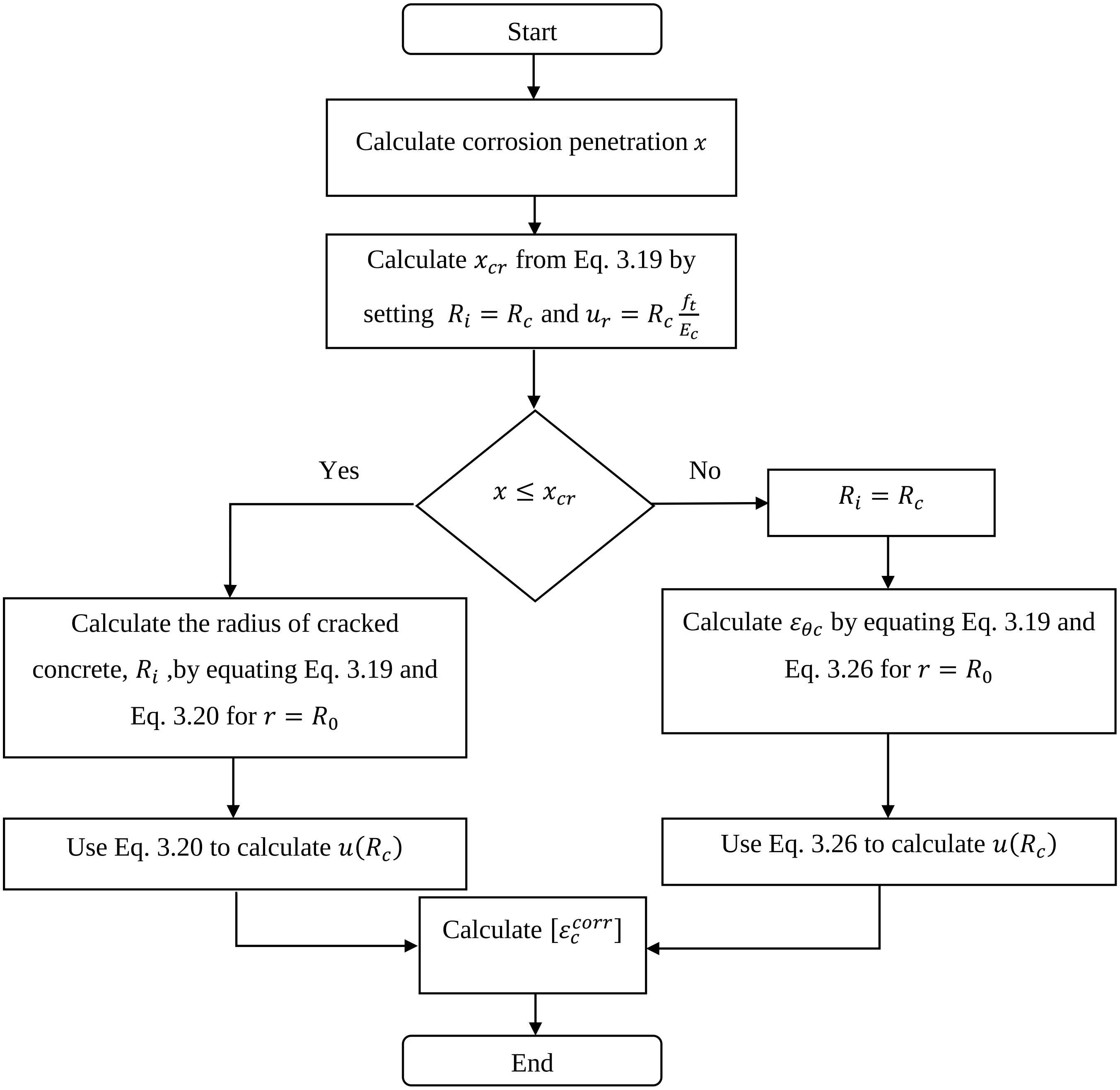

Figure 3.15: Implementation of the Wang and Liu (2004) model in VecTor2

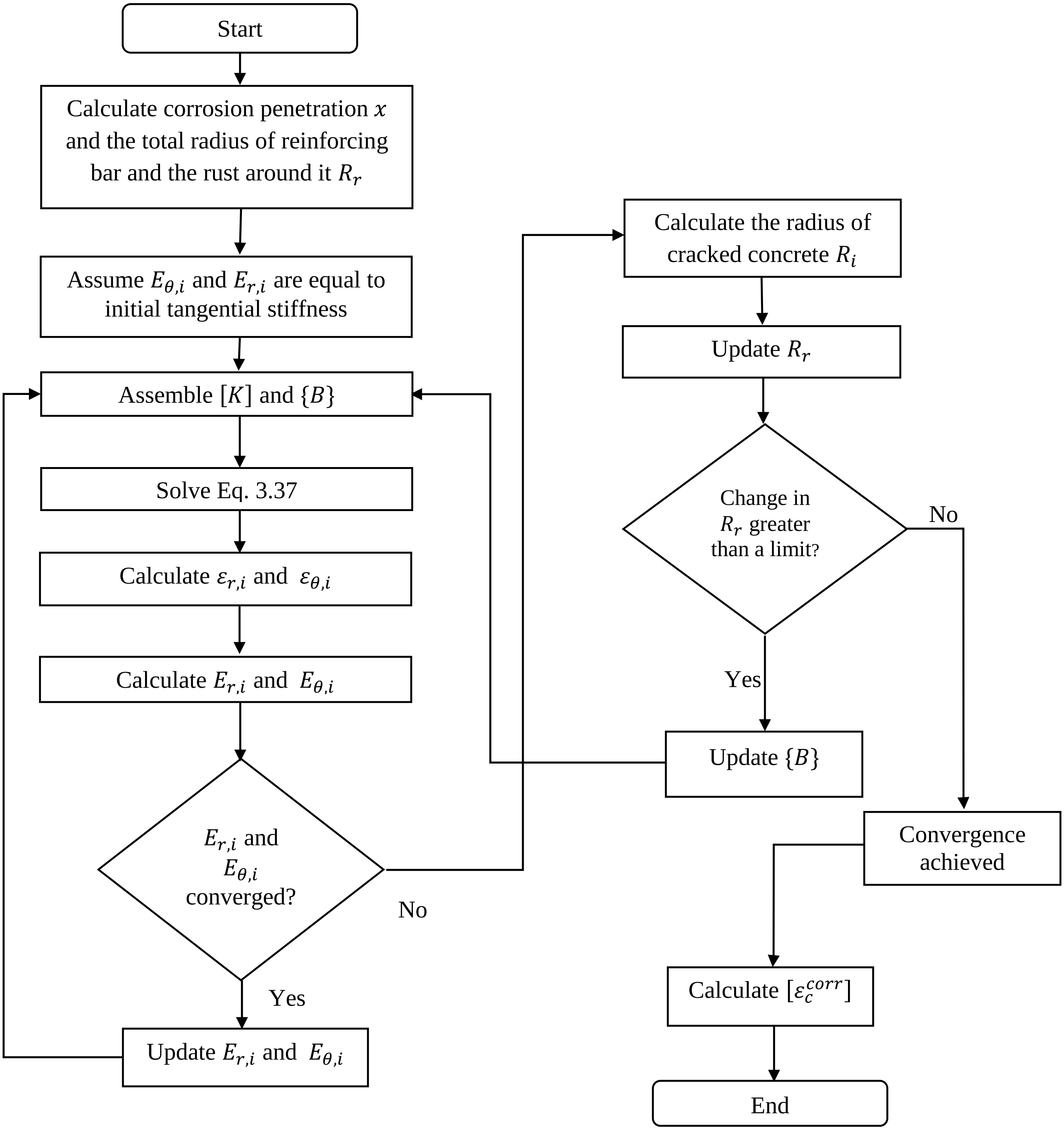

Figure 3.16: Implementation of the Pantazopoulou and Papoulia (2001) model in VecTor2

3.3 Bond Strength

The bond stresses between steel and concrete are transferred by adhesion, friction and bearing of the deformations of the rebar on the concrete. Adhesion and friction are severely reduced when the flaky corrosion products accumulate around a rebar. Moreover, cracking of the cover reduces the confining action of the concrete. As a result, the bond and anchorage between concrete and reinforcement of a corroding member will be severely degraded which directly effects the serviceability and ultimate strength. Pullout tests on corroded bars have shown that before cracking of the cover concrete, the bond strength slightly increases. This is attributed to an increase in the pressure applied to the concrete by corrosion products which adds to the confining action provided by the cover concrete. However, when the hoop tensile stress exceeds the tensile strength of the concrete, the reinforcement will be unconfined and the bond strength will drop rapidly. Therefore, quantifying the impaired bond between corroded reinforcement and concrete would help in evaluating the residual strength of corrosion damaged reinforced concrete structural members (Bhargava et al., 2007).

In VecTor2, the bond stress-slip of embedded bars is defined by calculating a series of reference points according to a user-selected bond model. The stress-slip relationship is defined for the two distinct cases of confined and unconfined bars. Based on the user-defined confinement pressure factor, β, the actual bond stress-slip curve is calculated by linear interpolation of confined and unconfined reference points. For more information, the reader is referred to “VecTor2 & FormWorks User’s Manual” (Wong et al., 2013).

Four empirical bond strength reduction models for corroded deformed bars have been chosen from the available literature and are implemented in VecTor2. All of the models specify an empirical reduction factor, referred to as bond strength reduction factor, for the bond strength of a corroded rebar. The damage is typically measured by the weight loss of the corroded rebar. The bond models of VecTor2 have been updated to include the bond strength reduction factor, R. Although analytical bond models for corroded reinforcing bars are also available in the literature, comparison of the bond strength given by these models showed that they don’t have any advantage over empirical models which are based on regression analysis and data fitting. The implemented models are explained and compared against experimental results in the following section.

3.3.1 Val et al. (1998)

The Val et al, (1998) proposed the bond strength reduction factor, R, as a function of the weight loss of reinforcement due to corrosion given in Eq. 3.57. The formulation is based on pullout tests on corroded bars with up to 8% weight loss. For higher values of corrosion, a residual bond strength equal to 10% of the initial bond strength is assumed.

$$R = \frac{\tau_{bu}}{\tau_{bu,o}} = \begin{cases} 1.0 & C(t) \le C_1 \\ (1 - (1 - \beta_T)\dfrac{C(t) - C_1}{C_2 - C_1}) & C_1 < C(t) \le C_2 \\ \beta_T & C(t) > C_2 \end{cases} \tag{3.57}$$

where:

- $C(t)$ = weight loss of the corroded reinforcing bar (%)
- $\tau_{bu,o}$ = original bond strength (MPa)
- τ_{bu} = reduced bond strength (MPa)
- C_1 = 1%
- C_2 = 8%
- β_T = 0.1

3.3.2 Chung et al. (2004)

Based on flexural tests on reinforced concrete slab specimens reinforced with corroded bars, Chung et al. (2004) suggested Eq. 3.58. The formulation is shown graphically in Figure 3.17. Two percent weight loss was identified as the critical corrosion level at which the ribs of a deformed bar will no longer exist.

$$R = \begin{cases} 1 & C(t) \le 2\% \\ 2.09C(t)^{-1.06} & C(t) > 2\% \end{cases} \tag{3.58}$$

3.3.3 Feng et al. (2016)

The Feng et al. (2016) model is derived from numerical analysis of a large database of 377 data points. The evolution of bond strength reduction factor with corrosion is divided into three stages. The first stage models the confining effect of corrosion before cracking of the cover concrete and the third stage represents the residual bond strength of corroded bars with more than 10% weight loss. In between, a linear reduction is suggested. The formulation is distinct from the previous models in the sense that it considers the increase in bond strength for small levels of corrosion.

$$R = \begin{cases} \left(-0.0320\dfrac{C}{d_b} + 0.576\right)C(t) + 1 & C(t) \leq C_{pk} \\ \left(0.0137\dfrac{C}{d_b} - 0.247\right)C(t) + 1.42 + 0.0475\dfrac{C}{d_b} & C_{pk} < C(t) \leq C_{2-3} \\ -0.0016C(t) + 0.224 & C(t) > C_{2-3} \end{cases} \tag{3.59}$$

where:

- $C_{pk} = 0.0864\frac{C}{d_b} + 0.516$
- $C_{2-3} = \frac{-1.20-0.0475(C/d_b)+0.003094(C/d_b)^2}{0.0137(C/d_b)-0.245}$
- C = concrete cover (mm)

3.3.4 Maaddawy et al. (2005)

Based on the bond strength model proposed by Kemp and William (1979) for non-corroded bars and the experimental work of Saifullah and Clarck (1994), Maaddawy et al. (2005) proposed a bond strength reduction factor given in Eq. 3.60 where A_1 and A_2 are empirical coefficients given in Table 3.8.

$$R = A_1 + A_2C(t) \tag{3.60}$$

Table 3.8: Empirical coefficients of Maaddawy et al. (2005) bond strength reduction model

i_{corr} (μA/cm^2)	A_1	A_2
40	1.003	-0.037
90	1.104	-0.024
150	1.152	-0.021
250	1.163	-0.011
500	0.953	-0.014
1000	0.861	-0.014
2000	0.677	-0.009
4000	0.551	-0.010

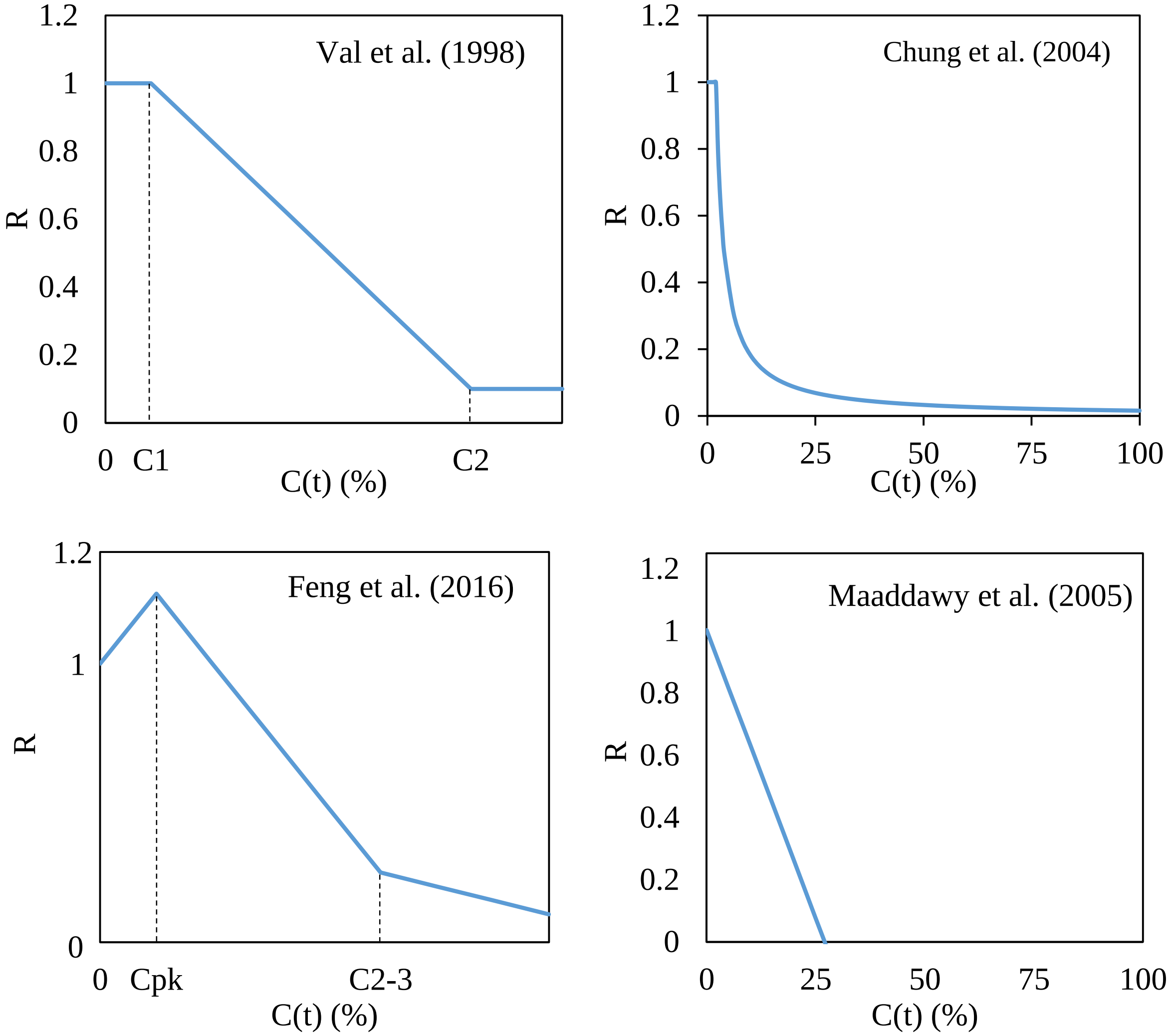

Figure 3.17: Bond strength reduction models

3.3.5 Verification of Implementation

The implemented bond models were checked against pullout tests performed by Al-Sulaimani et al. (1990). The results are depicted in Figure 3.18. Although the Fang et al. (2004) model considers the initial increase in the bond strength of a corroded bar and seems to be more accurate than the other models, due to the great variability associated with bond strength, the more conservative and less precise models provided by Val et al. (1998) and Chung et al. (2004) are suggested to be used.

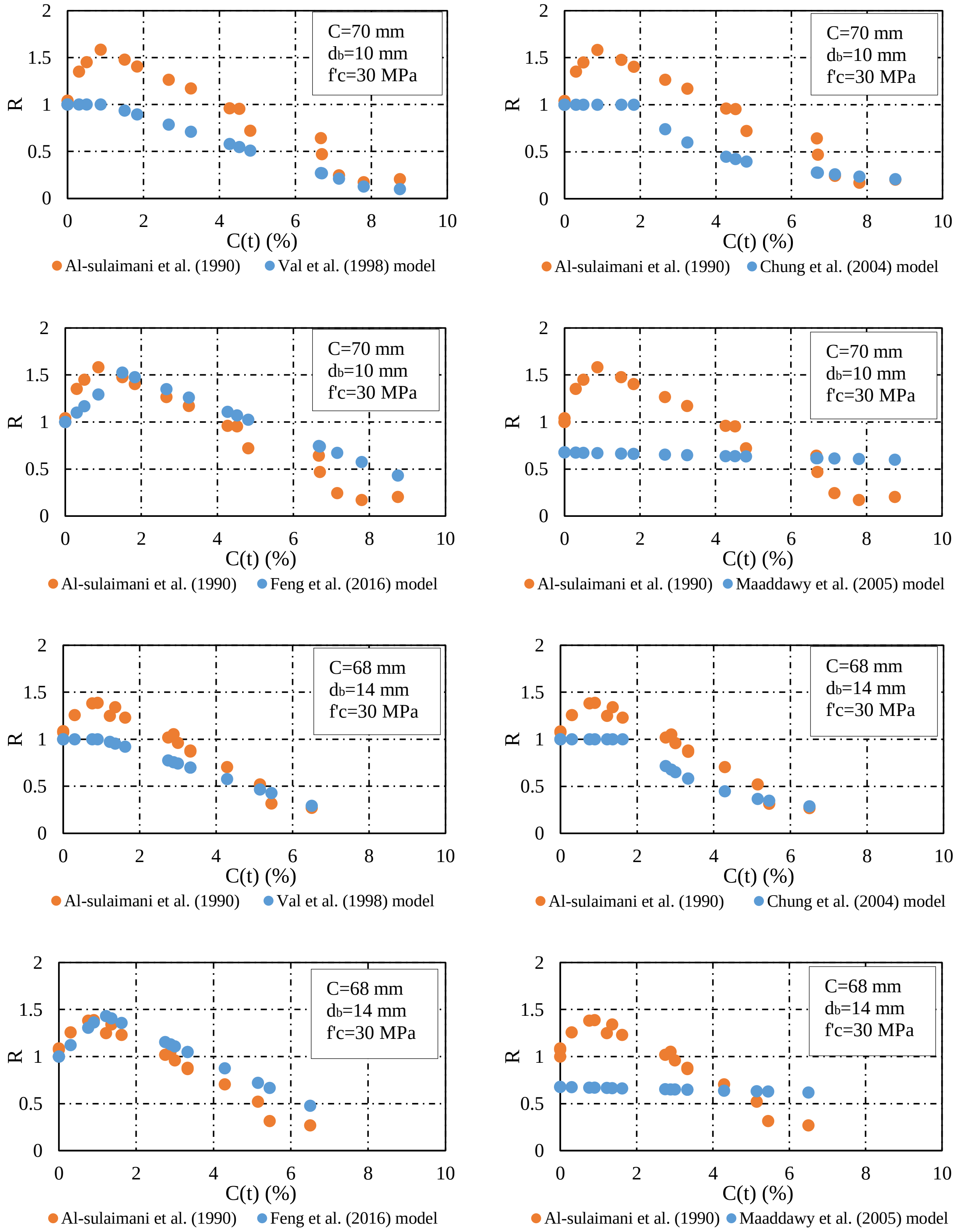

Figure 3.18: Bond strength reduction factor (R) versus level of corrosion for pullout specimens with 10 and 14 mm bars

3.4 Mechanical properties of corrosion-damaged reinforcement

Reinforcing bars subjected to local or pitting corrosion may suffer a loss of strength or ductility. The consequences of uniform corrosion were addressed by using the residual cross-sectional area of the corroded bar, reducing the bond strength, and straining the concrete elements around the reinforcing bar. However, the nature of pitting attack is substantially different from uniform corrosion. The oxidation products of pitting corrosion are less expansive to the extent that no signs of longitudinal cracking might become visible prior to significant section loss (Cairns et al., 2005).

In order to investigate the effects of corrosion on mechanical properties of reinforcement, Cairns et al. (2005) conducted a series of tests on deteriorated reinforcing bars. In the first group of tests, corrosion damage was simulated by removing a section of bar, using a multi-fluted hemispherical end mill with a cylindrical shank. Tensile tests were carried out on the artificially defected reinforcement. Significant reduction in the ductility of the bars was reported. In accordance with the first group of tests, two other series of tests were conducted on ribbed and plain bars placed in concrete specimens and damaged by accelerated corrosion. A mixture of general and pitting corrosion of varying intensities were observed.

In VecTor2, the mechanical properties of a corroded truss element subjected to pitting corrosion were updated using the following:

$$f_y = (1 - \alpha_y \cdot Q_{corr}) f_{y0} \tag{3.61}$$

$$f_u = (1 - \alpha_u \cdot Q_{corr}) f_{u0} \tag{3.62}$$

$$\varepsilon_u = (1 - \alpha_1 \cdot Q_{corr}) \varepsilon_{u0} \tag{3.63}$$

where:

- $f_{y0}, f_{u0}, \varepsilon_{u0}$ = yield strength, ultimate strength, ultimate strain of a non-corroded bar
- f_y, f_u, ε_u = yield strength, ultimate strength, ultimate strain of a corroded bar
- Q_{corr} = cross section loss expressed as a percentage of original cross section
- $\alpha_y, \alpha_u, \alpha_1$ = empirical coefficients

Cairns et al. (2005) suggested that a value of 0.01 for α_y and α_u represents a uniform corrosion attack while values greater than 0.01 represent local or pitting corrosion. A noticeable scatter can be observed in the reported values of empirical coefficients presented in Table 3.9. Nonetheless, the coefficients suggested by Du (2001) were incorporated in VecTor2.

Table 3.9: Empirical coefficients for reduction of strength and ductility of corroded reinforcing bars. Extracted from Cairns et al. (2005)

Author	Exposure	Q_{corr} (%)	α_y	α_u	α_1
Du (2001)	Accelerated, 1 mA/cm^2	0 to 18	0.015	0.015	0.039
Morinaga (1996)	Service, chlorides	0 to 25	0.017	0.018	0.060
Zhang et al. (1995)	Service, carbonation	0 to 67	0.010	0.010	0.000
Cairns et al. (2005)	Accelerated, 0.01 to 0.05 mA/cm^2	0 to 3	0.012	0.011	0.030

4 Deterministic Modelling of Corroded Reinforced Concrete Beams

In this chapter, the finite element modelling of reinforced concrete beams with corroded reinforcement, utilizing the program VecTor2, is discussed. The accuracy of the corrosion-damage models implemented in VecTor2 and the analytical procedure employed were checked by modelling a number of beams with corroded reinforcement chosen from the literature. Two types of deterministic (Chapter 4) and stochastic (Chapter 5) simulations were performed. The spatial variability of cross-sectional loss due to corrosion was not considered in the deterministic analyses, whereas in the stochastic simulations such variability was incorporated in the FE models by utilizing Monte Carlo sampling.

The default behavioural models of VecTor2 for concrete and reinforcing steel, shown in Table 4.1, were used. For each beam, the cylinder compressive strength, tensile strength, and initial tangent modulus of the concrete as well as the yield strength, ultimate strength, and modulus of elasticity of the reinforcing steel were manually specified according to the values reported by the researchers. In cases where one of these material properties was not reported, a reasonable assumption, mentioned in the corresponding section, has been made. VecTor2 default values were used for other material properties deemed not critical for the finite element models.

Table 4.1: VecTor2 default constitutive models

Concrete Constitutive Models			
Compression Pre-Peak	Hognestad (Parabola)	Dilation	Variable - Kupfer
Compression Post-Peak	Modified Park-Kent	Cracking Criterion	Mohr-Coulomb (Stress)
Compression Softening	Vecchio 1992-A	Crack Stress Calculation	Basic (DSFM/MCFT)
Tension Stiffening	Modified Bentz 2003	Crack Width Check	Agg/2.5 Max Crack Width
Tension Softening	Bilinear	Crack Slip Calculation	Walraven
FRC Tension	SDEM – Monotonic	Hysteretic Response	Nonlinear w/ Plastic offsets
Confined Strength	Kupfer/Richart		
Reinforcement Constitutive Models			
Hysteretic Response	Bauschinger Effect (Seckin)	Buckling	Akkaya 2012
Dowel Action	Tassios (Crack Slip)	Concrete Bond	Eligehausen

4.1 Azad et al. (2007)

Azad et al. (2007) tested 28 reinforced concrete beams to investigate the effects of varying degrees of reinforcing steel corrosion on the flexural behaviour of reinforced concrete beams. The design variables of the tests were the bar diameter, clear cover to the tension reinforcement, corrosion current density, and duration of the tests. The properties of the concrete and reinforcing steel used in the beams are given in Table 4.2. The beams were 1100 mm long and had a square cross section with a side length of 150 mm. To prevent premature shear failure, double-legged 6 mm diameter stirrups spaced 90 mm apart were provided for each beam. Two 8 mm diameter deformed bars with 36 mm clear cover were placed at the top of the beams as compression reinforcement. The tension reinforcement consisted of two 10 mm or 12 mm diameter bars as stated in Table 4.3. The geometry of the test specimens is depicted in Figure 4.1. The beams were cast using 10 batches of concrete with 350 kg/m^3 Type I Portland cement, with a water-cement ratio of 0.45 and a coarse to fine aggregate ratio of 1.65.

Table 4.2: Properties of the concrete and reinforcing steel used in Azad et al. (2007) tests

Beam series	Concrete	10 mm rebar		12 mm rebar	
	f_c' (MPa)	f_y (MPa)	f_u (MPa)	f_y (MPa)	f_u (MPa)
BT1	45.8	520	551	590	700
BT2	36.3	520	551	590	700
BT3	46.5	520	551	590	700
BT4	46.1	520	551	590	700

Corrosion of the reinforcement was facilitated by the addition of 2% sodium chloride by weight of cement to the mixture. After seven days of moist curing followed by air curing at room temperature, the tension bars of each beam were subjected to accelerated corrosion by connecting an anodic current to the tension bars. The beams were immersed in a 5% sodium chloride solution during this period.

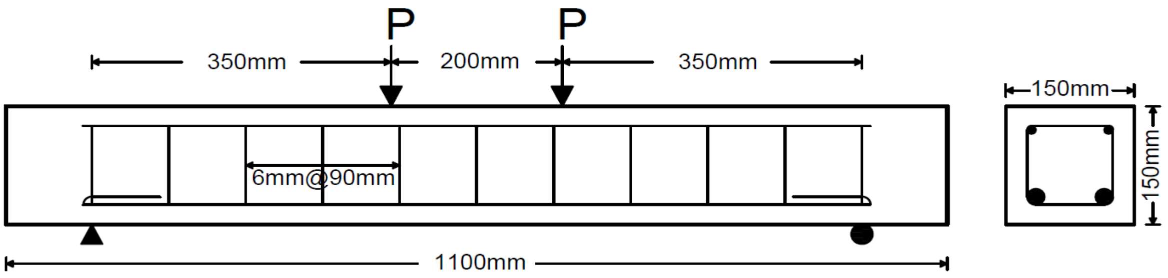

Figure 4.1: Geometry of Azad et al. (2007) test specimens

Table 4.3: Details of Azad et al. (2007) test specimens

Beam	D (mm)	Cover (mm)	Corrosion current density (mA/cm^2) Applied	Achieved	t (days)	Weight loss (%)
BT1-2-4	10	25	2.00	1.03	4	5.4
BT1-3-4	10	25	3.00	2.72	4	14.2
BT1-2-6	10	25	2.00	1.97	6	15.2
BT1-3-6	10	25	3.00	2.74	6	21.4
BT1-2-8	10	25	2.00	2.18	8	21.5
BT1-3-8	10	25	3.00	2.99	8	31.0
BT2-2-4	12	25	2.00	1.25	4	5.5
BT2-3-4	12	25	3.00	1.96	4	8.8
BT2-2-6	12	25	2.00	2.99	6	20.1
BT2-3-6	12	25	3.00	2.09	6	14.0
BT2-2-8	12	25	2.00	2.58	8	22.9
BT2-3-8	12	25	3.00	2.62	8	25.5
BT3-2-4	10	40	2.00	1.52	4	8.0
BT3-3-4	10	40	3.00	1.73	4	9.1
BT3-2-6	10	40	2.00	1.28	6	10.1
BT3-3-6	10	40	3.00	2.21	6	17.6
BT3-2-8	10	40	2.00	2.02	8	21.4
BT3-3-8	10	40	3.00	3.13	8	34.8
BT4-2-4	12	40	2.00	1.74	4	7.9
BT4-3-4	12	40	3.00	2.49	4	10.9
BT4-2-6	12	40	2.00	2.03	6	13.4
BT4-3-6	12	40	3.00	2.80	6	18.6
BT4-2-8	12	40	2.00	2.08	8	18.0
BT4-3-8	12	40	3.00	2.37	8	20.7
BT1-C	10	25	Control specimen			
BT2-C	12	25	Control specimen			
BT3-C	10	40	Control specimen			
BT4-C	12	40	Control specimen			

The beams were tested under symmetrical two-point loading with a universal testing machine. The specimens were disassembled after flexural testing and the corroded bars were cleaned from the adhered corrosion products using Clarke's solution according to ASTM G1. The weight loss due to the corrosion of the bars was measured by the gravimetric method. In order to examine the efficiency of the employed accelerated corrosion technique, that is the application of an anodic current to the reinforcement, Azad et al. (2007) utilized Faraday's law formulation, given in Eq. 3.2, to calculate the corrosion current density that was achieved during the tests from the measured weight loss of the bars. This value has been reported for each one of the corroded beams in Table 4.3. The calculated current densities were generally lower than the applied ones. This discrepancy was attributed to the spatial irregularities in the quality of the cover concrete, resulting in a non-uniform corrosion rate along the length of the bars. More specifically, Azad et al. (2007) calculated the applied current density based on the assumption of steel depassivation and corrosion over the whole length of the corroded bar while they occurred in a non-uniform manner. Based on the same observation, Austin et al. (2004) proposed a modified version of Faraday's law which gives a more reliable estimate of reinforcing steel cross-sectional loss by formulating the rate of corrosion as follows:

$$Corrosion\ rate = \frac{dr_b}{dt} = \frac{i_{corr}}{nF}\left(\frac{a_c}{A_c}\right) \tag{4.1}$$

where:

- a_c = area of depassivated steel (mm^2)
- A_c = total surface area of reinforcing bar (mm^2)
- i_{corr} = corrosion current density ($\frac{\mathrm{A}}{\mathrm{m}^2}$)
- F = Faraday constant (96494 $\frac{\mathrm{C}}{\mathrm{mol.e^-}}$ or $\frac{\mathrm{A.s}}{\mathrm{mol.e^-}}$)
- n = electrons per mole of iron (constant)
- r_b = radius of reinforcing bar (mm)

In addition, the variable t in Eq. 3.2 or Eq. 4.1, rather being based on the total time during which the anodic current is applied, should be based on the duration of the corrosion activity from the beginning of steel depassivation. Compared to the average cross-sectional loss, local loss was severely higher at some locations, mainly due to simultaneous occurrence of pitting and uniform corrosion.

Finite element models of the beams were created utilizing FormWorks, the pre-processor program for VecTor2. Except for the material properties summarized in Table 4.2, other input parameters were left as the default VecTor2 values. The reinforcement layout together with the mesh and support conditions are shown in Figure 4.2. Meshing was done by choosing an element size of 10 mm × 10 mm for every region. Any smaller size would have surpassed the maximum allowable number of the nodes in VecTor2. The stirrups in the out-of-plane direction were modelled as smeared reinforcement. In-plane tension, compression, and transverse reinforcement were modelled by 311 discrete truss elements. The bond between the concrete and corroded truss elements was modelled by placing link elements over the length of the tension reinforcement.

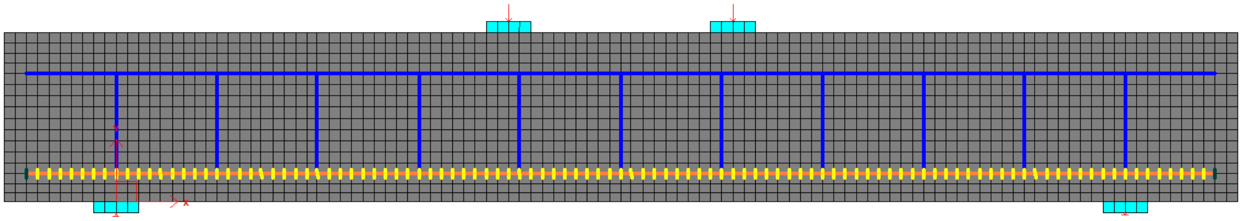

Figure 4.2: Finite element model of Azad et al. (2007) beams

The loss of cross-sectional area of the reinforcing steel was calculated based on the applied corrosion current density utilizing Eq. 3.3. The motive for using the applied corrosion current density instead of the achieved one was to avoid subjectivity of the analysis and to clearly demonstrate the capabilities and inaccuracies of the FE model. The Feng et al. (2016) and Pantazopoulou and Papoulia (2004) models were used for calculation of the bond strength reduction factor and cracking of the cover concrete, respectively. Employing the method explained in Section 3.2.3, cracks that formed in the cover concrete due to corrosion were incorporated into the FE models. Cracking of the cover concrete, as observed in Augustus, the post-processor program of VecTor2, is depicted in Figure 4.3. The longitudinal cracks above the corroded reinforcement were significantly smaller in width compared to the cracks formed in the plain concrete below the reinforcement, due to the confinement provided by the stirrups. Thus, the employed method seems to reasonably capture the pattern of the corrosion cracks. The increase in volume of the corroded bars generated tensile stresses up to 163 MPa in the stirrups.

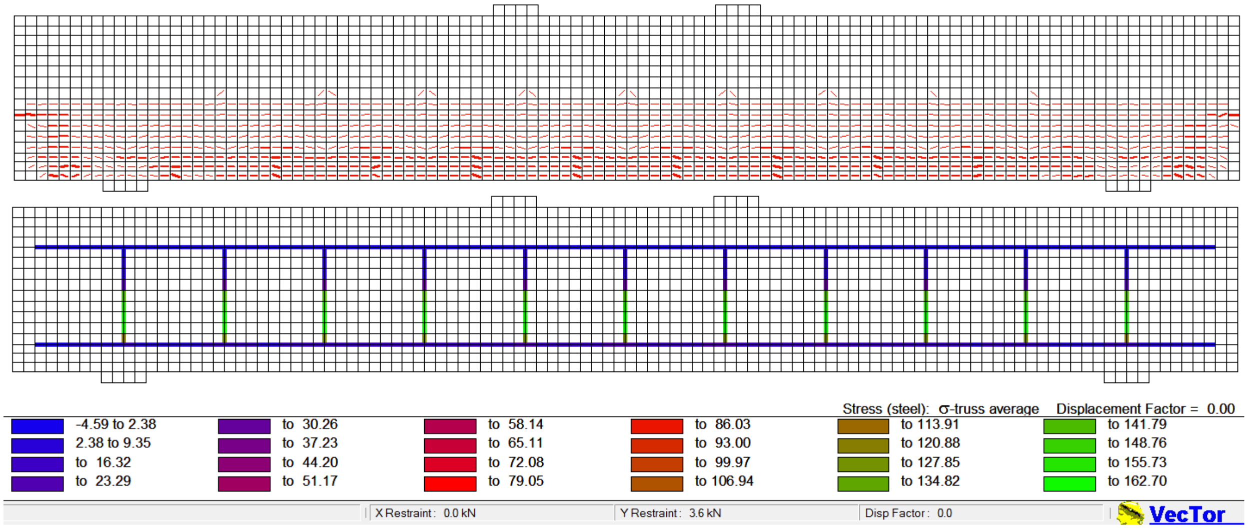

Figure 4.3: Corrosion induced cracking of cover concrete modelled in VecTor2

A monotonic nodal displacement with increments of 1 mm was applied to the finite element models at the locations shown in Figure 4.1. The experimental load-displacement curves were only provided by the authors for six out of the 24 corroded beams. Load-deflection responses predicted by VecTor2 along with the experimental ones are shown in Figure 4.4.

The ultimate strength of the beams with corroded reinforcement was accurately captured by VecTor2. The ratios of the calculated to experimental ultimate capacities, summarized in Table 4.4, had a mean of 1.05 and a C.O.V of 17.42%. Initially, this ratio was less than 1.0 (strength underestimated) but increased to values greater than 1.0 as corrosion progressed (strength overestimated). A slightly overestimated initial stiffness was observed for every beam which might be due to an overestimated concrete initial tangent modulus calculated by the default formulation of VecTor2 (i.e. $3320\sqrt{f'_c} + 6900$). A clear explanation for the differences between the mid-span deflections at ultimate load observed in the experiments and those predicted by VecTor2 was not found. Regarding the failure modes, a flexure-shear type of failure was observed in all beams as per Azad et al. (2007). Flexural failure with concrete crushing at the top was predicted by VecTor2 which was in agreement with the experiments. The failure of the beams was accompanied with significant slip between the tension reinforcement and concrete. As a result, the response of the beams was very sensitive to the choice of the bond strength reduction model. Beam BT1-2-4 was modelled four times with each of the implemented bond strength reduction models as depicted in Figure 4.5.

Table 4.4: Experimental versus calculated ultimate loads of Azad et al. (2007) beams

Beam	$P_{u,test}$ (kN)	$P_{u,VecTor2}$ (kN)	Calc./ Exp.	Beam	$P_{u,test}$ (kN)	$P_{u,VecTor2}$ (kN)	Calc./ Exp.
BT1-C	66.51	63.16	0.95	BT3-C	67.20	55.94	0.83
BT1-2-4	61.02	58.30	0.96	BT3-2-4	62.40	51.60	0.83
BT1-3-4	58.00	54.22	0.93	BT3-3-4	58.23	49.36	0.85
BT1-2-6	59.77	54.22	0.91	BT3-2-6	56.46	49.36	0.87
BT1-3-6	52.29	51.03	0.98	BT3-3-6	53.03	46.54	0.88
BT1-2-8	44.69	50.93	1.14	BT3-2-8	52.11	47.40	0.91
BT1-3-8	37.03	46.12	1.25	BT3-3-8	37.71	43.33	1.15
BT2-C	84.57	86.90	1.03	BT4-C	75.03	83.88	1.12
BT2-2-4	72.91	64.52	0.88	BT4-2-4	68.74	73.07	1.06
BT2-3-4	68.40	64.26	0.94	BT4-3-4	62.46	70.19	1.12
BT2-2-6	59.60	61.80	1.04	BT4-2-6	57.26	70.19	1.23
BT2-3-6	60.29	59.56	0.99	BT4-3-6	51.31	67.70	1.32
BT2-2-8	50.74	59.67	1.18	BT4-2-8	51.43	69.79	1.36
BT2-3-8	48.51	59.90	1.03	BT4-3-8	43.26	64.03	1.48
						mean	1.05
						C.O.V	17.4%

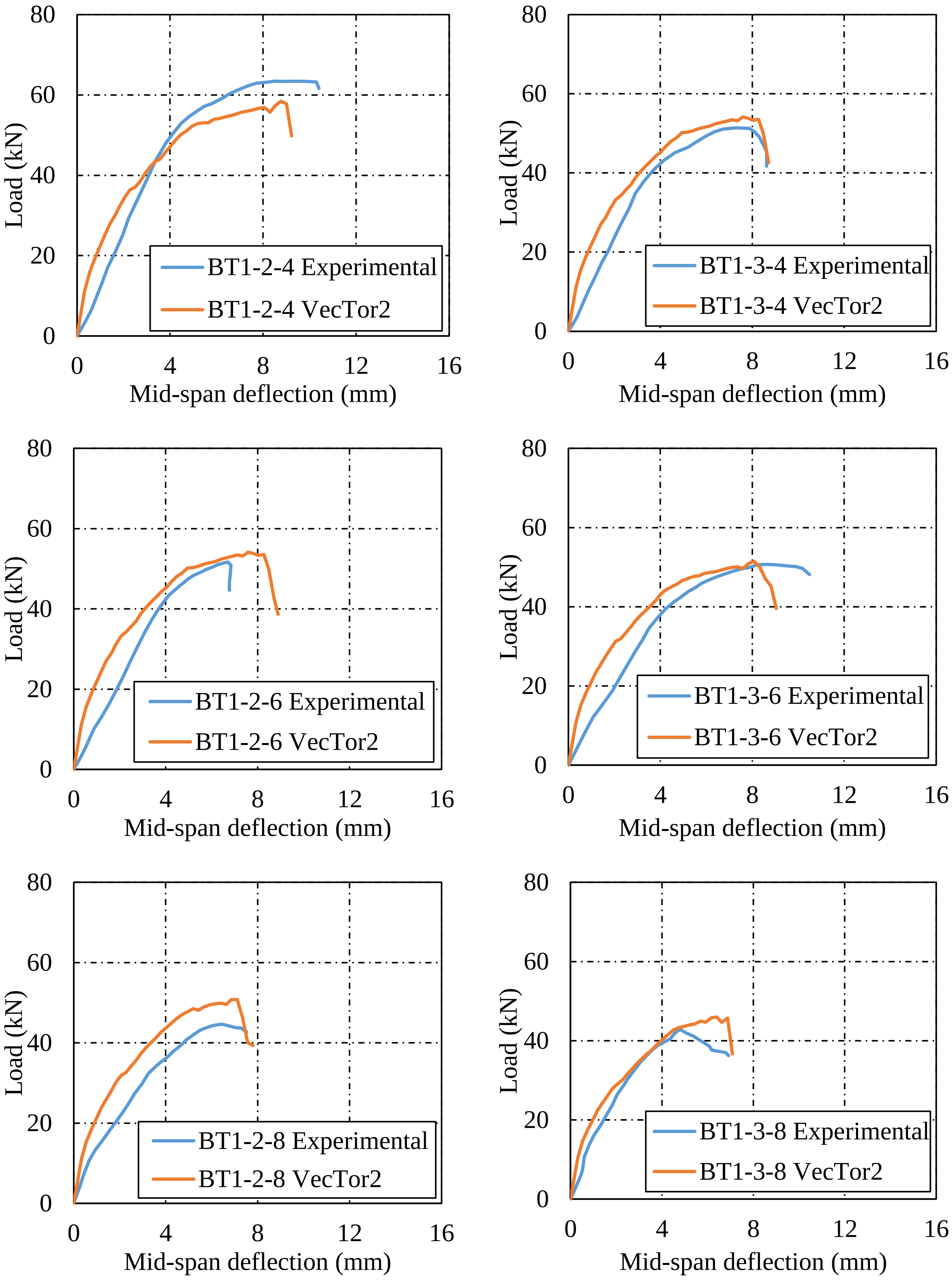

Figure 4.4: Load-deflection response of corroded beams of Azad et al. (2007)

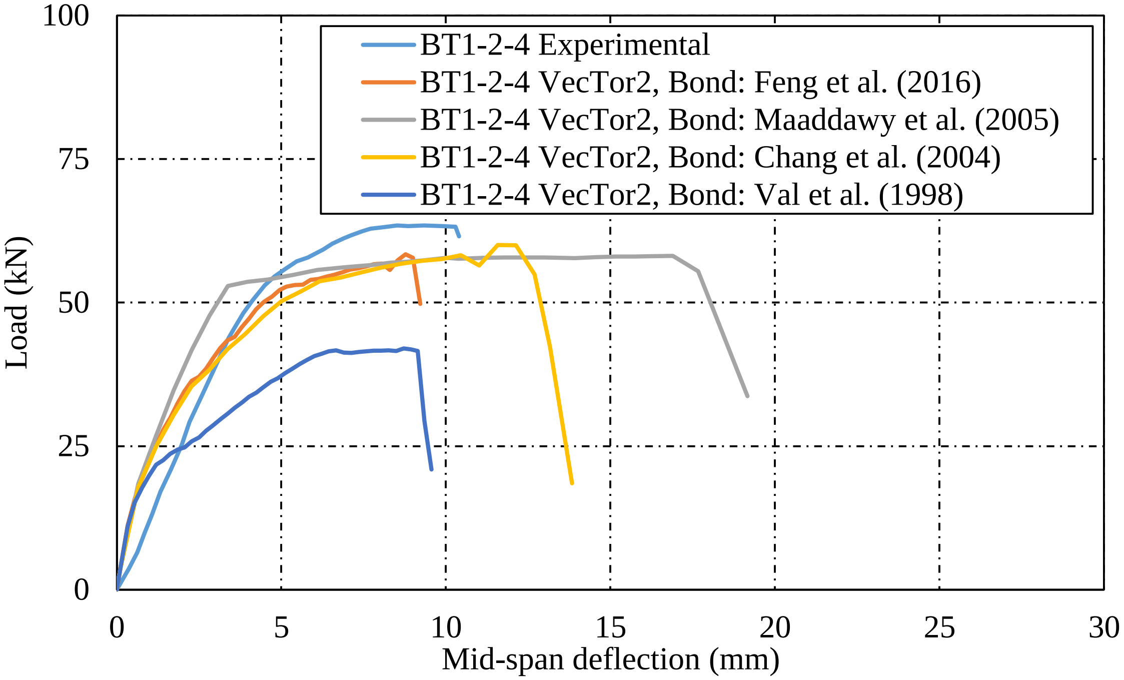

Figure 4.5: Load-deflection response of Azad et al. (2007) BT1-2-4 beam

The Maaddawy et al. (2005) bond strength reduction model predicted the smallest reduction in the bond strength by providing 46% reduction. Tensile stresses higher than the yield stress of the tension reinforcement were developed over a significant length of the beam. As a result, the FE model had a ductile response with a clear yield plateau. The Chang et al. (2004) and Feng et al. (2016) models predicted 79% and 82% reduction in the bond strength, respectively. The Val et al. (1998) model predicted 90% bond strength reduction, resulting in bond breakdown at an early stage of the loading. In conclusion, debonding of the reinforcement was found to be crucial to the response of the beams with corroded reinforcement failing in flexure. In the case of the Azad et al. (2007) beams, the FE models with Feng et al. (2016) and Chung et al. (2004) bond strength reduction models traced the experimental results more precisely. However, the disparate values of bond strength reduction factors clearly demonstrate the need for further research to better understand the degree to which the bond between the reinforcement and concrete degrades due to corrosion.

Figure 4.6 depicts the load-deflection curve of the BT1-2-4 beam, modelled using the Val et al. (1998) bond strength reduction model and both of the cover cracking models implemented in VecTor2. The Wang and Liu (2004) model predicted a much smaller tensile strain induced in the cover concrete compared to the value given by the Pantazopoulou and Papoulia (2001) model. However, the inaccuracy introduced in the response of the FE model by the bond strength reduction model was the predominant factor. The source of this observation, expected to be seen in every FE modelling attempt, is the fact that the concrete elements severely affected by corrosion are the ones located below the tension reinforcement. These elements are subjected to the highest tensile strains in the beam. Whether corrosion had occurred or not, they would have experienced severe cracking close to failure of the beam. Thus, except for a serviceability limit state, cracking of the cover concrete should not be of great concern.

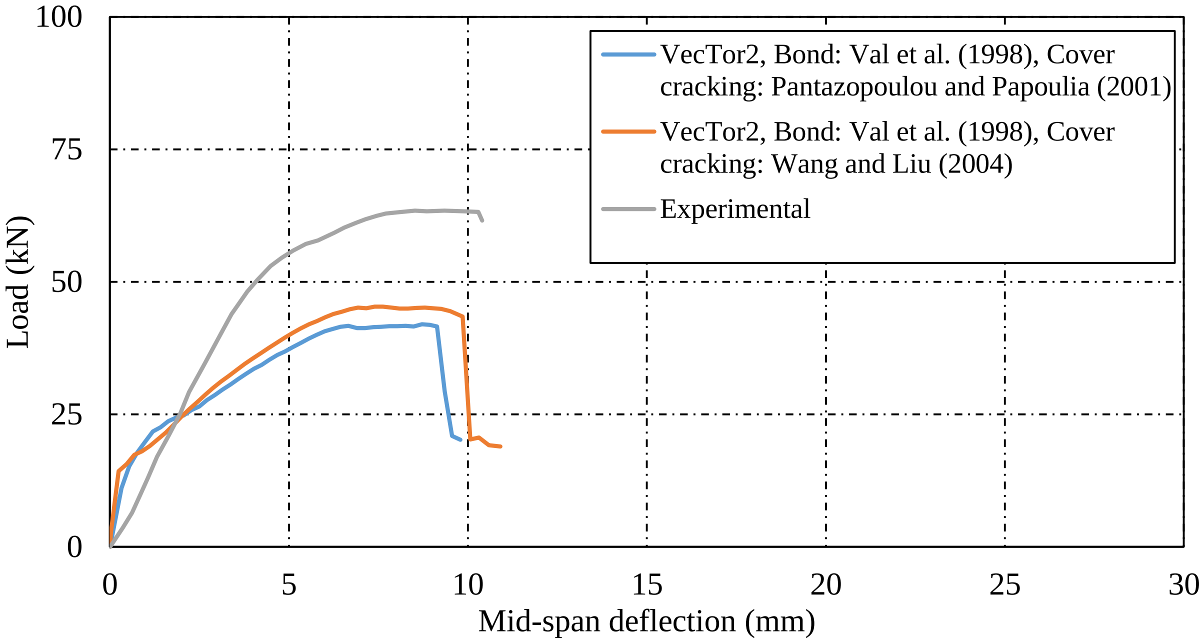

Figure 4.6: Effect of cover cracking model on the flexural response

4.2 Maaddawy et al. (2005)

Maaddawy et al. (2005) studied the effect of sustained loading and simultaneous corrosion on the flexural behaviour of reinforced concrete beams by testing nine reinforced concrete beams. The beams were identical in size, each measuring 152 mm × 254 mm × 3200 mm, and had the same material properties. The only design variable was corrosion time. Two No. 15 grade 60 bars and two 8 mm diameter smooth bars were used as the tension and compression reinforcement, respectively. Stirrups were double-legged 8 mm diameter smooth bars spaced at 80 mm apart in the shear span and 333 mm in the constant moment region. The mechanical properties of the reinforcement are given in Table 4.5.

Table 4.5: Mechanical properties of reinforcing bars used in Maaddawy et al. (2005) beams

	Bar type	D (mm)	f_y (MPa)	f_u (MPa)
Tensile reinforcement	Deformed	16	450	585
Compression reinforcement	Smooth	8	340	500
Stirrups	Smooth	8	340	500

The concrete was made from Portland cement with a 0.55 water-cement ratio. In each beam, 2.25% chloride by weight of cement was added to the concrete in the middle 1400 mm length to a 100 mm height as shown in Figure 4.7. Thus, only the portion of the tension reinforcement that was located in the salted zone was expected to corrode. The remaining length of the tension bars and the whole length of the compression and transverse reinforcement were protected against corrosion by an epoxy coating. The average cylinder compressive strengths of the salted and unsalted concrete were 40 and 41 MPa, respectively.

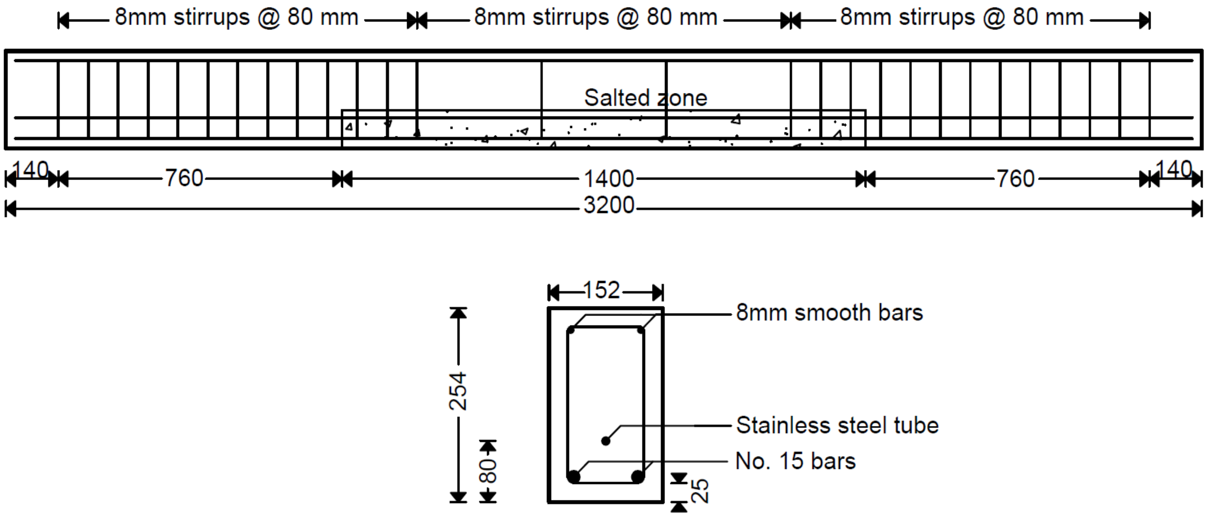

Figure 4.7: Details of Maaddawy et al. (2005) beams

Direct electrical current with an intensity of 215 mA, equivalent to a current density of 150 μA/cm^2, was used to accelerate the corrosion of the tension bars. One of the beams was used as the control specimen with no corrosion. The remaining eight beams were divided into two groups: group CN, kept unloaded during the accelerated corrosion period, and group CS, corroded under a sustained loading that caused a mid-span moment equal to 60% of the yield moment. After 50, 110, 210, and 310 days of accelerated corrosion, the flexural strengths of the beams were examined under four-point bending tests. Thereafter, steel coupons, 200 mm in length, were extracted from the beams and their maximum and average mass loss, summarized in Table 4.6, were measured.

The higher corrosion damage of the CS-50 and CS-110 beams, compared to the CN-50 and CN-110 beams, can be explained by easier penetration of oxygen and moisture through the flexural cracks caused by sustained loading. In addition, due to easier diffusion of chloride ions, steel depassivation can occur in a shorter time in the beams with sustained loading. Hence, in agreement with the Austin et al. (2004) assertion about the variable t in Eq. 3.2 (Faraday's law), a greater portion of the total time of the tests was devoted to corrosion of the tension reinforcement. The only contradiction to this reasoning is the average mass loss of the CN-310 beam being greater than that of the CS-310 beam. In conclusion, the following observations were made in these experiments:

1. The beams with sustained loading initially experienced a higher rate of corrosion, resulting in a greater reduction in strength, compared to the beams with no sustained loading. However, the reduction in strength was independent of the sustained loading at high degrees of corrosion.
2. Sustained loading during the corrosion period significantly decreased the cracking time and increased the width of cracks caused by corrosion.
3. The ductility of the beams with less than 15% average cross-sectional loss of the tension reinforcement was increased.

Table 4.6: Maximum and average mass loss of the steel coupons extracted from Maaddawy et al. (2005) beams

Beam	Maximum (%)	Average (%)	Beam	Maximum (%)	Average (%)
CN-50	9.2	8.9	CS-50	10.9	9.7
CN-110	14.8	14.2	CS-110	18.5	15.4
CN-210	24.8	22.2	CS-210	25.2	22.8
CN-310	33.0	31.6	CS-310	31.5	30.0

The finite element model of the beams, constructed in FormWorks, is shown in Figure 4.8. Corroded steel was assigned as the material type of the middle 1400 mm length of the tension reinforcement. Normal steel was used as the material type for the rest of the reinforcing bars. Although, the middle portion of the beams had a much smaller out-of-plane reinforcement ratio, the stirrups in the out-of-plane direction were smeared uniformly throughout the length of the beams. This simplifying assumption was considered not to have a noticeable effect on the flexural response of the beams. Only the CN group of beams were modelled in VecTor2. The difference in the average mass loss of the corroded reinforcement of the CN and CS beams was deemed negligible. The finite element models were loaded with a monotonically increasing nodal displacement with increments of 1 mm up to failure.

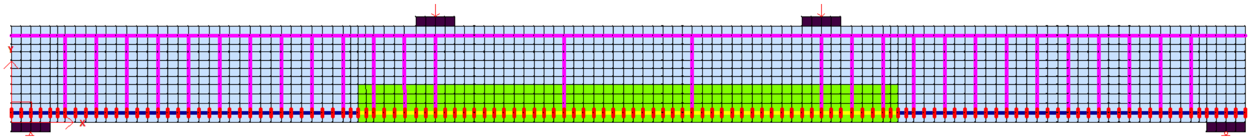

Figure 4.8: Finite element model of Maaddawy et al. (2005) beams

The load-deflection curves from the VecTor2 models are compared to the experimental responses in Figure 4.9. The ultimate strength and the load that caused yielding of the tension reinforcement were captured perfectly by VecTor2 as summarized in Table 4.7. The increase in the mid-span deflection at the ultimate load, observed after 50 and 110 days of corrosion, can be attributed to the reduction of the tension reinforcement cross-sectional area, resulting in a smaller flexural stiffness. On the other hand, the decreased ductility of the CN-210 and CN-310 beams might be due to the prevailing effect of pitting corrosion in a longer period of corrosion exposure.

Table 4.7: Experimental versus calculated response of Maaddawy et al. (2005) beams

Specimen	Experimental				VecTor2				VecTor2/Experimental			
	P_y	Δ_y	P_u	Δ_u	P_y	Δ_y	P_u	Δ_u	P_y	Δ_y	P_u	Δ_u
Control	67.20	15.63	75.00	73.33	68.00	14.00	81.71	78.63	1.01	0.90	1.09	1.07
CN-50	61.71	14.39	70.22	88.96	60.90	13.00	74.41	54.95	0.99	0.90	1.06	0.62
CN-110	57.39	13.91	66.76	78.39	58.60	13.00	70.37	66.40	1.02	0.93	1.05	0.85
CN-210	50.74	12.96	60.02	62.38	50.50	12.00	62.75	77.23	1.00	0.93	1.05	1.24
CN-310	44.16	11.74	53.27	58.96	46.60	12.00	56.82	85.04	1.06	1.02	1.07	1.44
								Mean	1.01	0.94	1.06	1.04
								C.O.V (%)	2.70	4.93	1.67	32.14

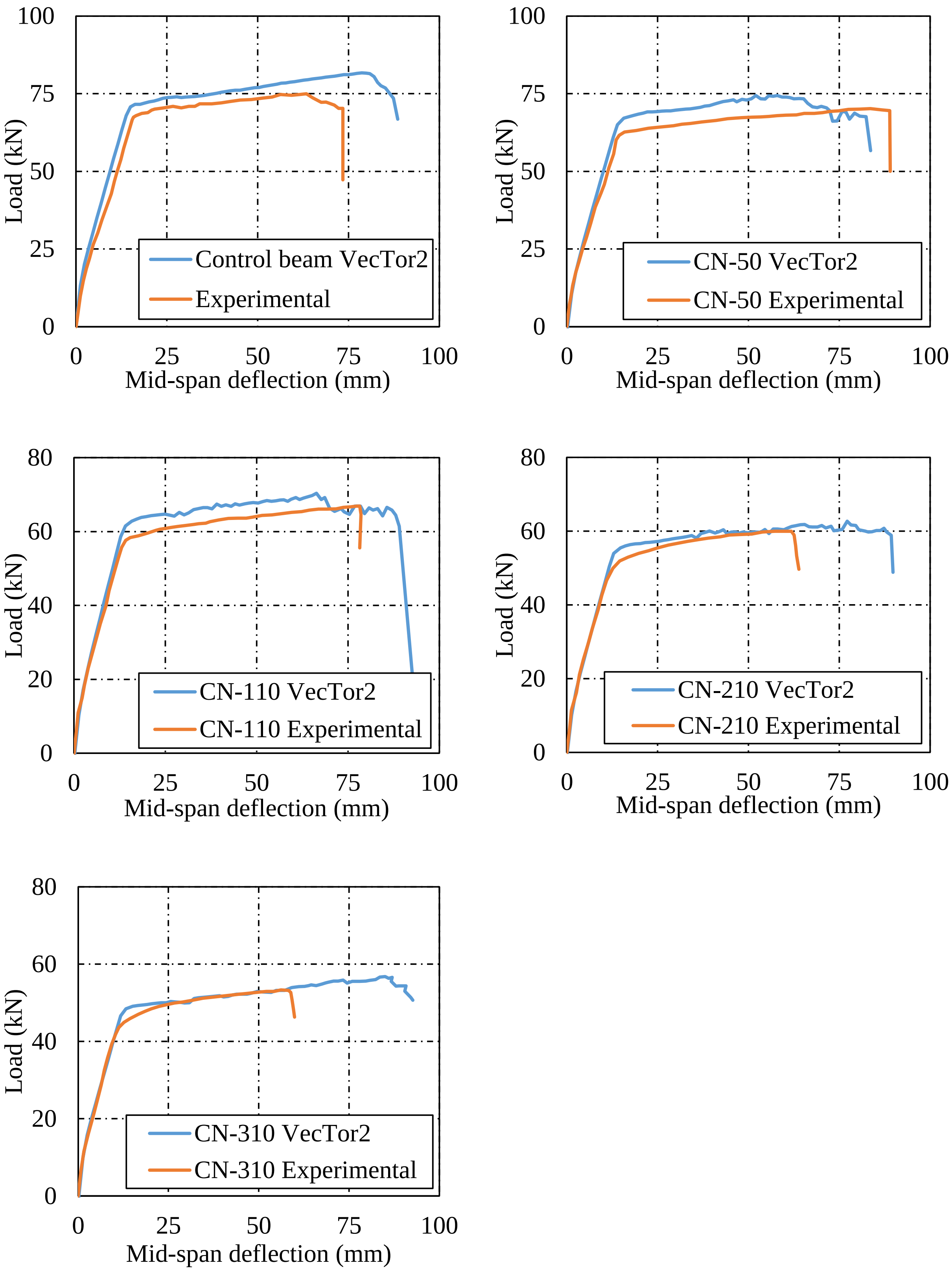

Figure 4.9: Load-deflection curves of Maaddawy et al. (2005) beams

The longitudinal cracks due to corrosion, observed in the experiments, were compared with the corrosion cracks of the finite element model of the CN-310 beam, as depicted in Figure 4.10. Despite the uncertainties associated with cracking of plain concrete in tension, the cover cracking model employed and the VecTor methodology explained in Section 3.2 predicted the width of the longitudinal cracks caused by corrosion with a reasonable accuracy. The fluctuations in the width of corrosion cracks, observed in the VecTor2 model, were due to the confining action of the stirrups.

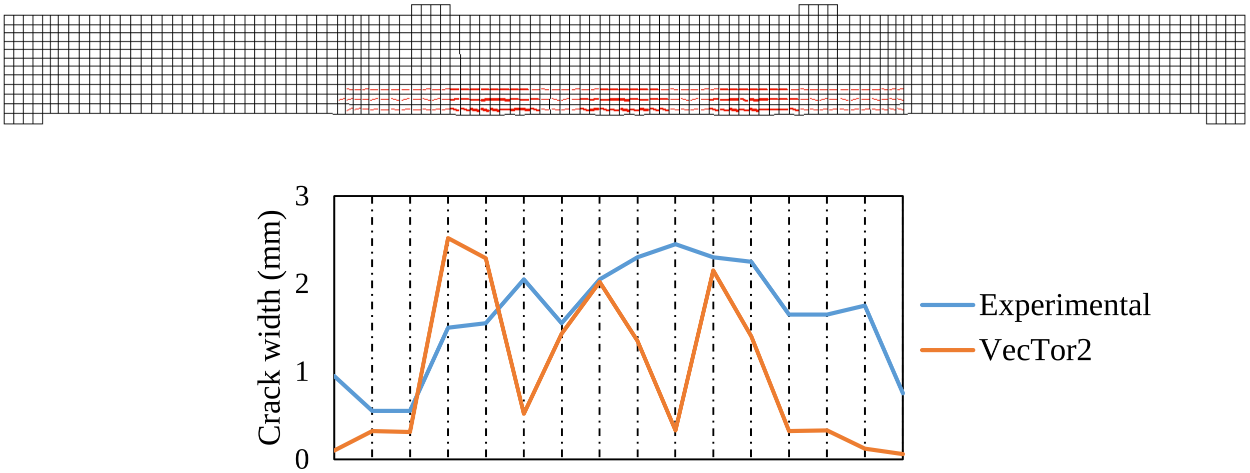

Figure 4.10: Experimental versus modelled longitudinal cracking of the cover concrete due to corrosion

4.3 Du et al. (2007)

Du et al. (2007) carried out an experimental program to study the effects of steel corrosion on the failure mode of reinforced concrete beams. Nineteen reinforced concrete beams, in four groups of highly under-reinforced, under-reinforced, balanced, and over-reinforced beams, were constructed and tested to failure. The beams were loaded with incremental loading up to yielding of the tension reinforcement and then with increments of mid-span deflection up to failure. The variables of the tests were the area and type of the tension reinforcement, the location of the corroded reinforcement, and the degree of corrosion. The mechanical properties of the reinforcing bars are given in Table 4.8. The beams had the same dimensions of 150 mm × 200 mm × 2100 mm. They were reinforced with 0.56 or 0.87% compression reinforcement, 8 mm diameter stirrups spaced at 150 mm, and 0.87, 1.6, 3.5, or 6.2% tension reinforcement as summarized in Table 4.9.

In order to achieve the desired level of corrosion in a reasonable time, sodium chloride was added to the concrete mixture used in casting the middle 600 mm of the length of the beams as depicted in Figure 4.11. The reinforcing bars were corroded by means of passing a direct current through them. Afterward, the beams were simply supported over a length of 1800 mm and tested under four-point bending with a constant moment span of 300 mm. The current was applied only to the compression, tension, or transverse reinforcement of each specimen located in the salted region. The contact points of the bars were taped to prevent the passage of current from one bar to another. However, the high electrical conductivity of the chloride saturated concrete provided an alternative path for the current, resulting in corrosion of all of the reinforcing bars located in the salted zone. On the other hand, there were no signs of corrosion in the bars located in the unsaturated regions.

Table 4.8: Mechanical properties of reinforcing bars used in Du et al. (2007) specimens

Type		Smooth	Deformed			
No.		R12	T08	T12	T16	T32
Diameter	(mm)	12.5	7.91	12.01	15.92	31.61
Yield strength	(MPa)	385	526	489	529	498
Ultimate strength	(MPa)	539	619	595	627	604
Elasticity	(GPa)	199	203	202	201	211
Yield strain	($\times10^{-3}$)	1.9	2.6	2.4	2.6	2.5
Hardening strain	($\times10^{-3}$)	25	22	20	19	17
Ultimate strain	($\times10^{-3}$)	203	82	132	116	123

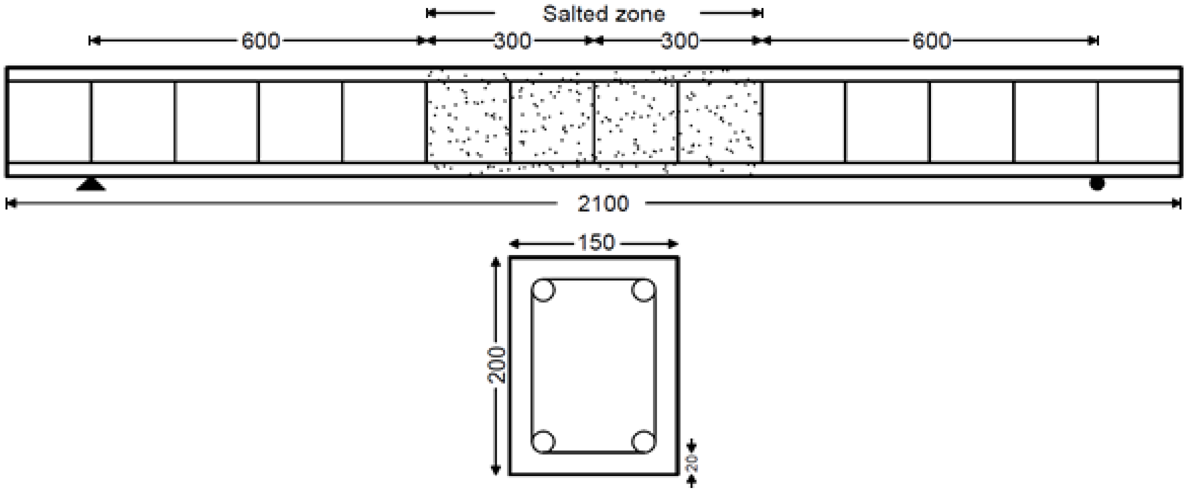

Figure 4.11: Du et al. (2007) test specimen

Table 4.9 : Details of the Du et al. (2007) beams

Beam Type	Beam	f'_{cu} (MPa)	Reinforcement			Corroded bar	I_{corr} (mA/cm^2)	Corrosion time (days)
			Tension	Compression	Transverse			
Over-reinforced	C120A	48.5	2-D32	2-T12	T8@150mm	Control	0.00	0
	C120B	37.2	2-D32	2-T12	T8@150mm	Control	0.00	0
	T322	43.8	2-D32	2-T12	T8@150mm	Tensile	0.90	60
	C124	49.1	2-D32	2-T12	T8@150mm	Compressive	0.35	120
Balanced	T160	48.1	4-D16	2-T12	T8@150mm	Control	0.00	0
	T162	48.6	4-D16	2-T12	T8@150mm	Tensile	0.45	60
	T163	48.6	4-D16	2-T12	T8@150mm	Tensile	0.45	90
	C162	49.6	4-D16	2-T12	T8@150mm	Compressive	0.35	60
Under-reinforced	T680	35.7	2-D16	2-T8	T8@150mm	Control	0.00	0
	T682	35.7	2-D16	2-T8	T8@150mm	Tensile	0.45	60
Very under-reinforced	T280	35.8	2-D12	2-T8	T8@150mm	Control beam	0.00	0
	T282	44.5	2-D12	2-T8	T8@150mm	Tensile	0.35	60
	T120A	47.1	2-D12	2-T12	T8@150mm	Control	0.00	0
	T120B	34.4	2-D12	2-T12	T8@150mm	Control	0.00	0
	T122	47.1	2-D12	2-T12	T8@150mm	Tensile	0.35	60
	R120	35.2	2-R12	2-T12	T8@150mm	Control	0.00	0
	R122	35.2	2-R12	2-T12	T8@150mm	Tensile	0.35	60

The cross-sectional loss of the tension and compression reinforcing bars was measured by the gravimetric method which represents the average cross-sectional loss. Corrosion of the links was quantified by measuring the maximum cross-sectional loss. The cross-sectional loss due to corrosion ranged from 2.4% to 11.5% for the tension bars, 6.6% to 13.5% for the compression bars, and 23% to 68% for the stirrups. The following conclusions were drawn from these tests:

- Corrosion caused the over-reinforced beams to fail in a less brittle manner either due to a reduction of the reinforcement ratio by corrosion of the tension bars or because of the cracks which developed within the compression zone of the beams as a result of corrosion of the compression bars.
- The under-reinforced beams failed in a less ductile manner as a result of reduced ductility of the reinforcement due to pitting corrosion and degradation of the bond between the reinforcement and concrete.

- Only 10% corrosion was enough to transform the failure mode of the highly under-reinforced beams from ductile to extremely brittle, failing due to the rupture of the corroded tension bars.

The finite element model of the beams is shown in Figure 4.12. The cylinder compressive strength of concrete was assumed to be 80% of the cube strength. Other material properties of the concrete were not reported by Du et al. (2007). Thus, they were left as the default VecTor2 values. The reinforcing bars were modelled by discrete truss elements. The corroding portion of the reinforcement of each beam was modelled by corroded reinforcing steel material type as per Table 4.9. A total of 1339 rectangular elements and 315 truss elements were used to model each beam. The corroded reinforcement was connected to the concrete elements using link elements.

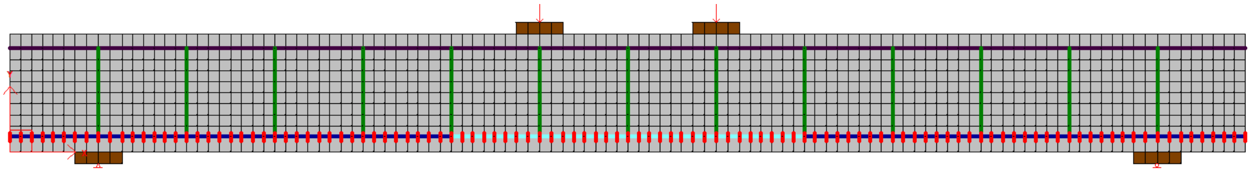

Figure 4.12: Finite element model of Du et al. (2007) beams

The load-deflection responses of the beams are depicted in Figure 4.13. The highly under-reinforced control beam, T280, was modeled twice: once with a perfect bond and once assuming an imperfect bond between the tension reinforcement and concrete. The strength of the beam was overestimated by the assumption of perfect bond. On the other hand, the ultimate strength was well predicted when assuming imperfect bond. However, the ultimate displacement of VecTor2 model was significantly smaller than that of the actual beam. Although, the experimental response of the T280 beam shows a clear yield plateau, the tension reinforcement of the VecTor2 model didn’t yield. Premature bond failure of the tension reinforcement in the vicinity of the constant moment region, accompanied by wide flexural cracks at either sides, caused the failure. Thus, the other control specimens were modelled with the assumption of imperfect bond. In every case the load-deflection curve up to failure was reasonably traced and the anticipated flexural behaviour was observed.

The corroded beams were modelled using the Feng et al. (2016) and Pantazopoulou and Papoulia (2001) models. Inaccuracies in the stiffness and ultimate displacement can be seen in the predicted load-deflection graphs. Almost every beam failed by crushing of the concrete at the top. However, due to bond failure, the tension reinforcement of the highly under-reinforcement beams didn't yield. In contrast, the tension reinforcement of the under-reinforced and balanced beams could yield with small slips occurring after the yielding of the reinforcement. Nevertheless, the slippage between the concrete and reinforcement was not significant. The balanced beam with corroded compression reinforcement, C124, failed by concrete crushing at the top in an early stage of loading mainly due to the reduction of the compression reinforcement area and loss of the composite action. The response of the over-reinforced beams was also well estimated by VecTor2.

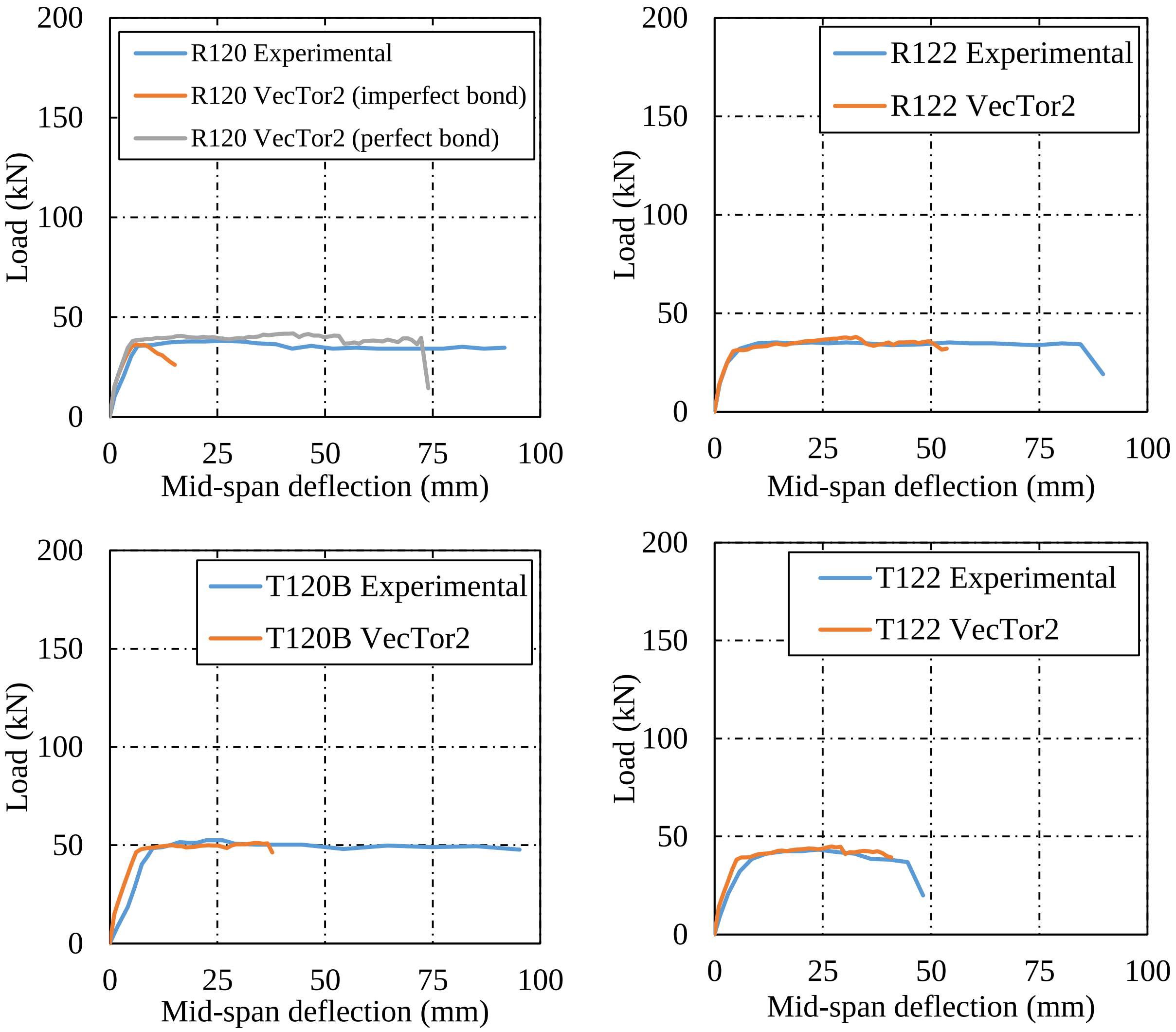

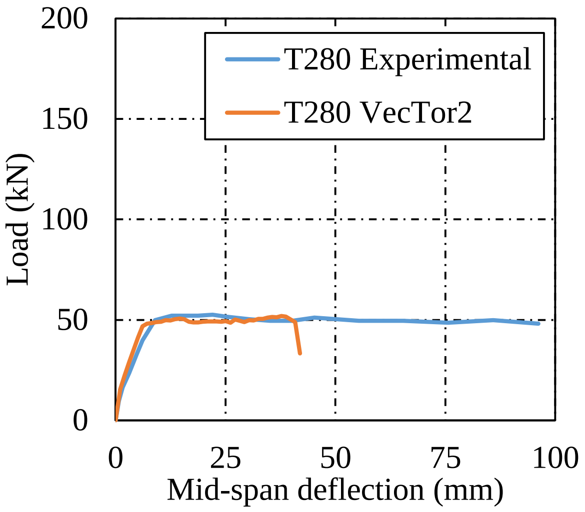
T280 Experimental
T280 VecTor2
Load (kN)
200
150
100
50
0
0
25
50
75
100
Mid-span deflection (mm)

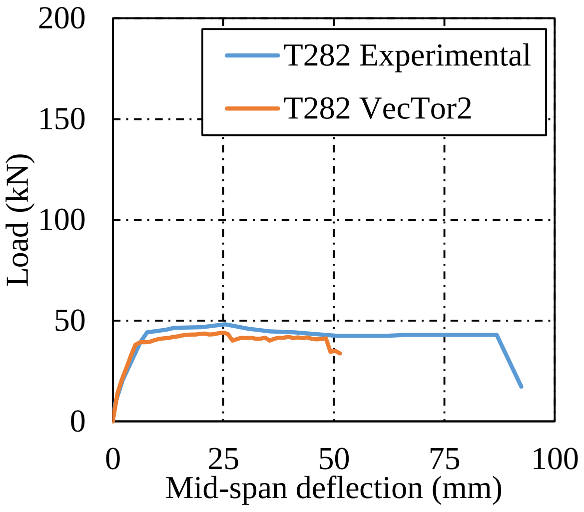
T282 Experimental
T282 VecTor2
Load (kN)
200
150
100
50
0
0
25
50
75
100
Mid-span deflection (mm)

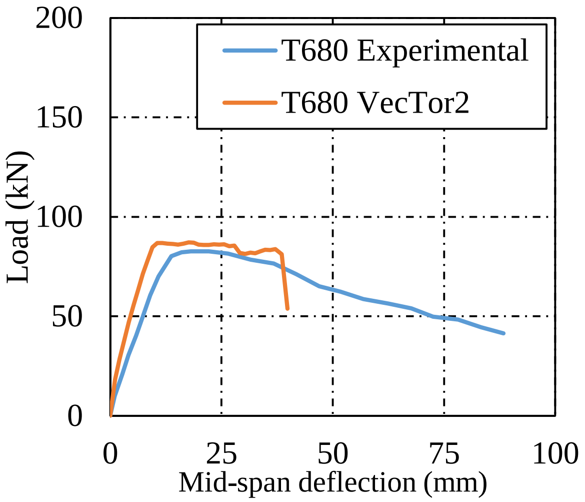
T680 Experimental
T680 VecTor2
Load (kN)
200
150
100
50
0
0
25
50
75
100
Mid-span deflection (mm)

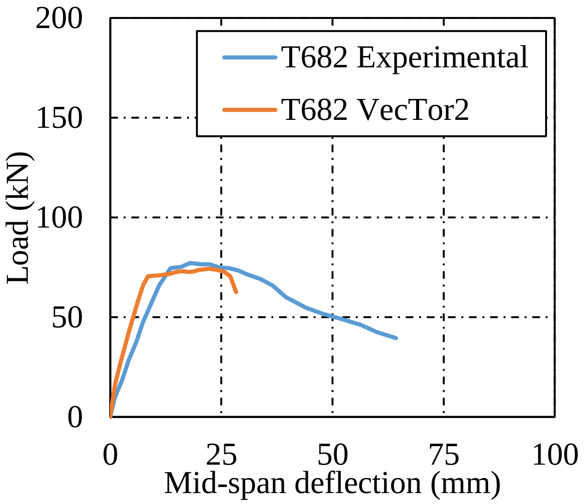
T682 Experimental
T682 VecTor2
Load (kN)
200
150
100
50
0
0
25
50
75
100
Mid-span deflection (mm)

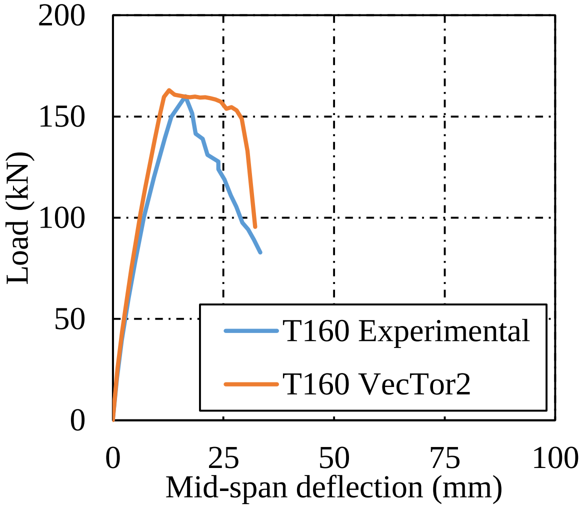
T160 Experimental
T160 VecTor2
Load (kN)
200
150
100
50
0
0
25
50
75
100
Mid-span deflection (mm)

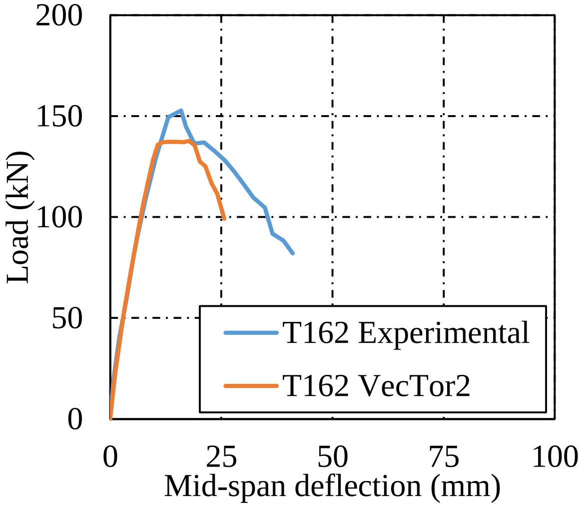
T162 Experimental
T162 VecTor2
Load (kN)
200
150
100
50
0
0
25
50
75
100
Mid-span deflection (mm)

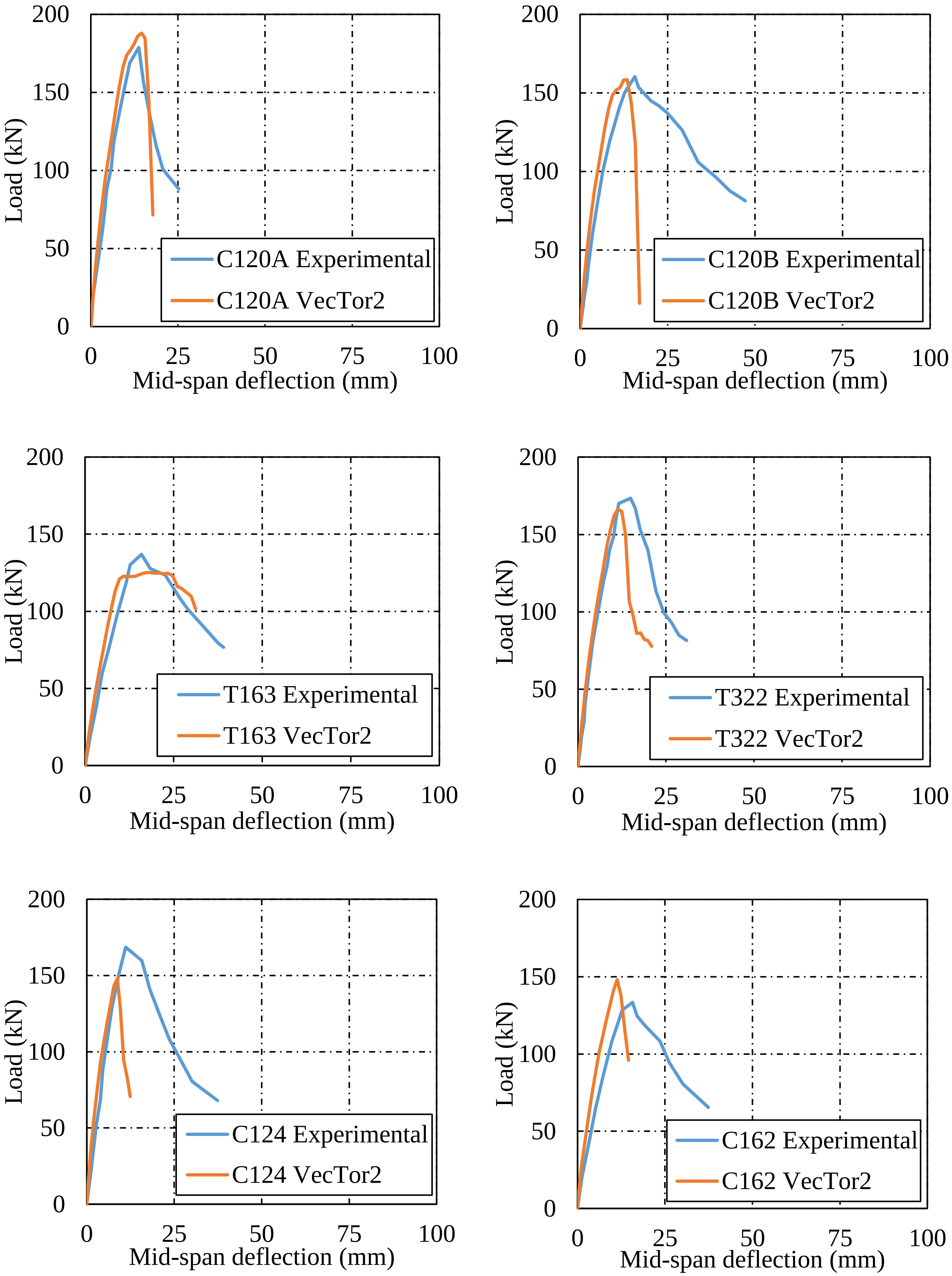

Figure 4.13: Load-deflection response of Du et al. (2007) beam specimens

In general, the response of corroded beams is very sensitive to the choice of the bond strength reduction model. The lack of a genuine formulation for the bond strength of corroded bars with different diameters is a barrier against accurate estimation of the ductility of a reinforced concrete beam. Formulations presented in Section 3.3 were all derived based on tests performed on corroded bars of certain type or diameter. Thus, the test results might not be applicable to specimens constructed with a different bar type or diameter. Furthermore, the random nature of corrosion damage in accelerated corrosion tests aggravates the situation even more. The pattern of cross-sectional loss of reinforcing bars in accelerated corrosion tests is not in the form of uniform nor pitting corrosion alone. Instead, it is a combination of the both types of corrosion, occurring simultaneously. The average cross-sectional loss is caused by carbonation of the concrete (uniform corrosion) while the spatial variability of cross-sectional loss is due to simultaneous uniform and pitting corrosion. How the two types of corrosion interact with each other and affect the response of a reinforced concrete is a matter of further study. The next chapter presents an attempt at overcoming some of the shortcomings of deterministic finite element modelling of corroded beams pointed out in this chapter.

5 Stochastic Modelling of Corroded Reinforced Concrete Beams

For a long time, researchers have focused on improving the constitutive laws and structural models that are employed in FE modelling of reinforced concrete. However, the intrinsic randomness of the mechanical properties of this material, and other phenomena associated with it such as corrosion, are such that deterministic modelling can lead to rough representations of reality. Thus, there is an inherent approximation in the predicted response of a reinforced concrete member employing classical methods. Increasing the accuracy of the constitutive models does not solve the problem of identification of such uncertainty. Accounting for the randomness and spatial variability of the mechanical properties of reinforced concrete can be achieved through stochastic finite element modelling (SFEM). In general, SFEM aims at evaluating the first two statistical moments (mean and variance) of the response quantities such as the load-carrying capacity of a beam (Sudret and Der Kiureghian, 2000). Such information can then be used for reliability analysis aimed at evaluating the probability of failure given a limit state function.

The two types of corrosion that lead to reduction in the cross-sectional area of a reinforcing bar, general (uniform) and pitting (localized) corrosion, are illustrated in Figure 5.1. Most of the previous experimental and analytical works on corrosion are based on the simplifying assumption of uniform cross-sectional loss over the whole length of a corroded reinforcing bar. Regardless of the type of corrosion, in-situ inspection of corroded bars has revealed the irregularity and heterogeneity of the spatial distribution of cross-sectional loss due to corrosion as shown in Figure 5.2. Another example is the beams tested by Yu et al. (2015) in which the ratio of local cross section loss to the average section loss varied from 0.2 to 3.5 at different locations along the length of the beams. Although the specimens were corroded under the same corrosive conditions, the average cross-sectional loss of every rebar, measured using the gravimetric method, was also different from the others. Gonzalez et al. (1995) found that the ratio of maximum corrosion penetration to the average value varied from 4 to 8 in naturally corroded concrete specimens. Tuutti (1982) suggested that this ratio varies from 4 to 10 for 5 mm and 10 mm diameter reinforcing bars. Thus, the randomness of corrosion not only effects the loss of cross section at a locality but also affects the average loss of cross-sectional area.

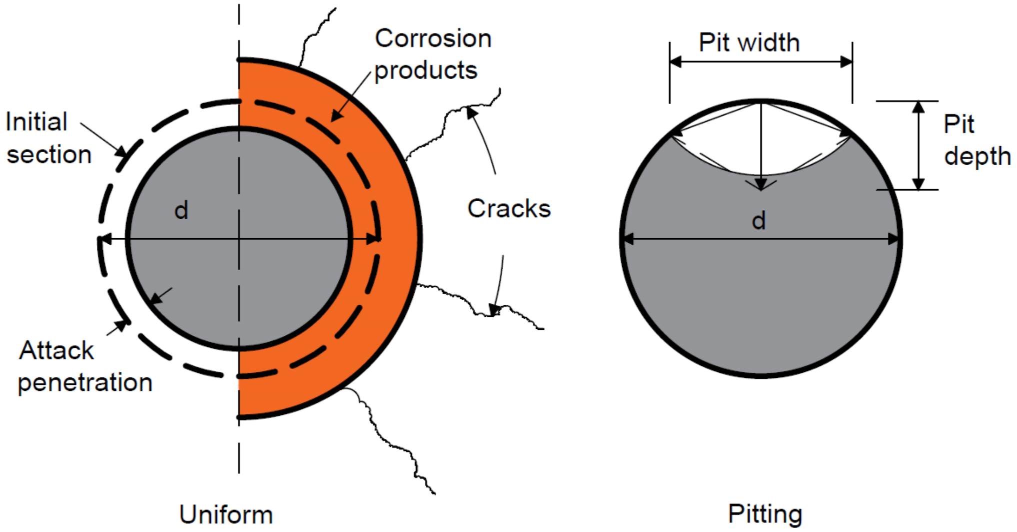

Figure 5.1: Cross-sectional loss due to different types of corrosion

This chapter describes the formulation used for stochastic analysis of corroded reinforced concrete beams in VecTor2. The description of uncertainties associated with corrosion was accomplished through the definition of random variables in the FE models. The selection of these variables was purely based on the available information in the literature. The framework required for stochastic simulation was previously implemented in VecTor2. The current version allows for random sampling from Normal, Lognormal, Beta, and Gamma probability distributions by employing Monte Carlo or Latin Hypercube sampling techniques. In order to generate a random sample, the implicit function RANDOM_NUMBER in Fortran is used. This function samples from a uniform probability distribution within the range 0 to 1. The uniform samples are transformed to the desired probability density function (PDF) using the Inverse CDF Method. In order to generate a random field, uncorrelated samples are transformed to correlated space through the Karhunen–Loeve Transform (KL transform). As part of this thesis, the formulation required for random sampling from a Gumbel distribution and the generation of Lognormal and Gamma random fields were added to this framework. For more information about the stochastic simulation tools available in VecTor2, the reader is referred to Hunter (2016). In order to highlight the potential applications, stochastic simulations of uniform and pitting corrosion of the Maaddawy et al. (2005) beams were performed. The outcome of this study should be interpreted only in a comparative sense. The formulation of each type of simulation along with the results are presented in the following sections.

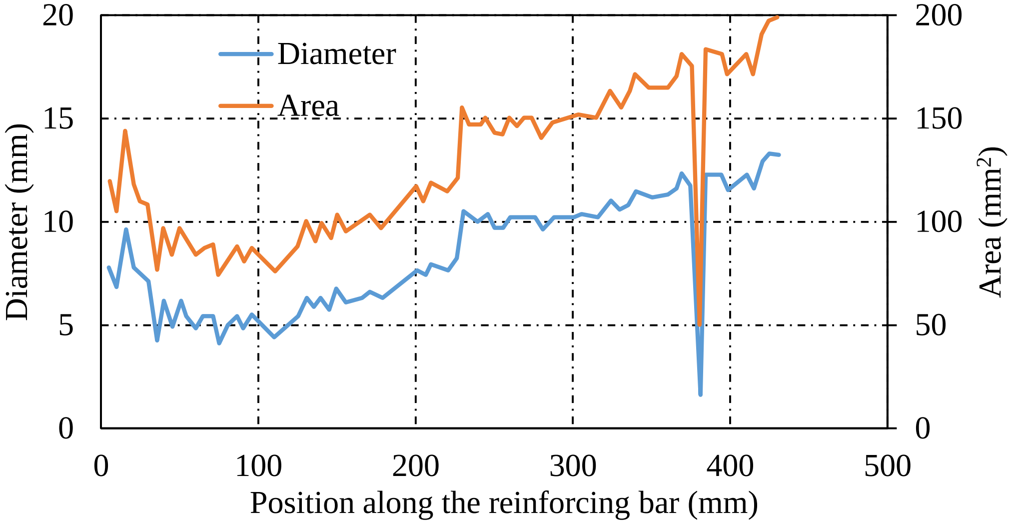

Figure 5.2: Variation in cross section and diameter of a corroded bar (Cairns et al., 2005)

5.1 Uniform corrosion

Stochastic modelling of uniform corrosion was performed through the description of a probability distribution function for corrosion current density (or the rate of corrosion). Note that there is a linear relationship between corrosion rate and corrosion current density, as given in Eq. 3.2. Thus, they can be used interchangeably from a statistical point of view. Assuming a reinforced concrete beam is discretized into m segments, as shown in Figure 5.3, corrosion current density can be modelled either as a single random variable (not considering the spatial variability) or a random field with a prescribed covariance matrix (considering the spatial variability).

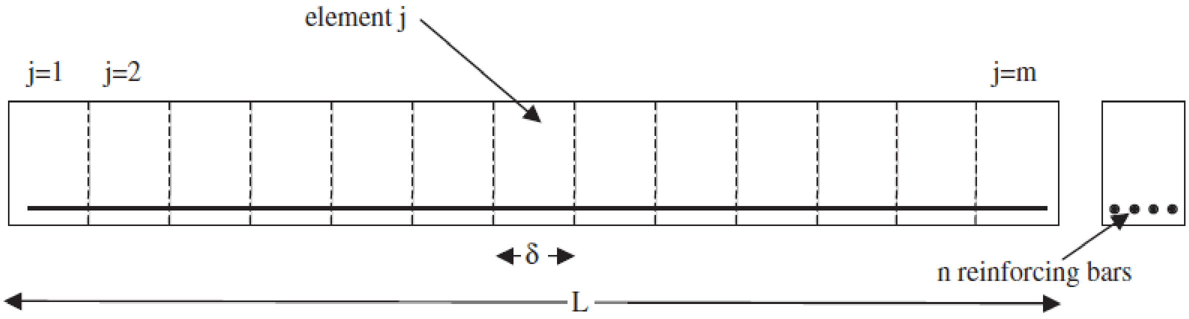

Figure 5.3: Discretization of a reinforced concrete beam

A specific statistical model for corrosion current density was not found in the literature. For an appropriate selection of the statistical parameters, the experimental results of Yu et al. (2015) were analyzed. Yu et al. (2015) examined the spatial distribution of the reinforcing steel cross-sectional loss by testing three identical beams, namely Bs02, Bs03, and Bs04, which were exposed to accelerated natural corrosion for 36, 19, and 27 months, respectively. The beams were 3000 mm long and had a cross section of 280 × 150 mm. They were reinforced with two 12 mm deformed bars in tension and two 6 mm deformed bars in compression. Double-legged 6 mm diameter stirrups spaced at 220 mm apart were used as the transverse reinforcement. The cross-sectional loss of the tension bars was quantified by measuring the weight loss of 10 mm pieces of reinforcing steel extracted from each beam. Despite the fact that the reinforcing bars of each beam were corroded in the same corrosive environment, the average and the pattern of cross-sectional loss were significantly different in each bar. The pattern of cross-sectional loss of each beam is shown in Figure 5.5.The coordinates of the points of each graph were extracted and the cross-sectional loss was converted to corrosion current density (or the rate of corrosion) using Faraday's law. The extracted data can be found in Appendix A. It was assumed that the collected data are part of a homogenous isotropic random field, Z, and the graphs in Figure 5.5 were treated as six realizations of this field. A random field is fully characterized over a spatial domain Ω by knowing the probability density function of every $x \in \Omega$ and the correlation of any pairs of random variables. This correlation is often given by a function that describes the spatial correlation of the points of the random field. If a random field is homogenous, the probability density function is independent of the location and the covariance function depends only on the distance. A lognormal probability distribution function was fitted to the values of the corrosion current density of each realization. The statistical parameters of the fitted distributions are given in Table 5.1. The fitted and the empirical PDF and CDF of the front bar of the Bs02 beam are shown in Figure 5.4.

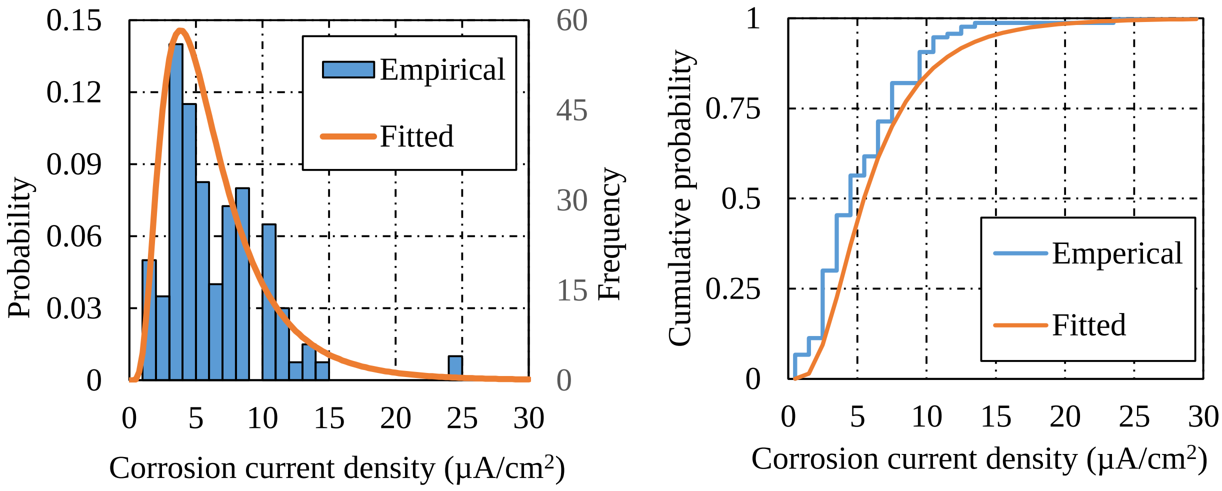

Figure 5.4: Empirical and fitted PDF (left), Empirical and fitted CDF (right)

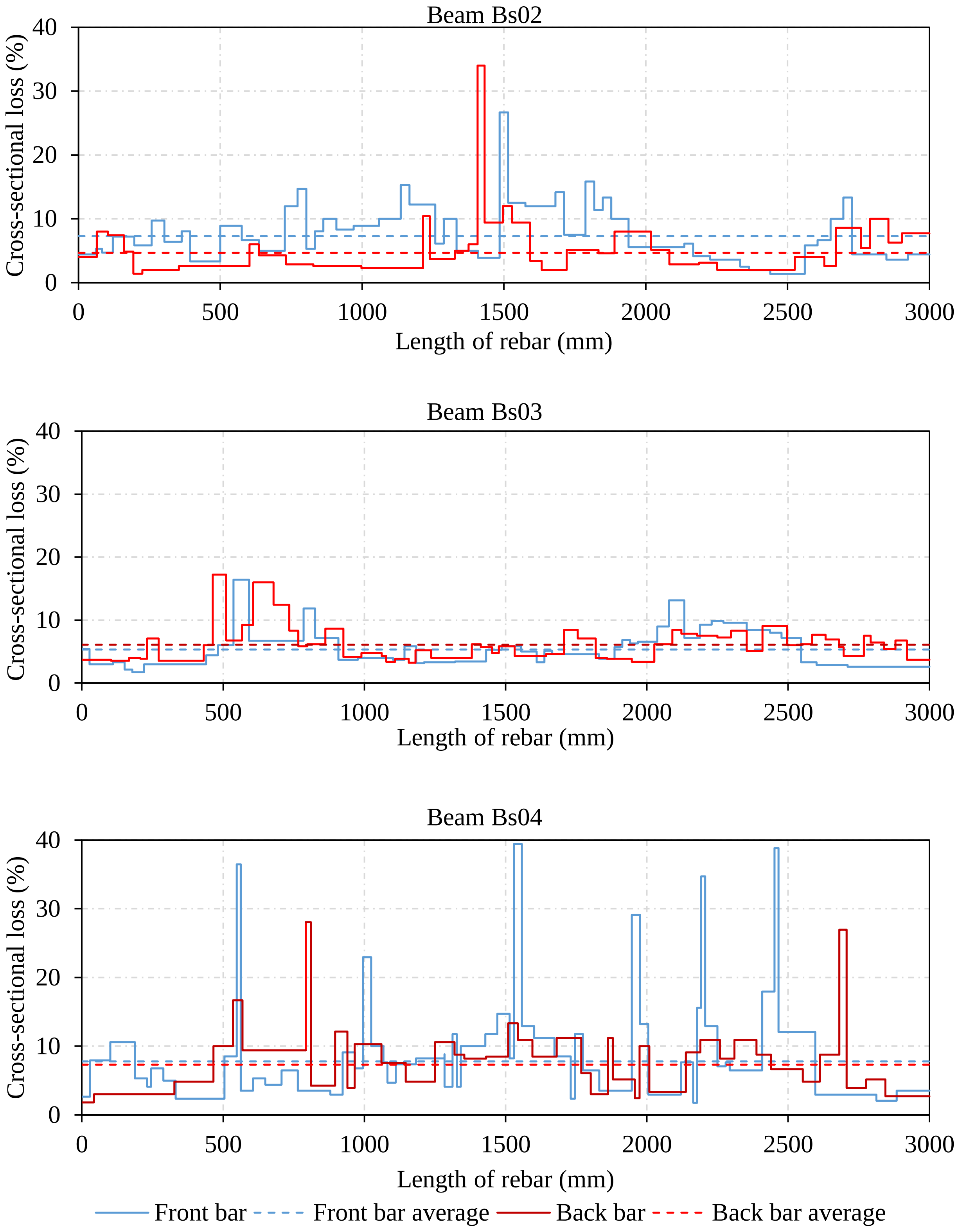

Figure 5.5: Cross-sectional loss of the corroded bars of Yu et al. (2015) beams

Table 5.1: Statistics of the lognormal distributions fitted to corrosion rates of Yu et al. (2015) beams

Beam	Bs02		Bs03		Bs04	
Rebar	Front	Back	Front	Back	Front	Back
μ	1.70	2.06	1.96	1.25	2.23	2.00
σ	0.60	0.49	0.70	0.54	0.40	0.56
COV	0.35	0.24	0.36	0.43	0.18	0.28
Mean	6.55	8.83	9.07	4.01	10.08	8.65
Standard deviation	2.79	2.45	5.71	1.34	1.77	3.22

In order to assess the spatial correlation of the random fields, an empirical semivariogram for each realization was constructed. In statistics, a semivariogram is a function that describes the degree of spatial dependence along a random field which is defined as the variance of the difference between the values at locations x_i and x_j. Since it was assumed that the realizations are isotropic, this variance is only a function of distance. The semivariograms were constructed by employing the following equation:

$$\hat{\gamma}(x) = \frac{1}{2n(x)} \sum_{x_i - x_j = x} (Z(x_i) - Z(x_j))^2 \tag{5.1}$$

where:

- x = lag distance defined as the distance between x_i and x_j
- $\hat{\gamma}(x)$ = empirical semivariance for lag distance x
- $Z(x_i)$ = measured value of random field at point x_i

The constructed semivariograms, shown in Figure 5.6, shared two common features. They started with a curve and leveled out at the end. Thus, an exponential covariance function which models the covariance as an exponential decay was assumed:

$$C(x) = \sigma^2 e^{-Bx} \tag{5.2}$$

where:

- B = scale parameter (inverse of the correlation length)
- σ^2 = variance of the random field
- x = linear distance

The semivariance of an isotropic random field can be described using its covariance function as follows:

$$\gamma(x) = \sigma^2(1 - e^{-Bx}) \tag{5.3}$$

The method proposed by Krajewski et al. (1986) was adopted to fit the semivariance function to the empirical semivariogram of each realization. The correlation length and variance of each realization estimated by this method are given in Table 5.2.

Table 5.2: Estimated parameters of the covariance function

Realization	B (1/mm)	Correlation length (mm)	σ^2
Beam Bs02 - Front bar	0.0035	286	15.0
Beam Bs02 - Back bar	0.0065	154	10.5
Beam Bs03 - Front bar	0.0037	270	23.8
Beam Bs03 - Back bar	0.0051	196	24.2
Beam Bs04 - Front bar	0.0108	93	74.0
Beam Bs04 - Back bar	0.0098	102	24.4

The first series of stochastic simulations were performed without considering the spatial variability of corrosion current density. In other words, the rate of corrosion was modelled as a single variable in each simulation. A lognormal distribution with a mean of 150 µA/cm^2 and a coefficient of variation (COV) of 0.30 was used for random sampling of corrosion current density. The selection of the value of COV was based on the value suggested by Val et al. (1998) and the coefficient of variations observed in Yu et al. (2005) beams. In order to choose an appropriate number of simulations, the CN-50 beam was modelled 400, 200, 100, and 50 times. Each beam was loaded up to failure with a monotonically increasing nodal displacement at mid-span with increments of 1 mm. The value of the failure load and mid-span deflection at ultimate load were extracted from the outputs of VecTor2 using a MATLAB script. The mean and COV of the failure loads and mid-span deflections at failure load are presented in Table 5.3. From these values, it was concluded that 100 simulations provided sufficient accuracy for estimations of the statistical parameters. A typical plot of the stochastic simulation results is shown in Figure 5.7. It’s noteworthy that an average failure load very close to the experimental value was observed. However, there was great variability in the predicted mid-span deflection at failure.

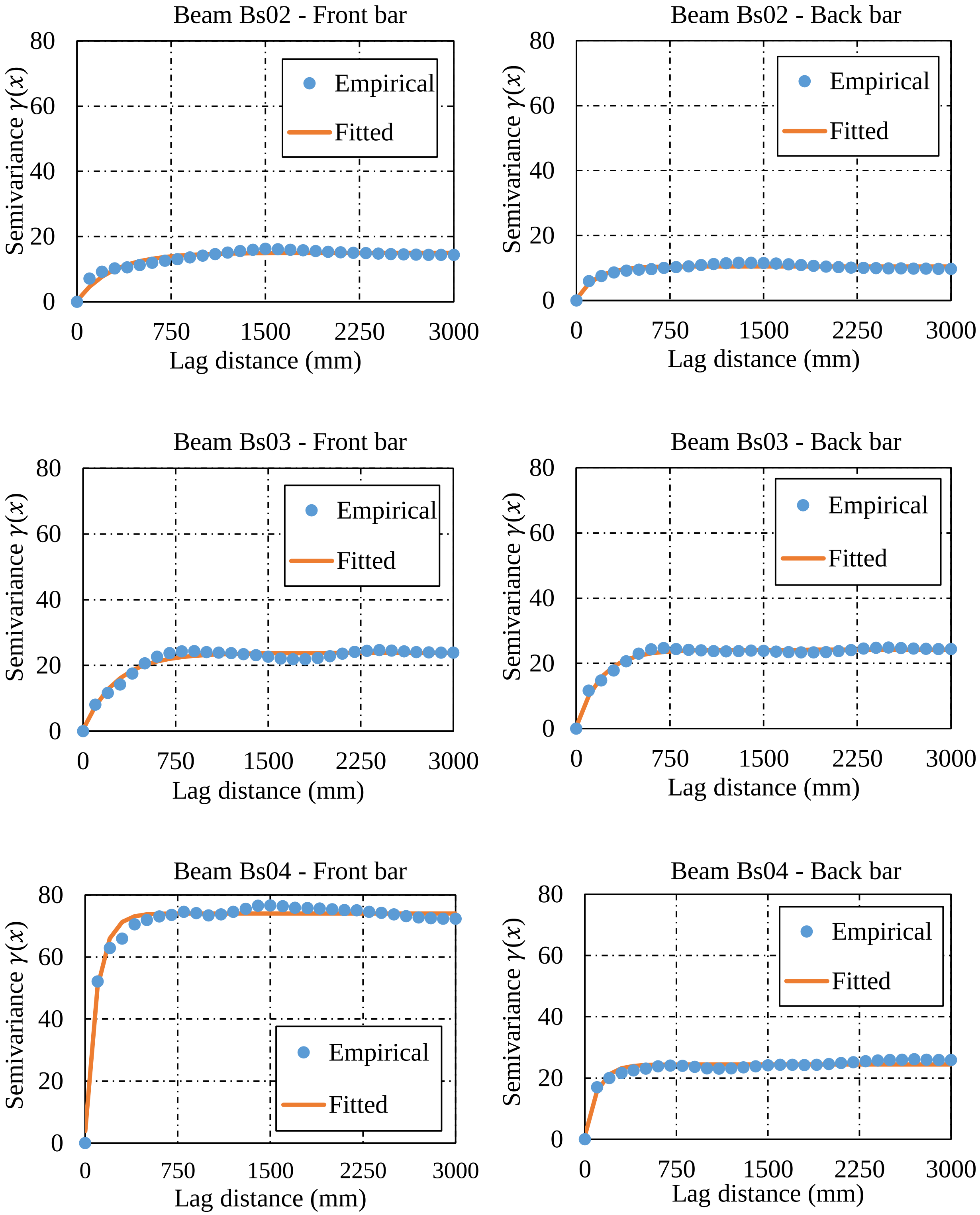

Figure 5.6: Empirical and fitted semivariogram of corrosion current densities extracted from Yu et al. (2015) beams

Table 5.3: Stochastic simulation results of the CN-50 beam

	No. of simulations	400	200	100	50
Failure load (kN)	Mean	74.2	73.9	75.0	73.9
	Variance	3.3	3.3	3.3	1.9
	COV	2.5%	2.4%	2.4%	1.9%
Mid-span deflection at failure (mm)	Mean	66.5	66.8	69.5	69.1
	Variance	76.2	70.0	85.6	53.5
	COV	13.1%	12.5%	13.3%	10.6%

Stochastic simulations with 100 runs were also performed for the CN-110, CN-210, and CN-310 beams. The load deflection curves obtained for each beam are given in Appendix B. The COV of the failure load and mid-span deflection at failure significantly increased with increasing corrosion time. The statistical parameters of failure load and mid-span deflection at failure, compared with the experimental results and the values predicted by deterministic analysis, are given in Table 5.4. A linear relationship between the corrosion current density and the failure load was observed. However, there was no meaningful relationship between the corrosion current density and the mid-span deflection at failure as illustrated in Figure 5.8.

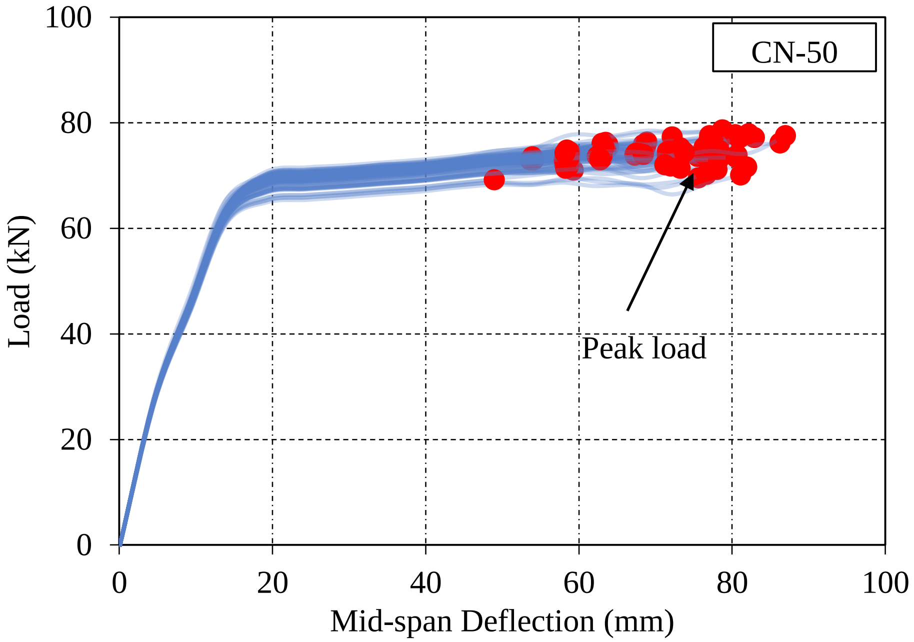

Figure 5.7: Stochastic simulation results of the CN-50 beam

Table 5.4: Stochastic simulation results

	Beam	Stochastic		Deterministic	Experimental
		Average	COV		
Failure load (kN)	CN-50	75.00	2.4%	74.41	70.22
	CN-110	68.31	4.3%	70.37	66.76
	CN-210	61.38	6.1%	62.75	60.02
	CN-310	55.02	9.5%	56.82	53.27
Mid-span deflection (mm)	Beam	Stochastic		Deterministic	Experimental
		Average	COV		
	CN-50	69.52	13.3%	54.95	88.96
	CN-110	68.32	15.3%	66.40	78.39
	CN-210	71.62	15.2%	77.23	62.38
	CN-310	80.73	11.1%	85.05	58.96

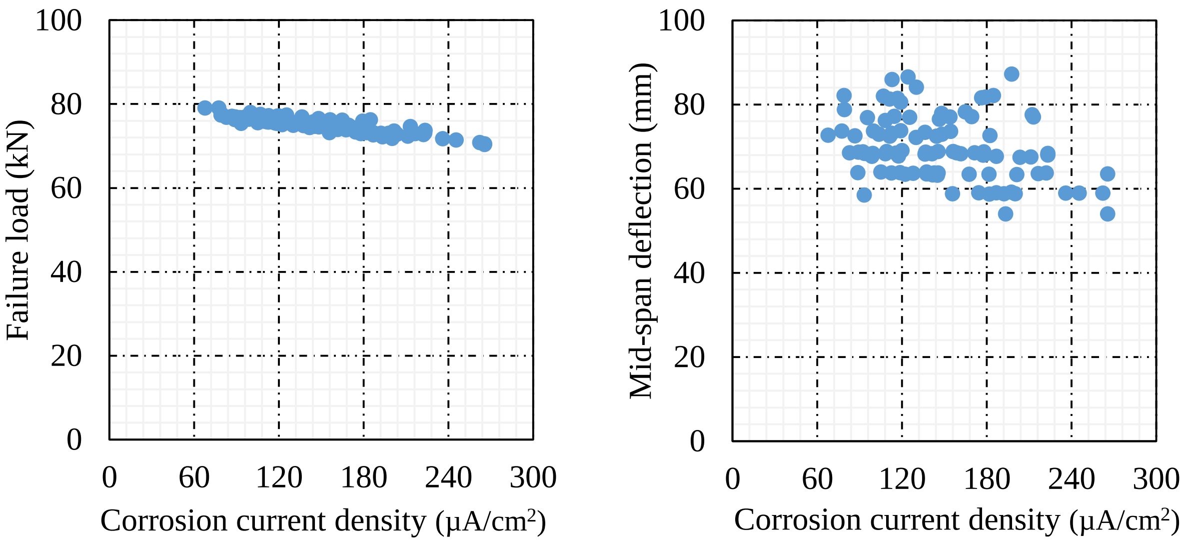

Figure 5.8: Scatter plots of corrosion current density, failure load and mid-span deflection at failure of the CN-50 beam

Random field simulation of uniform corrosion was performed by employing the same lognormal probability density function. The covariance matrix was constructed by employing Eq. 5.2. In order to assess the effect of correlation length on the stochastic simulations, the CN-50 beam was modelled with four different correlation lengths of 1200, 600, 300, and 0 mm. For each correlation length, 100 simulations were performed. The load-deflection curves can be found in Appendix B. The statistics of the response quantities of the stochastic simulations are also given in Table 5.5. In general, the variation in failure load slightly increased with an increased correlation length. The maximum and average of each random field are depicted in Figure 5.9 . As can be noted from these figures, increasing the correlation length significantly increases the variation in the average and decreases the variance of a random field. In other words, a large correlation length relative to the field length causes a smooth realization with relatively small fluctuations around the average value. Scatter plots of the average corrosion current density and standard deviation of the generated random fields, depicted in Figure 5.10, also confirm this observation. Thus, the greater variation in the failure load of the simulations with a large correlation length shows that the response of a lightly corroded reinforced concrete beam (CN-50 in this case) is more sensitive to the average cross-sectional loss rather than the maximum loss at a locality. In conclusion, the simulation of corrosion current density (or corrosion rate) as a random field has only a minor effect on the response. Thus, focus should be directed toward the randomness of the average value of the corrosion current density as a single random variable as it can be significantly different in two reinforcing bars located in the same beam and corroded under the same corrosive conditions, as was illustrated in Figure 5.5.

Table 5.5: Random field simulation results of the CN-50 beam

Correlation length (mm)	Failure load (kN)		Mid-span deflection (mm)	
	Average	COV	Average	COV
0	75.15	1.4%	67.71	11.0%
300	74.45	2.0%	67.91	10.5%
600	74.68	1.9%	69.04	10.4%
1200	74.51	2.1%	69.34	11.4%

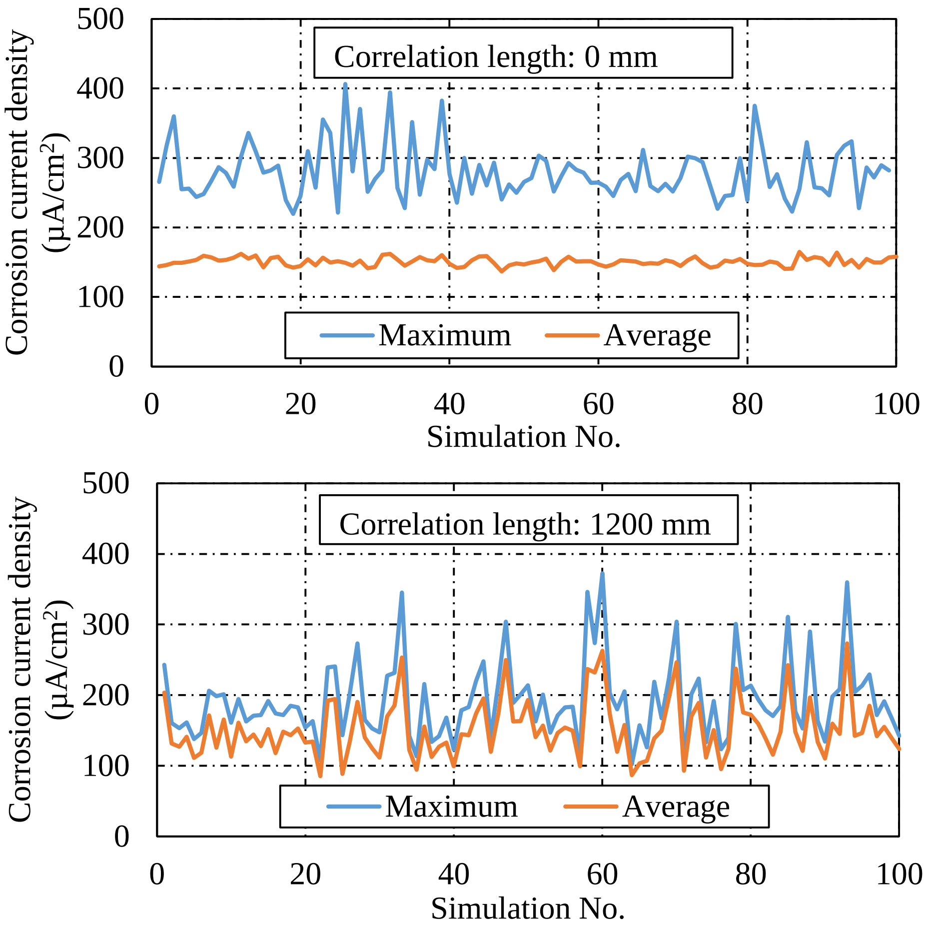

Figure 5.9: The average and maximum of 100 random field simulations

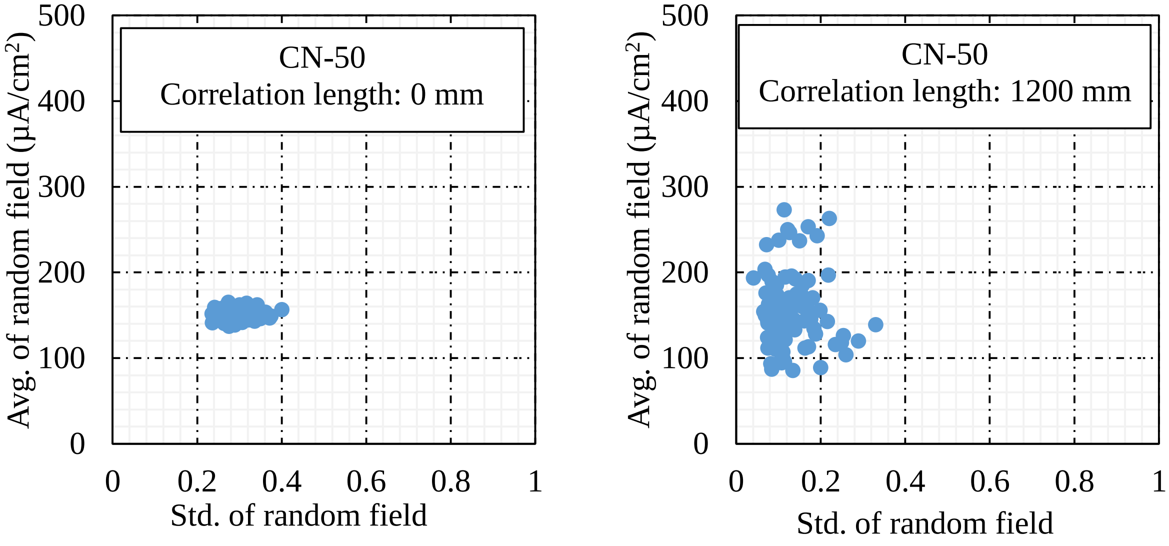

Figure 5.10: Scatter plots of the average and standard deviation of the generated random fields

5.2 Pitting corrosion

Pitting corrosion was modelled by employing the methodology proposed by Stewart and Al-Harthy (2008). Based on a statistical analysis of the maximum pit depths, measured over a 100 mm long reinforcing bar corroded in an accelerated corrosion test, they proposed a Gumbel (generalized extreme value distribution Type-I) distribution for the pitting factor. The probability density function of this distribution is given in Eq. 5.4 where μ and β are the location and scale parameters of the distribution, respectively. Random sampling from the Gumbel distribution was done by generating a uniform sample and transforming this sample to a Gumbel distribution using the cumulative probability function given in Eq. 5.5. The distribution was assumed to be time invariant and was truncated at x = 1. The shape of the Gumbel distributions given for 16 mm and 27 mm reinforcing bars are shown in Figure 5.11. The probability of a pitting factor smaller than 3 for a 16 mm diameter bar is almost zero. Analogously, a pitting factor smaller than 4 is unexpected for a 27 mm bar. The statistics of this distribution are given in Table 5.6. To predict the statistics for a length or diameter other than the ones given in Table 5.6, the statistical parameters should be modified by employing Eq. 5.6 and Eq. 5.7 where D_0, μ_0, and β_0 are given in Table 5.6.

$$f(x) = \frac{1}{\beta} e^{-\frac{x-\mu}{\beta}} e^{-e^{-\frac{x-\mu}{\beta}}} \tag{5.4}$$

$$F(x) = e^{-e^{-\frac{x-\mu}{\beta}}} \tag{5.5}$$

$$\mu = \mu_0 + \frac{1}{\beta_0} \ln\left(\frac{D^2}{{D_0}^2}\right) \tag{5.6}$$

$$\beta = \beta_0 \tag{5.7}$$

Table 5.6: Statistics of pitting factor. Taken from Stewart and Al-Harthy (2008)

Reinforcing bar		Pitting factor R		Gumbel parameters	
Length (mm)	Diameter (mm)	Mean	COV	μ_0	β_0
100	16	6.2	0.18	5.56	1.16
100	27	7.1	0.17	6.55	1.07

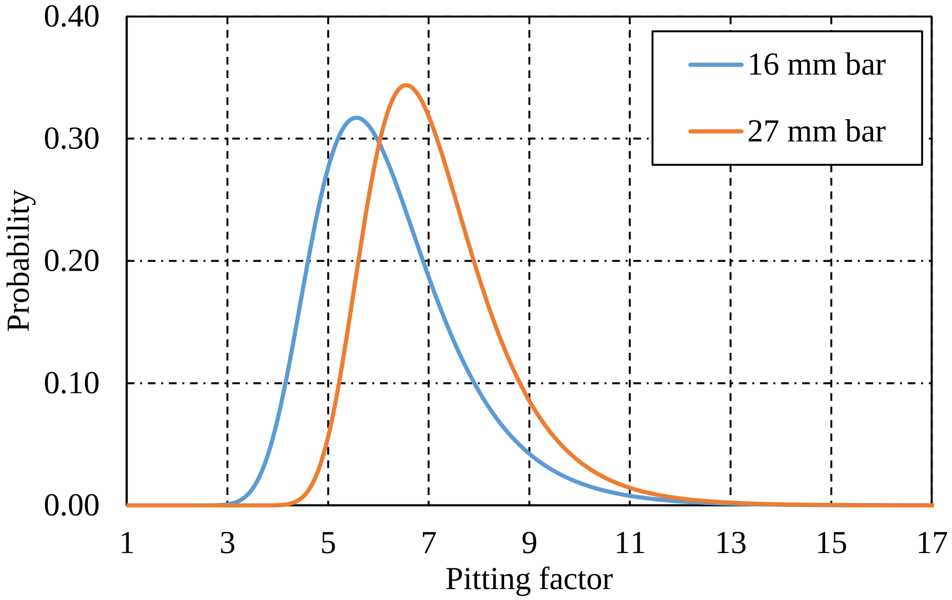

Figure 5.11: Gumbel probability distribution function for pitting factor suggested by Stewart and Al-Harthy (2008)

For the sake of comparison, the beams tested by Maaddawy et al. (2005) were modelled again. For every corroded truss element, a random pitting factor was generated and the cross-sectional loss due to pitting corrosion of the corroded truss elements was calculated based on the formulations presented in Section 3.1. The diameter of the reinforcing bars used in the Maaddawy et al. (2005) beams was 16 mm. Thus, the statistics given in Table 5.6 were directly used. Due to lack of information about the spatial correlation of pitting factors along the length of a corroded bar, a nugget-effect model described by Eq. 5.8 was used to populate the covariance matrix. Stochastic simulation results for the CN-110 beam are shown in Figure 5.12. The load-deflection responses of other beams can be found in Appendix B. Compared with uniform corrosion, a significantly greater scatter in the failure load and mid-span deflection at failure can be observed. The average and COV of the failure load and mid-span deflection are given in Table 5.7.

$$C_{ij} = \begin{cases} C_0 \ \ if \ \left|\Delta x_{ij}\right| = 0 \\ 0 \ \ if \ \left|\Delta x_{ij}\right| > 0 \end{cases} \tag{5.8}$$

Table 5.7: Stochastic simulation results for pitting corrosion

Beam	Failure load (kN)		Mid-span deflection (mm)	
	Average	COV	Average	COV
CN-50	77.1	1.4%	73.5	11.1%
CN-110	57.8	6.7%	29.5	35.7%
CN-210	31.1	21.6%	16.2	40.2%
CN-310	12.8	17.1%	5.31	42.7%

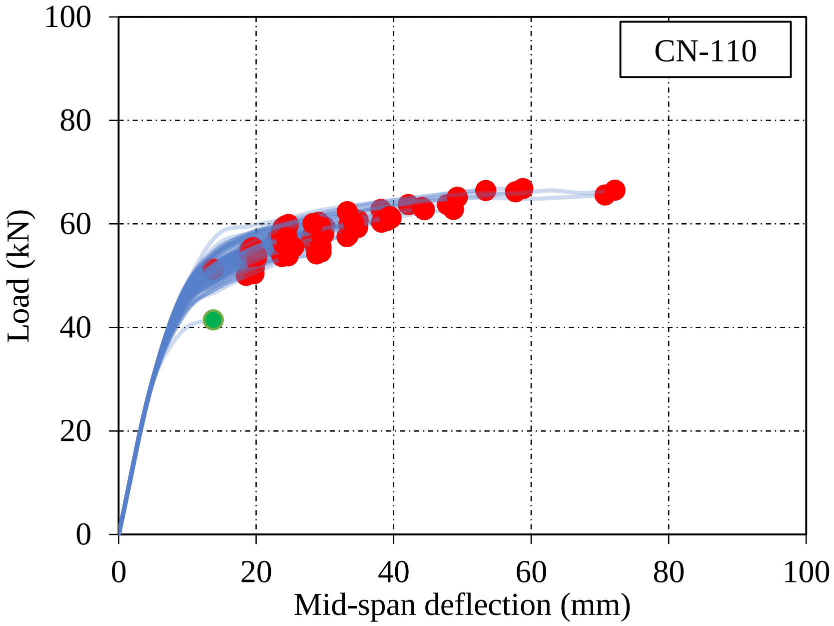

Figure 5.12: Stochastic simulation results of the CN-110 beam

In addition to the reduction of the reinforcing steel cross-sectional area, degradation due to pitting corrosion of the mechanical properties such as the yield strength of the reinforcing bars was implemented in the finite element models by the formulations given in Section 3.4. Scatter plots generated from the outputs of the stochastic simulations, such as the ones shown in Figure 5.13, show a direct relationship between the failure load and the maximum pitting factor of each simulation. In the same manner, a direct dependency exists between the mid-span deflection at failure and the maximum pitting factor. The response of the CN-310 beam was significantly different from the other beams mainly because it was governed by rupture of the tension reinforcement. For this beam the ultimate strain of almost every corroded truss element was reduced by 70 percent. An average cross-sectional loss of 50 percent was also calculated. As a result, the failure load was reduced from 55.0 kN (the average of uniform corrosion simulations) to 5.3 kN, showing the devastating effect of pitting corrosion. Although such a reduction might be purely hypothetical, it clearly demonstrates the important areas of study for stochastic finite element modelling of pitting corrosion. The point shown in green colour in Figure 5.12 shows the possibility of a mid-span deflection less than 20 mm for a beam that can deform up to 72 mm at mid-span under a different pitting corrosion scenario. The failure in such a case, depicted in Figure 5.14, is governed by pitting factors much greater than the average pitting factor in the areas shown. Assuming that a minimum mid-span deflection of 20 mm is defined as a limit state, the stochastic analysis undertaken in this study shows a 13% probability of failure to meet such condition after 110 days of corrosion.

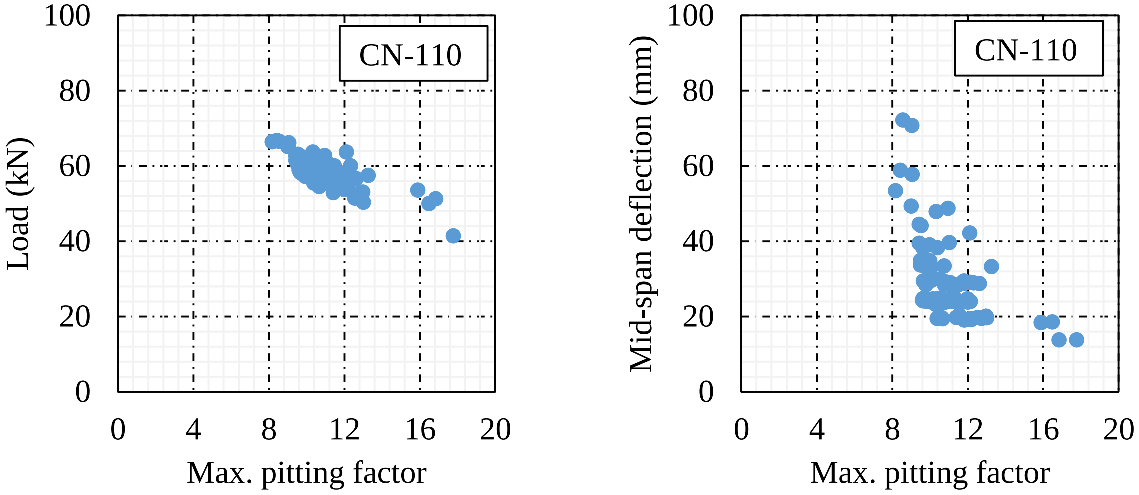

Figure 5.13: Scatter plots of maximum pitting factor, failure load and mid-span deflection at failure of the CN-110 beam

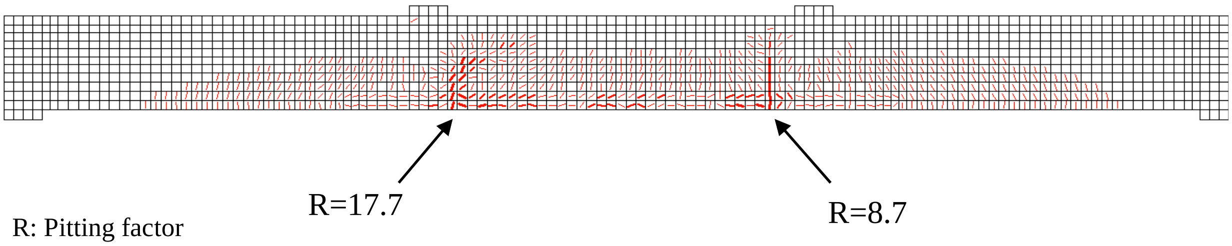

Figure 5.14: Failure of the simulation with largest pitting factors

6 Conclusions and Recommendations

6.1 Summary

This chapter presents conclusions and recommendations for future work based on the research undertaken. The main goal of this thesis was to incorporate the corrosion damage models found in the literature into the NLFEA program VecTor2 to model the response of corroded RC structures. The potential stochastic capabilities of this program were also investigated by stochastic modelling of corroded RC beams. In the process, the following objectives were addressed:

1. Implementing of numerical models which define the corrosion damage in terms of loss of steel reinforcement cross-sectional area, bond strength reduction, and cracking of the cover concrete.
2. Verifying of the implemented models and the analytical procedure employed for incorporating such models into the algorithms of VecTor2.
3. Modelling corrosion-damaged reinforced concrete beams subjected to short-term monotonic nodal displacement with variations in material and specimen configurations.
4. Identifying deficiencies pertaining to the existing corrosion damage models in the literature.
5. Demonstrating the effect of stochastic modelling of RC beams subjected to uniform and pitting corrosion on the response quantities such as failure load or mid-span deflection at failure.

6.2 Conclusions

Based on the results obtained from the deterministic and stochastic modelling of corroded RC beams, the following conclusions and observations were made:

1. With the load-deflection responses presented in Chapter 4, it is confirmed that VecTor2 is capable of modelling the response of corroded RC members with reasonable accuracy.
2. The most decisive factor in degradation of the strength of a RC beam due to corrosion is the corrosion rate (or the reduction of steel reinforcement cross-sectional area).
3. The degree to which the bond strength of a corroded reinforcing bar is reduced is the next dominant parameter as the failure of the modelled beams was accompanied with significant slip in every case.

4. From an ultimate limit state point of view, cracking of the cover concrete is the least important phenomenon associated with corrosion. However, for a serviceability limit state, it should be regarded as the most important as significant cracking can occur in an early stage of corrosion.
5. The Distributed Stress Field Model provides a convenient and accurate framework for incorporating the corrosion induced strains into FE modelling of reinforced concrete.
6. The statistics of the response quantities of RC beams damaged by uniform corrosion are accurately estimated by modelling the rate of corrosion as a single random variable rather than a random field. In other words, consideration of the spatial variability of the rate of corrosion does not lead to a significantly different response.
7. Reduction in the strength of a corroded beam is much more severe in the case of pitting corrosion compared to the uniform corrosion.
8. For the beams subjected to pitting corrosion, the flexural strength is highly sensitive to the maximum pitting factor along the length.

6.3 Recommendations

Future work pertaining to the deficiencies identified during the analytical study of corrosion damage models are outlined. The recommendations are thought to provide improvements on both stochastic and deterministic FE modelling of corroded reinforced concrete beams.

1. The discrepancy between the applied and achieved corrosion current density (or corrosion rate) in accelerated corrosion tests needs to be further studied. Such inaccuracy in the primary input parameter of corrosion damage models can propagate through the analysis and lead to significant error in the results.
2. Further work must be undertaken to investigate the type of rust produced as a result of steel corrosion under different environmental conditions as the corrosion induced tensile strains in the cover concrete and the time to cover cracking are severely affected by the assumed type of rust.
3. The portion of the rust that penetrates into the diffusion zone and the cracks of cover concrete, which does not contribute to further cracking of the cover concrete, needs to be identified precisely.

4. Experimental evidence, found in the literature and presented in previous sections, suggests that both uniform and pitting corrosion occur at the same time. Thus, it is of interest to develop a hybrid corrosion model which combines the effects of simultaneous pitting and uniform corrosion. Such a model can potentially generate a more realistic representation of the corrosion pattern of a reinforcing bar.
5. The development of a bond model applicable to corroded reinforcing bars of various diameters would help in better modelling the response of corroded RC beams which are typically susceptible to bond slip due to cracking of the cover concrete and loss of confinement.
6. The loss of strength and ductility of reinforcing bars due pitting corrosion is a matter which needs to be quantified more precisely.
7. The effects of steel corrosion on the constitutive behaviour of the concrete around a corroded rebar has not been sufficiently studied yet or, at least, cannot be found easily in the literature.
8. A statistical distribution, quantifying the probability of occurrence of pitting corrosion at a certain location along the length of a reinforcing bar, would be a valuable asset to stochastic modelling of corrosion. The assumption of a pit formed over every corroded truss element, made in the analysis performed in this thesis, is not realistic and should be regarded as the worst case scenario.
9. Post-processing of the stochastic simulation results, which has been done by using external scripts written in MATLAB, is an exhaustive task. A post-processor such as Augustus, capable of reporting statistical information about response quantities such as the failure load, in a general sense, or the principal stresses and strains of a certain group of elements, for a detailed investigation, can reveal interesting relationships between input and output parameters which might not be easily noticeable.

References

Abosrra, L., Ashour, A. F., & Youseffi, M. (2011). Corrosion of steel reinforcement in concrete of different compressive strengths. *Constructioin and Building Materials, 25*, 3915-3925.

Almusallam, A. A., Al-Gahtani, A. S., Aziz, A. R., & Rasheeduzzafar. (1996). Effect of reinforcement corrosion on bond strength. *Construction and Building Materials, 10*(2), 123-129.

Alonso, C., Andrade, C., & Gonzalez, J. A. (1988). Relation between resistivity and corrosion rate of reinforcements in carbonated mortar made with several cement types. *Cement and Concrete Research, 18*(5), 687-698.

Alonso, C., Andrade, C., R. J., & Diez, J. (1998). Factors controlling cracking of concrete affected by reinforcement corrosion. *Materials and Structures, 31*, 435-441.

Al-Sulaimani, G., Kaleemullah, M., Basunbul, I., & Rasheeduzafar. (1990). Influence of corrosion and cracking on bond behavior and strength of reinforced concrete members. *ACI Structural Journal, 87*(2), 220-231.

Andrade, C. (2009). Types of models of service life of reinforcement: the case of the resistivity. *Proceedings of the 7th Asia Pacific Structural Engineering and Construction (APSEC) Conference*.

Andrade, C. A. (1993). Cover cracking as a function of bar corrosion: Part I-Experimental test. *Materials and Structures, 26*, 453-464.

Angst, U. (2011). Chloride induced reinforcement corrosion in concrete: Concept of critical chloride content - methods and mechanisms. (Doctoral Thesis). Norwegian University of Science and Technology.

Angst, U., Elsener, B., Jamali, A., & Adey, B. (2012). Concrete cover cracking owing to reinforcement corrosion - theoretical considerations and practical experience. *Materials and Corrosion, 63*(12), 1069-1076.

Apostolopoulos, C. A., Demis, S., & Papadakis, V. G. (2013). Chloride-induced corrosion of steel reinforcement - Mechanical performance and pit depth analysis. *Construction and Building Materials, 38,* 139-146.

Austin, S. A., Lyons, R., & Ing, M. J. (2004). Electrochemical behavior of steel-reinforced concrete during accelerated corrosion testing. *CORROSION Journal, 60*(2), 203-212.

Azad, A. K., Ahmad, S., & Azher, S. A. (2007). Residual Strength of Corrosion-Damaged Reinforced Concrete Beams. *ACI Material Journal, 104*(1), 41-47.

Bazant, Z. O. (1983). Crack band theory for fracture of concrete. *Materials and Structures, 16*, 155-177.

Bhargava, K., Ghosh, A. K., Mori, Y., & Ramanujam, S. (2005). Modeling of time to corrosion-induced cover cracking in reinforced concrete structures. *Cement and Concrete Research, 35*, 2203-2218.

Bhargava, K., Ghosh, A. K., Mori, Y., & Ramanujam, S. (2007). Corrosion-induced bond strength degradation in reinforced concrete - Analytical and empirical models. *Nuclear Engineering and Design, 237*, 1140-1157.

Bohni, H. (2005). Corrosion in reinforced concrete structures. Woodhead publishing.

Broomfield, J. P. (2007). Corrosion of Steel in Concrete.

Cairns, J., Plizzari, G., Du, Y., Law, D., & Franzoni, C. (2005). Mechanical properties of corrosion-damaged reinforcement. *ACI Material Journal, 102*(4), 256-264.

CEB-FIP. (2000). Bond of reinforcement in concrete. State-of-the-art report.

Coronelli, D., & Gambarova, P. (2004). Structural assessment of corroded reinforced concrete beams: Modeling guidelines. *Journal of Structural Engineering, 130*(8), 1214-1224.

Darmawan, M. S. (2007). Spatial time-dependent reliability analysis of corroding pretensioned prestressed concrete bridge girders. *Structural Safety, 29*, 16-31.

Du, Y., Clark, L. A., & Chan, A. H. (2007). Impact of reinforcement corrosion on ductile behavior of reinforced concrete beams. *ACI Structural Journal, 104*(3), 285-293.

FHWA-RD-98-088. (1998). Corrosion protection:Concrete bridges.

fib Bulletin No. 10. (2000). Bond of reinforcement in concrete.

Gonzalez, J., Andrade, C., Alonso, C., & Feliu, S. (1995). Comparison of rates of general corrosion and maximum pitting depth penetration on concrete embedded steel reinforcement. *Cement and Concrete Research, 25*(2), 257-264.

Hilsdorf, H. B. (1991). Code-type formulation of fracture mechanics concepts for concrete. *International Journal of Fracture, 51*(1), 61-72.

Hunter, M. D. (2016). Towards stochastic finite element analysis of reinforced concrete structures. (Master Thesis). University of Toronto.

Jamali, A., Angst, U., Adey, B., & Elsener, B. (2013). Modeling of corrosion-induced concrete cover cracking: A critical analysis. *Construction and Building Materials*, 225–237.

Kallias, A. N., & Rafiq, M. I. (2010). Finite element investigation of the structural response of corroded RC beams. *Engineering Structures, 32*, 2984-2994.

Krajewski, W. F. (1986). Estimation of the covariance and semivariogram for stationary, isotropic random fields. *Integrated design of hydrological networks (Proceedings of the Budapest symposium), 158*, 71-84.

Liou, J., Su, Y., Chiang, J., & Cheng, K. (2011). Gamma random field simulation by a covariance matrix transformation method. *Stochastic environmental research and risk assessment, 25*, 235-251.

Liu, T., & Weyers, R. W. (1998). Modeling the dynamic corrosion process in chloride contaminated concrete structures. *Cement and Concrete Research, 28*(3), 365-379.

Liu, Y., & Weyers, R. (1998). Modeling the time-to-corrosion cracking in chloride contaminated reinforced concrete structures. *ACI Material Journal, 95*(6), 675-681.

Lu, Z. H., Yu, K., & Zhao, Y. (2008). Stochastic modeling of corrosion propagation for service life prediction of chloride contaminated RC structures. *Proceedings of the International Symposium on Life-Cycle Civil Engineering, IALCCE '08, held in Varenna, Lake Como, Italy*, 195-201.

Maaddawy, T., & Soudki, K. (2003). Effectiveness of impressed current techniques to simulate corrosion of steel reinforcement in concrete. *Journal of Materials in Civil Engineering, 15*(1), 41-47.

Maaddawy, T., Soudki, K., & Topper, T. (2005). Analytical Model to Predict Nonlinear Flexural Behavior of Corroded Reinforced Concrete Beams. *ACI Structural Journal, 102*(4), 550-559.

Maaddawy, T., Soudki, K., & Topper, T. (2005). Long-term performance of corrosion-damaged reinforced concrete beams. *ACI Structural Journal, 102*(5), 649-656.

Markeset, G., & Myrdal, R. (2008). Modelling of reinforcement in concrete - State of the art. COIN Project report 7.

Otieno, M., Beushausen, H., & Alexander, M. (2011). Prediction of corrosion rate in RC structures - A critical review. *Modeling of Corroding Concrete Structures, 3*, 3-37.

Pantazopoulou, S. J., & Papoulia, K. D. (2001). Modeling cover-cracking due to reinforcement corrosion in RC structures. *Journal of Engineering Mechanics, 127*(4), 342-351.

Richard, B., Ragueneau, F., Cremona, C., Adelaide, L., & Tailhan, J. L. (2010). A three-dimensional steel/concrete interface model including corrosion effects. *Engineering Fracture Mechanics, 77*, 951-973.

Rodriguez, J., Ortega, M., & Casal, J. (1997). Load carrying capacity of concrete structures with corroded reinforcement. *Construction and Building Materials, 11*(4), 239-248.

Stewart, M. G., & Al-Harthy, A. (2008). Pitting corrosion and structural reliability of corroding RC structures: Experimental data and probabilistic analysis. *Reliability Engineering and System Safety, 93*, 373-382.

Sudret, B., & Der Kiureghian, A. (2000). Stochastic Finite Element Methods and Reliability, A State-of-the-Art Report.

Tuutti, K. (1982). Corrosion of steel in concrete. *Swedish cement and concrete research institute*.

Vecchio, F. J. (2000). Distributed Stress Field Model for Reinforced Concrete Formulation. *ASCE Journal of Structural Engineering, 126*(9), 1071-1077.

Vecchio, F. J., & Collins, M. (1986). The modified compression field theory for reinforced concrete elements subjected to shear. *ACI Journal, 83*(22), 219-231.

Vu, K., & Stewart, M. G. (2000). Structural reliability of concrete bridges including improved chloride-induced corrosion models. *Structural Safety, 22,* 313-333.

Vu, K., Stewart, M. G., & Mullard, J. (2005). Corrosion-induced cracking: Experimental data and predictive models. *ACI Structural Journal, 102*(5), 719-726.

Wang, L., Ma, Y., Ding, W., Jianren, Z., & Liu, Y. (2015). Comparative study of flexural behavior of corroded beams with different types of steel bars. *Journal of Performance of Constructed Facilities, 29*(6), 1-9.

Wang, X. H., & Liu, X. L. (2004). Modelling effects of corrosion on cover cracking and bond in reinforced concrete. *Magazine of Concrete Research, 56*(4), 191-199.

Wong, P., Trommels, H., & Vecchio, F. J. (2013). VecTor2 and FormWorks user's manual.

Yalcyn, H., & Ergun, M. (1996). The prediction of corrosion rates of reinforcing steels in concrete. *Cement and Concrete Research, 26*(10), 1593-1599.

Yu, L., Francois, R., Dang, V., L'Hostis, V., & Gagne, R. (2015). Distribution of corrosion and pitting factor of steel in corroded RC beams. *Construction and Building Materials, 95,* 384-392.

Zhang, R., Castel, A., & Francois, R. (2010). Concrete cover cracking with reinforcement corrosion of RC beam during chloride-induced corrosion process. *Cement and Concrete Research, 40,* 415-425.

Appendix A: Experimental Data

The following appendix contains all the data extracted from Yu et al. (2015).

Beam	Bs02		Bs03		Bs04	
Bar	Front	Back	Front	Back	Front	Back
X (mm)	Section loss (%)					
5	4.4	4.0	5.4	3.7	2.6	1.8
15	4.4	4.0	5.4	3.7	2.6	1.8
25	4.4	4.0	5.4	3.7	2.6	1.8
35	4.4	4.0	3.0	3.7	7.9	1.8
45	4.4	4.0	3.0	3.7	7.9	3.0
55	4.4	4.0	3.0	3.7	7.9	3.0
65	5.3	8.0	3.0	3.7	7.9	3.0
75	5.3	8.0	3.0	3.7	7.9	3.0
85	4.7	8.0	3.0	3.7	7.9	3.0
95	4.7	8.0	3.0	3.7	7.9	3.0
105	4.7	7.4	3.0	3.5	10.6	3.0
115	4.7	7.4	3.3	3.5	10.6	3.0
125	7.2	7.4	3.3	3.5	10.6	3.0
135	7.2	7.4	3.3	3.5	10.6	3.0
145	7.2	7.4	3.3	3.5	10.6	3.0
155	7.2	7.4	2.1	3.5	10.6	3.0
165	7.2	4.9	2.1	3.5	10.6	3.0
175	7.2	4.9	2.1	4.0	10.6	3.0
185	7.2	4.9	1.7	4.0	10.6	3.0
195	7.2	1.4	1.7	4.0	5.3	3.0
205	5.8	1.4	1.7	4.0	5.3	3.0
215	5.8	1.4	1.7	3.8	5.3	3.0
225	5.8	1.4	3.0	3.8	5.3	3.0
235	5.8	2.0	3.0	7.1	4.1	3.0
245	5.8	2.0	3.0	7.1	4.1	3.0
255	5.8	2.0	3.0	7.1	6.8	3.0
265	9.7	2.0	3.0	7.1	6.8	3.0
275	9.7	2.0	3.0	3.5	6.8	3.0
285	9.7	2.0	3.0	3.5	6.8	3.0
295	9.7	2.0	3.0	3.5	5.0	3.0
305	6.4	2.0	3.0	3.5	5.0	3.0
315	6.4	2.0	3.0	3.5	5.0	3.0
325	6.4	2.0	3.0	3.5	5.0	3.0
335	6.4	2.0	3.0	3.5	2.4	4.8

Beam	Bs02		Bs03		Bs04	
Bar	Front	Back	Front	Back	Front	Back
X (mm)	Section loss (%)					
345	6.4	2.0	3.0	3.5	2.4	4.8
355	6.4	2.6	3.0	3.5	2.4	4.8
365	8.1	2.6	3.0	3.5	2.4	4.8
375	8.1	2.6	3.0	3.5	2.4	4.8
385	8.1	2.6	3.0	3.5	2.4	4.8
395	3.3	2.6	3.0	3.5	2.4	4.8
405	3.3	2.6	3.0	3.5	2.4	4.8
415	3.3	2.6	3.0	3.5	2.4	4.8
425	3.3	2.6	3.0	3.5	2.4	4.8
435	3.3	2.6	3.0	6.0	2.4	4.8
445	3.3	2.6	4.4	6.0	2.4	4.8
455	3.3	2.6	4.4	6.0	2.4	4.8
465	3.3	2.6	4.4	17.2	2.4	4.8
475	3.3	2.6	4.4	17.2	2.4	10.0
485	3.3	2.6	6.0	17.2	2.4	10.0
495	3.3	2.6	6.0	17.2	2.4	10.0
505	8.9	2.6	6.0	17.2	8.5	10.0
515	8.9	2.6	6.0	6.8	8.5	10.0
525	8.9	2.6	6.0	6.8	8.5	10.0
535	8.9	2.6	6.0	6.8	8.5	16.7
545	8.9	2.6	16.4	6.8	8.5	16.7
555	8.9	2.6	16.4	6.8	36.5	16.7
565	8.9	2.6	16.4	6.8	3.5	16.7
575	8.9	2.6	16.4	9.2	3.5	9.4
585	6.7	2.6	16.4	9.2	3.5	9.4
595	6.7	2.6	6.7	9.2	3.5	9.4
605	6.7	6.0	6.7	9.2	3.5	9.4
615	6.7	6.0	6.7	16.0	5.3	9.4
625	6.7	6.0	6.7	16.0	5.3	9.4
635	6.7	6.0	6.7	16.0	5.3	9.4
645	5.0	4.3	6.7	16.0	5.3	9.4
655	5.0	4.3	6.7	16.0	4.4	9.4
665	5.0	4.3	6.7	16.0	4.4	9.4
675	5.0	4.3	6.7	16.0	4.4	9.4
685	5.0	4.3	6.7	12.5	4.4	9.4
695	5.0	4.3	6.7	12.5	4.4	9.4
705	5.0	4.3	6.7	12.5	4.4	9.4
715	5.0	4.3	6.7	12.5	6.5	9.4

Beam	Bs02		Bs03		Bs04	
Bar	Front	Back	Front	Back	Front	Back
X (mm)	Section loss (%)					
725	5.0	4.3	6.7	12.5	6.5	9.4
735	11.9	2.9	6.7	8.3	6.5	9.4
745	11.9	2.9	6.7	8.3	6.5	9.4
755	11.9	2.9	6.7	8.3	6.5	9.4
765	11.9	2.9	6.7	8.3	3.5	9.4
775	14.7	2.9	6.7	5.8	3.5	9.4
785	14.7	2.9	11.9	5.8	3.5	9.4
795	14.7	2.9	11.9	5.8	3.5	28.0
805	5.3	2.9	11.9	6.2	3.5	28.0
815	5.3	2.9	11.9	6.2	3.5	4.2
825	5.3	2.9	11.9	6.2	3.5	4.2
835	8.1	2.6	7.1	6.2	3.5	4.2
845	8.1	2.6	7.1	6.2	3.5	4.2
855	8.1	2.6	7.1	6.2	3.5	4.2
865	10.0	2.6	7.1	8.6	3.5	4.2
875	10.0	2.6	7.1	8.6	3.5	4.2
885	10.0	2.6	7.1	8.6	2.9	4.2
895	10.0	2.6	7.1	8.6	2.9	4.2
905	10.0	2.6	7.1	8.6	2.9	12.1
915	8.3	2.6	3.7	8.6	2.9	12.1
925	8.3	2.6	3.7	8.6	9.1	12.1
935	8.3	2.6	3.7	4.2	9.1	12.1
945	8.3	2.6	3.7	4.2	9.1	3.9
955	8.3	2.6	3.7	4.2	9.1	3.9
965	8.3	2.6	3.7	4.2	9.1	3.9
975	8.9	2.6	3.7	4.2	6.8	10.3
985	8.9	2.6	4.0	4.2	6.8	10.3
995	8.9	2.6	4.0	4.8	6.8	10.3
1005	8.9	2.3	4.0	4.8	22.9	10.3
1015	8.9	2.3	4.0	4.8	22.9	10.3
1025	8.9	2.3	4.0	4.8	10.0	10.3
1035	8.9	2.3	4.0	4.8	10.0	10.3
1045	8.9	2.3	4.0	4.8	10.0	10.3
1055	8.9	2.3	4.0	4.8	10.0	10.3
1065	10.0	2.3	4.0	4.3	10.0	7.6
1075	10.0	2.3	4.0	4.3	7.6	7.6
1085	10.0	2.3	4.0	3.4	4.7	7.6
1095	10.0	2.3	4.0	3.4	4.7	7.6

Beam	Bs02		Bs03		Bs04	
Bar	Front	Back	Front	Back	Front	Back
X (mm)	Section loss (%)					
1105	10.0	2.3	3.7	3.4	4.7	7.6
1115	10.0	2.3	3.7	3.8	7.4	7.6
1125	10.0	2.3	3.7	3.8	7.4	7.6
1135	10.0	2.3	3.7	3.8	7.4	7.6
1145	15.3	2.3	5.9	3.8	7.4	7.6
1155	15.3	2.3	5.9	3.8	7.4	4.8
1165	15.3	2.3	5.9	3.2	7.4	4.8
1175	12.2	2.3	5.9	3.2	7.4	4.8
1185	12.2	2.3	3.1	5.2	8.2	4.8
1195	12.2	2.3	3.1	5.2	8.2	4.8
1205	12.2	2.3	3.1	5.2	8.2	4.8
1215	12.2	10.4	3.3	5.2	8.2	4.8
1225	12.2	10.4	3.3	5.2	8.2	4.8
1235	12.2	10.4	3.3	5.2	8.2	4.8
1245	12.2	3.7	3.3	4.0	8.2	4.8
1255	12.2	3.7	3.3	4.0	8.2	10.6
1265	6.1	3.7	3.3	4.0	8.2	10.6
1275	6.1	3.7	3.3	4.0	8.2	10.6
1285	6.1	3.7	3.3	4.0	4.1	10.6
1295	10.0	3.7	3.3	4.0	4.1	10.6
1305	10.0	3.7	3.3	4.0	4.1	10.6
1315	10.0	3.7	3.3	4.0	11.8	10.6
1325	10.0	3.7	3.4	4.0	11.8	8.8
1335	5.0	5.0	3.4	4.0	4.1	8.8
1345	5.0	5.0	3.4	4.0	10.0	8.8
1355	5.0	5.0	3.4	4.0	10.0	8.2
1365	5.0	5.0	3.4	4.0	10.0	8.2
1375	5.0	5.0	3.4	4.0	10.0	8.2
1385	5.0	6.0	3.4	6.2	10.0	8.2
1395	5.0	6.0	3.4	6.2	10.0	8.2
1405	5.0	6.0	3.4	6.2	10.0	8.2
1415	3.9	34.0	3.4	5.7	10.0	8.2
1425	3.9	34.0	3.4	5.7	10.0	8.2
1435	3.9	9.4	5.3	5.7	11.8	8.5
1445	3.9	9.4	5.3	5.7	11.8	8.5
1455	3.9	9.4	5.3	4.8	11.8	8.5
1465	3.9	9.4	5.3	4.8	11.8	8.5
1475	3.9	9.4	5.3	4.8	14.7	8.5

Beam	Bs02		Bs03		Bs04	
Bar	Front	Back	Front	Back	Front	Back
X (mm)	Section loss (%)					
1485	26.7	9.4	5.3	5.8	14.7	8.5
1495	26.7	9.4	5.9	5.8	14.7	8.5
1505	26.7	12.0	5.9	5.8	14.7	8.5
1515	26.7	12.0	5.9	5.8	8.2	13.3
1525	12.5	12.0	5.9	5.8	8.2	13.3
1535	12.5	9.4	5.9	4.3	39.4	13.3
1545	12.5	9.4	5.9	4.3	39.4	10.9
1555	12.5	9.4	5.9	4.3	39.4	10.9
1565	12.5	9.4	5.0	4.3	12.9	10.9
1575	12.5	9.4	5.0	4.3	12.9	10.9
1585	11.9	9.4	5.0	4.3	12.9	10.9
1595	11.9	3.4	5.0	4.3	12.9	8.5
1605	11.9	3.4	5.0	4.3	11.2	8.5
1615	11.9	3.4	3.3	4.3	11.2	8.5
1625	11.9	3.4	3.3	4.3	11.2	8.5
1635	11.9	2.0	3.3	4.3	11.2	8.5
1645	11.9	2.0	5.1	4.6	11.2	8.5
1655	11.9	2.0	5.1	4.6	11.2	8.5
1665	11.9	2.0	5.1	4.6	11.2	8.5
1675	11.9	2.0	4.6	4.6	8.5	8.5
1685	14.2	2.0	4.6	4.6	8.5	11.2
1695	14.2	2.0	4.6	4.6	8.5	11.2
1705	14.2	2.0	4.6	4.6	8.5	11.2
1715	7.5	2.0	4.6	8.5	8.5	11.2
1725	7.5	5.1	4.6	8.5	8.5	11.2
1735	7.5	5.1	4.6	8.5	2.4	11.2
1745	7.5	5.1	4.6	8.5	2.4	11.2
1755	7.5	5.1	4.6	8.5	11.8	11.2
1765	7.5	5.1	4.6	7.1	11.8	11.2
1775	7.5	5.1	4.6	7.1	6.5	6.1
1785	7.5	5.1	4.6	7.1	6.5	6.1
1795	15.8	5.1	4.6	7.1	6.5	6.1
1805	15.8	5.1	4.6	7.1	6.5	3.0
1815	15.8	5.1	4.6	7.1	6.5	3.0
1825	11.4	5.1	4.6	4.0	6.5	3.0
1835	11.4	4.6	3.9	4.0	3.5	3.0
1845	11.4	4.6	3.9	4.0	3.5	3.0
1855	13.3	4.6	3.9	4.0	3.5	3.0

Beam	Bs02		Bs03		Bs04	
Bar	Front	Back	Front	Back	Front	Back
X (mm)	Section loss (%)					
1865	13.3	4.6	3.9	3.8	3.5	11.2
1875	13.3	4.6	3.9	3.8	3.5	11.2
1885	10.0	4.6	3.9	3.8	3.5	5.2
1895	10.0	8.0	5.7	3.8	3.5	5.2
1905	10.0	8.0	5.7	3.8	3.5	5.2
1915	10.0	8.0	6.9	3.8	3.5	5.2
1925	10.0	8.0	6.9	3.8	3.5	5.2
1935	10.0	8.0	6.9	3.8	3.5	5.2
1945	5.6	8.0	6.3	3.8	3.5	5.2
1955	5.6	8.0	6.3	3.4	29.1	5.2
1965	5.6	8.0	6.3	3.4	29.1	2.4
1975	5.6	8.0	6.6	3.4	29.1	10.0
1985	5.6	8.0	6.6	3.4	13.2	10.0
1995	5.6	8.0	6.6	3.4	13.2	10.0
2005	5.6	8.0	6.6	3.4	2.9	10.0
2015	5.6	8.0	6.6	3.4	2.9	3.3
2025	5.6	5.1	6.6	3.4	2.9	3.3
2035	5.6	5.1	6.6	6.2	2.9	3.3
2045	5.6	5.1	9.0	6.2	2.9	3.3
2055	5.6	5.1	9.0	6.2	2.9	3.3
2065	5.6	5.1	9.0	6.2	2.9	3.3
2075	5.6	5.1	9.0	6.2	2.9	3.3
2085	5.6	3.1	13.1	6.2	2.9	3.3
2095	5.6	3.1	13.1	8.5	2.9	3.3
2105	5.6	3.1	13.1	8.5	2.9	3.3
2115	5.6	3.1	13.1	8.5	2.9	3.3
2125	5.6	3.1	13.1	7.8	7.6	3.3
2135	5.6	3.1	7.1	7.8	7.6	3.3
2145	6.1	3.1	7.1	7.8	7.6	9.1
2155	6.1	3.1	7.1	7.8	7.6	9.1
2165	6.1	3.1	7.1	7.8	1.8	9.1
2175	4.2	3.1	7.1	7.8	1.8	9.1
2185	4.2	3.1	7.1	7.5	15.6	9.1
2195	4.2	2.0	9.3	7.5	34.7	10.9
2205	4.2	2.0	9.3	7.5	34.7	10.9
2215	4.2	2.0	9.3	7.5	12.9	10.9
2225	4.2	2.0	9.3	7.5	12.9	10.9
2235	3.6	2.0	9.9	7.5	12.9	10.9

Beam	Bs02		Bs03		Bs04	
Bar	Front	Back	Front	Back	Front	Back
X (mm)	Section loss (%)					
2245	3.6	2.0	9.9	7.5	12.9	10.9
2255	3.6	4.0	9.9	7.2	7.1	10.9
2265	3.6	4.0	9.9	7.2	7.1	8.2
2275	3.6	4.0	9.6	7.2	7.1	8.2
2285	3.6	4.0	9.6	7.2	7.6	8.2
2295	3.6	4.0	9.6	7.2	6.5	8.2
2305	3.6	4.0	9.6	8.3	6.5	8.2
2315	3.6	4.0	9.6	8.3	6.5	10.9
2325	3.6	4.0	9.6	8.3	6.5	10.9
2335	2.5	4.0	9.6	8.3	6.5	10.9
2345	2.5	4.0	9.6	8.3	6.5	10.9
2355	2.5	4.0	8.4	5.1	6.5	10.9
2365	1.9	4.0	8.4	5.1	6.5	10.9
2375	1.9	4.0	8.4	5.1	6.5	10.9
2385	1.9	4.0	8.4	5.1	6.5	10.9
2395	1.9	4.0	8.4	5.1	6.5	8.8
2405	1.9	4.0	8.4	5.1	6.5	8.8
2415	1.9	4.0	8.4	9.1	17.9	8.8
2425	1.9	4.0	8.4	9.1	17.9	8.8
2435	1.9	4.0	8.4	9.1	17.9	8.8
2445	1.4	4.0	8.0	9.1	17.9	6.7
2455	1.4	4.0	8.0	9.1	38.8	6.7
2465	1.4	4.0	8.0	9.1	38.8	6.7
2475	1.4	4.0	8.0	9.1	12.1	6.7
2485	1.4	4.0	7.1	9.1	12.1	6.7
2495	1.4	4.0	7.1	9.1	12.1	6.7
2505	1.4	4.0	7.1	6.0	12.1	6.7
2515	1.4	4.0	7.1	6.0	12.1	6.7
2525	1.4	4.0	7.1	6.0	12.1	6.7
2535	1.4	2.6	7.1	6.0	12.1	6.7
2545	1.4	2.6	7.1	6.0	12.1	6.7
2555	1.4	2.6	3.3	6.2	12.1	4.8
2565	5.8	2.6	3.3	6.2	12.1	4.8
2575	5.8	2.6	3.3	6.2	12.1	4.8
2585	5.8	2.6	3.3	6.2	12.1	4.8
2595	5.8	2.6	3.3	7.7	12.1	4.8
2605	5.8	2.6	2.9	7.7	2.9	4.8
2615	6.7	2.6	2.9	7.7	2.9	8.8

Beam	Bs02		Bs03		Bs04	
Bar	Front	Back	Front	Back	Front	Back
X (mm)	Section loss (%)					
2625	6.7	2.6	2.9	7.7	2.9	8.8
2635	6.7	8.6	2.9	6.9	2.9	8.8
2645	6.7	8.6	2.9	6.9	2.9	8.8
2655	10.0	8.6	2.9	6.9	2.9	8.8
2665	10.0	8.6	2.9	6.9	2.9	8.8
2675	10.0	5.4	2.9	6.9	2.9	8.8
2685	10.0	5.4	2.9	5.7	2.9	27.0
2695	10.0	5.4	2.9	5.7	2.9	27.0
2705	13.3	5.4	2.9	4.3	2.9	27.0
2715	13.3	5.4	2.6	4.3	2.9	3.9
2725	13.3	5.4	2.6	4.3	2.9	3.9
2735	4.4	5.4	2.6	4.3	2.9	3.9
2745	4.4	5.4	2.6	4.3	2.9	3.9
2755	4.4	5.4	2.6	4.3	2.9	3.9
2765	4.4	10.0	2.6	4.3	2.9	3.9
2775	4.4	10.0	2.6	7.5	2.9	3.9
2785	4.4	10.0	2.6	7.5	2.9	5.2
2795	4.4	6.3	2.6	6.5	2.9	5.2
2805	4.4	6.3	2.6	6.5	2.9	5.2
2815	4.4	6.3	2.6	6.5	2.1	5.2
2825	4.4	6.3	2.6	6.5	2.1	5.2
2835	4.4	6.3	2.6	6.5	2.1	5.2
2845	4.4	6.3	2.6	5.4	2.1	2.7
2855	3.6	6.3	2.6	5.4	2.1	2.7
2865	3.6	7.7	2.6	5.4	2.1	2.7
2875	3.6	7.7	2.6	5.4	2.1	2.7
2885	3.6	7.7	2.6	6.8	3.5	2.7
2895	3.6	7.7	2.6	6.8	3.5	2.7
2905	3.6	4.9	2.6	6.8	3.5	2.7
2915	3.6	4.9	2.6	6.8	3.5	2.7
2925	4.4	4.9	2.6	3.7	3.5	2.7
2935	4.4	4.9	2.6	3.7	3.5	2.7
2945	4.4	4.9	2.6	3.7	3.5	2.7
2955	4.4	4.9	2.6	3.7	3.5	2.7
2965	4.4	4.9	2.6	3.7	3.5	2.7
2975	4.4	4.9	2.6	3.7	3.5	2.7
2985	4.4	4.9	2.6	3.7	3.5	2.7
2995	4.4	4.9	2.6	3.7	3.5	2.7

Appendix B: Stochastic simulation results

B.1 Stochastic simulations of uniform corrosion

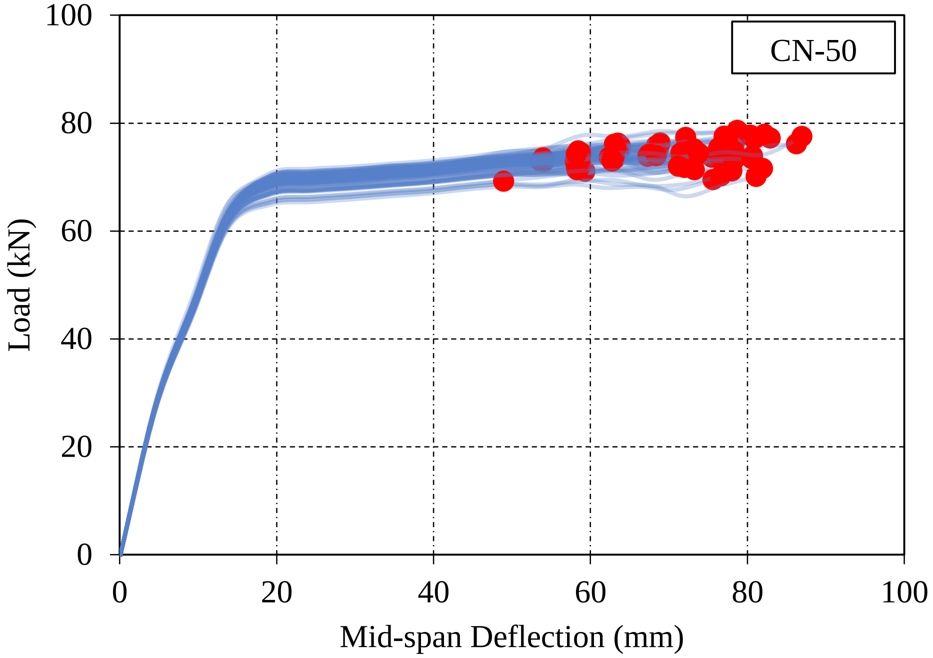

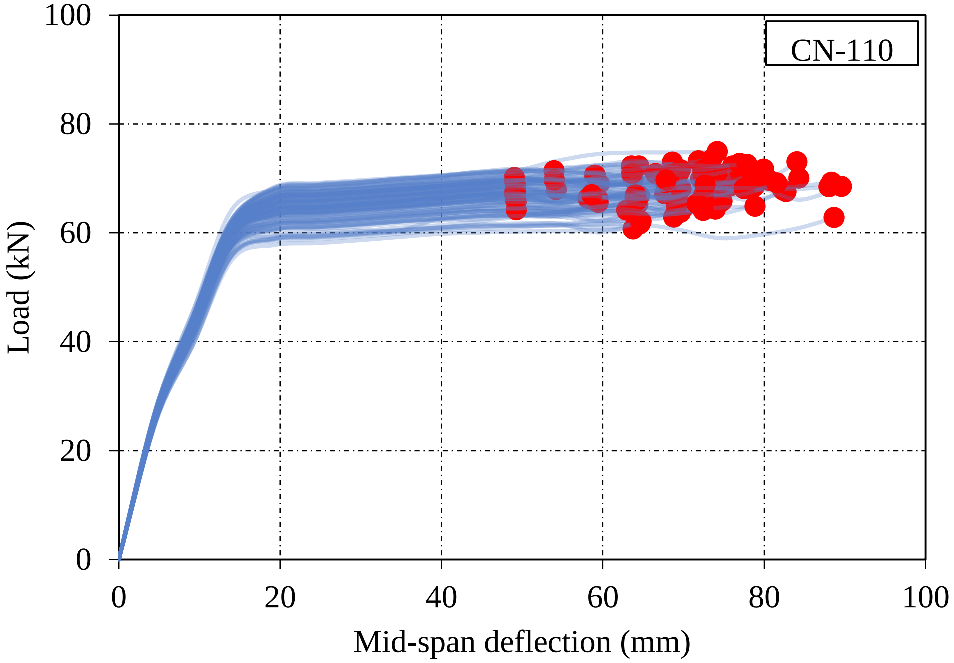

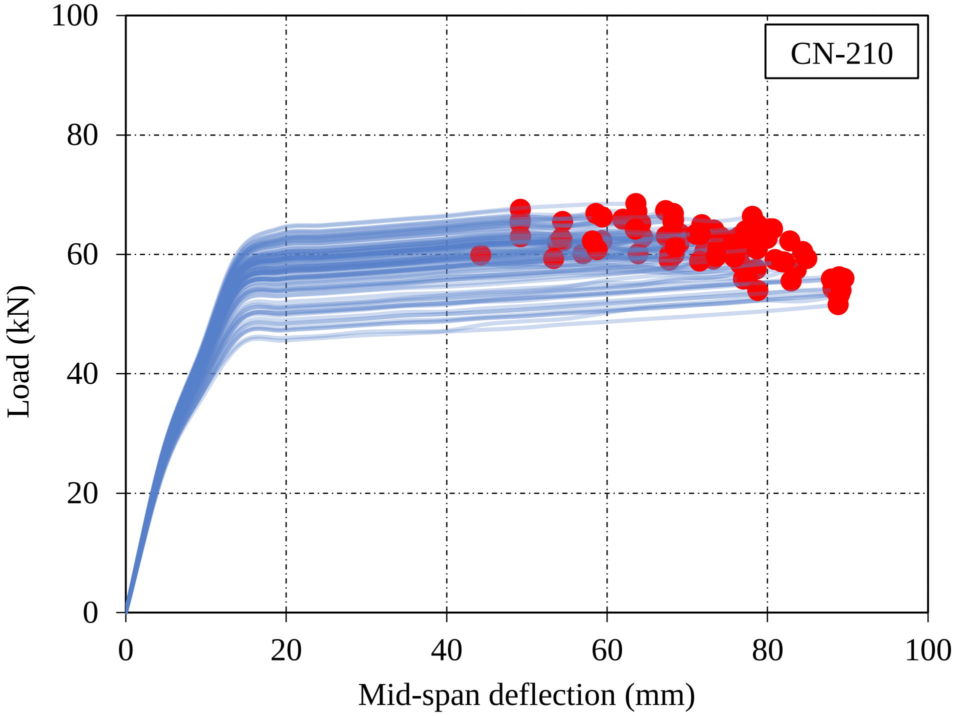
CN-210
Load (kN)
Mid-span deflection (mm)
0
20
40
60
80
100
0
20
40
60
80
100

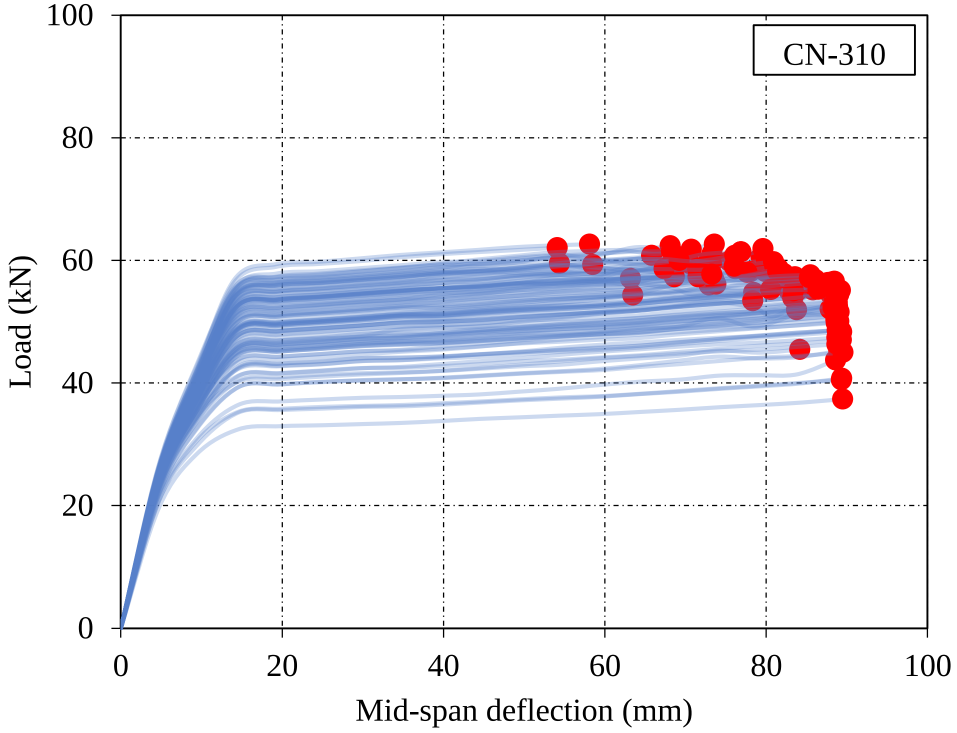
CN-310
Load (kN)
Mid-span deflection (mm)
0
20
40
60
80
100
0
20
40
60
80
100

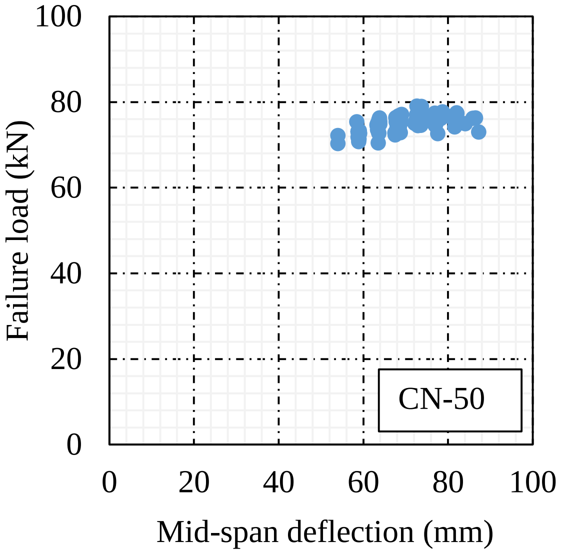
CN-50
Failure load (kN)
0
20
40
60
80
100
Mid-span deflection (mm)
0
20
40
60
80
100

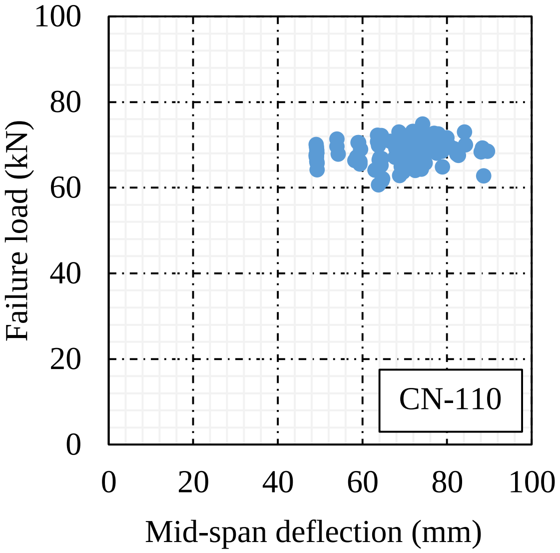
CN-110
Failure load (kN)
0
20
40
60
80
100
Mid-span deflection (mm)
0
20
40
60
80
100

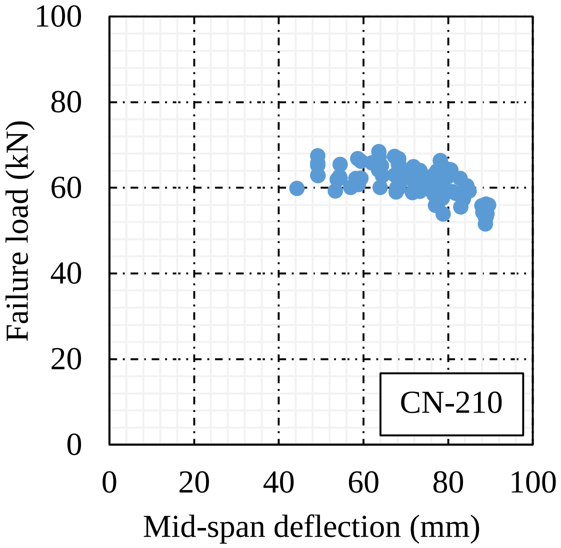
CN-210
Failure load (kN)
0
20
40
60
80
100
Mid-span deflection (mm)
0
20
40
60
80
100

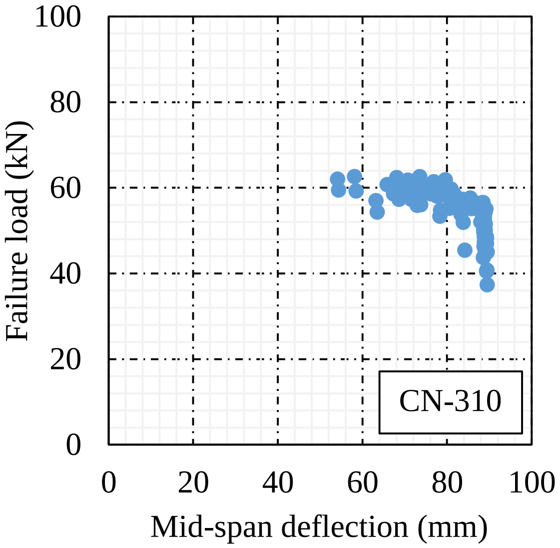
CN-310
Failure load (kN)
0
20
40
60
80
100
Mid-span deflection (mm)
0
20
40
60
80
100

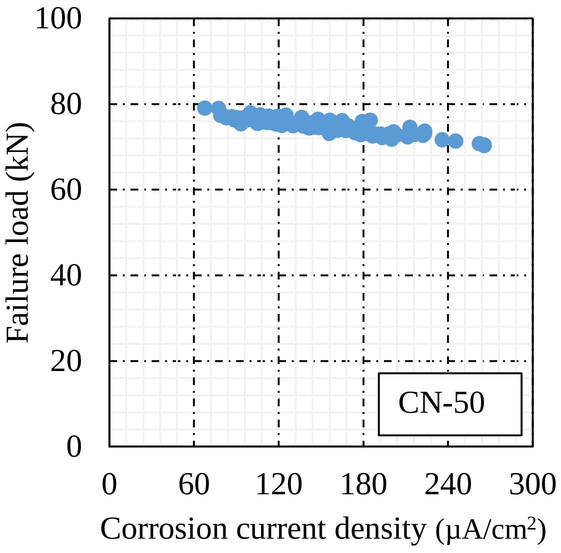
Failure load (kN)
100
80
60
40
20
0
0
60
120
180
240
300
Corrosion current density (μA/cm²)
CN-50

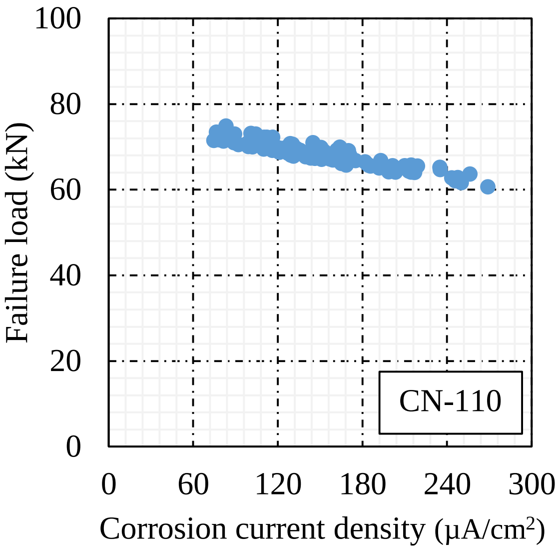
Failure load (kN)
100
80
60
40
20
0
0
60
120
180
240
300
Corrosion current density (μA/cm²)
CN-110

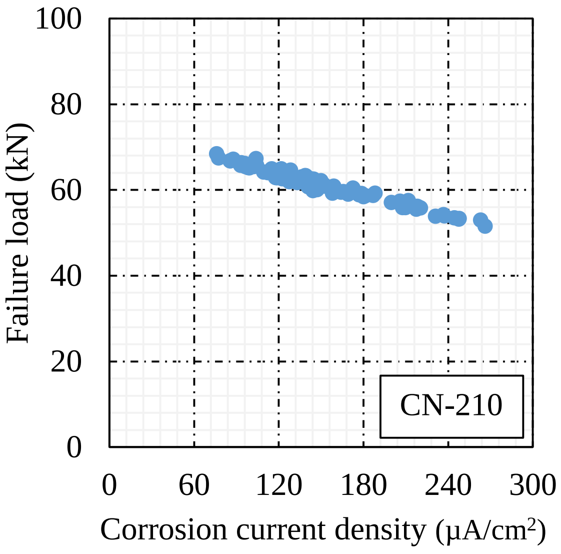
Failure load (kN)
100
80
60
40
20
0
0
60
120
180
240
300
Corrosion current density (μA/cm²)
CN-210

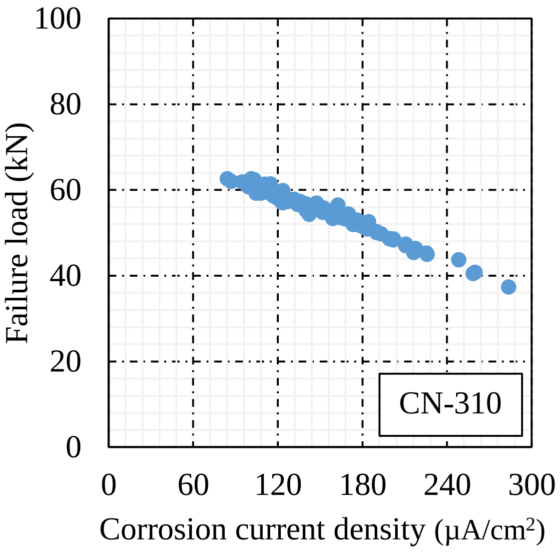
Failure load (kN)
100
80
60
40
20
0
0
60
120
180
240
300
Corrosion current density (μA/cm²)
CN-310

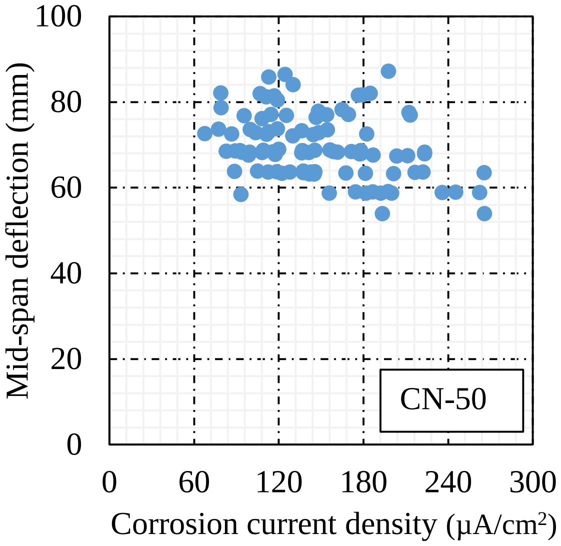
CN-50
Mid-span deflection (mm)
0
20
40
60
80
100
0
60
120
180
240
300
Corrosion current density (μA/cm²)

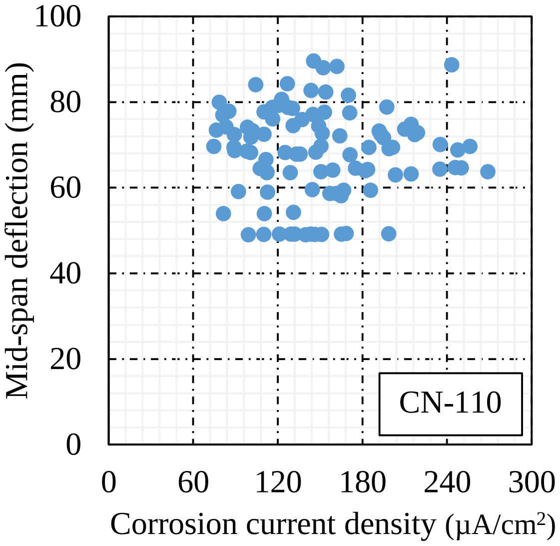
CN-110
Mid-span deflection (mm)
0
20
40
60
80
100
0
60
120
180
240
300
Corrosion current density (μA/cm²)

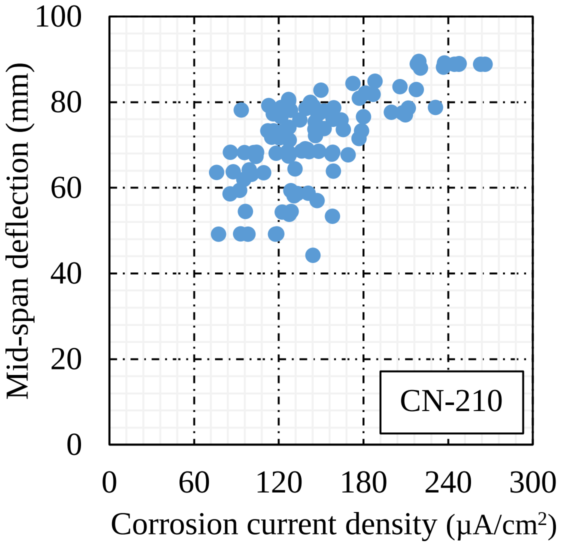
CN-210
Mid-span deflection (mm)
0
20
40
60
80
100
0
60
120
180
240
300
Corrosion current density (μA/cm²)

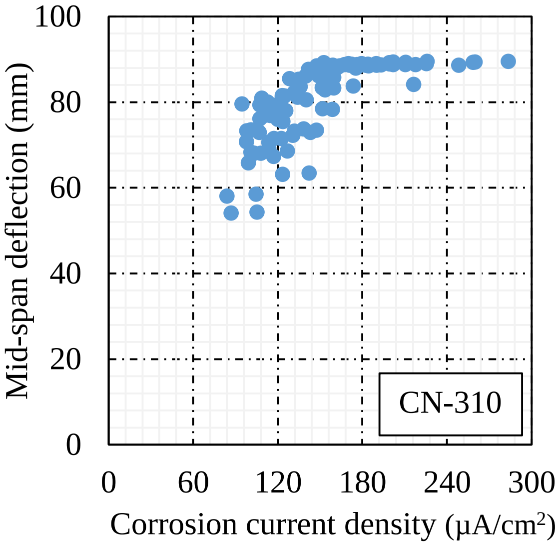
CN-310
Mid-span deflection (mm)
0
20
40
60
80
100
0
60
120
180
240
300
Corrosion current density (μA/cm²)

B.2 Random field simulations of the CN-50 beam

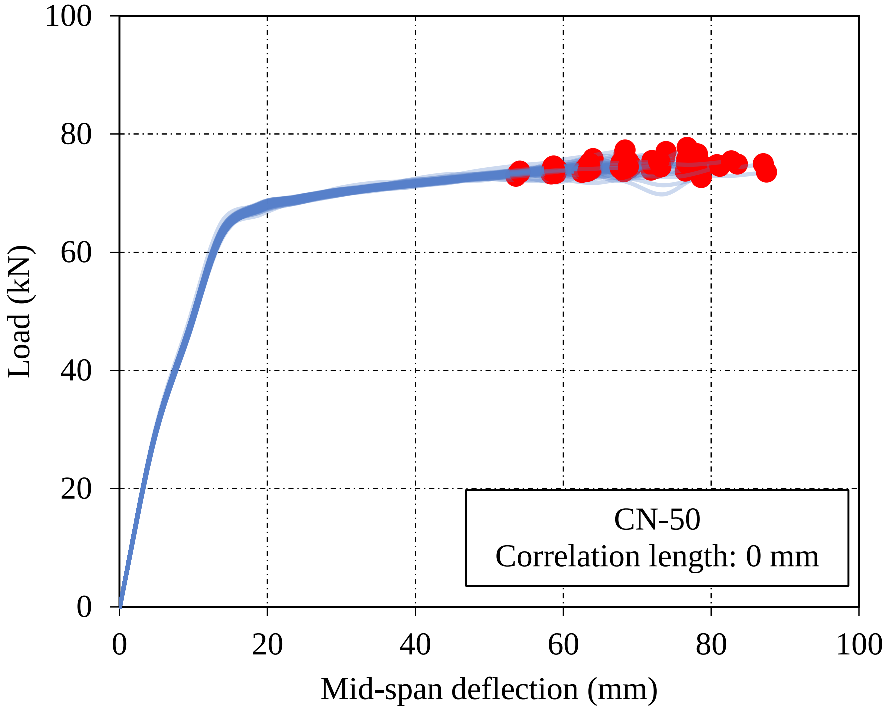

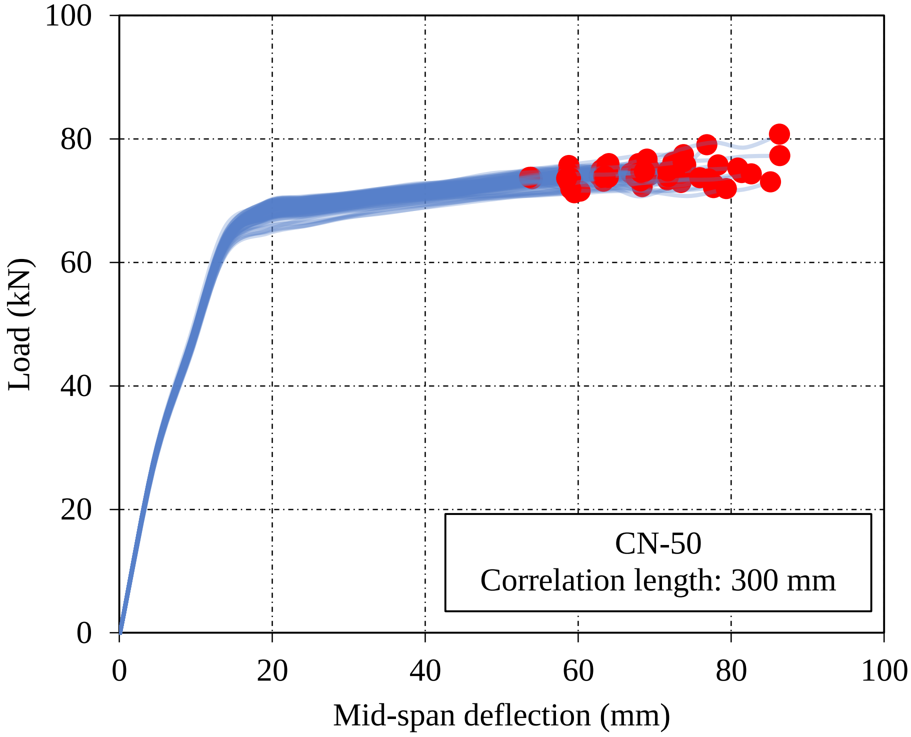

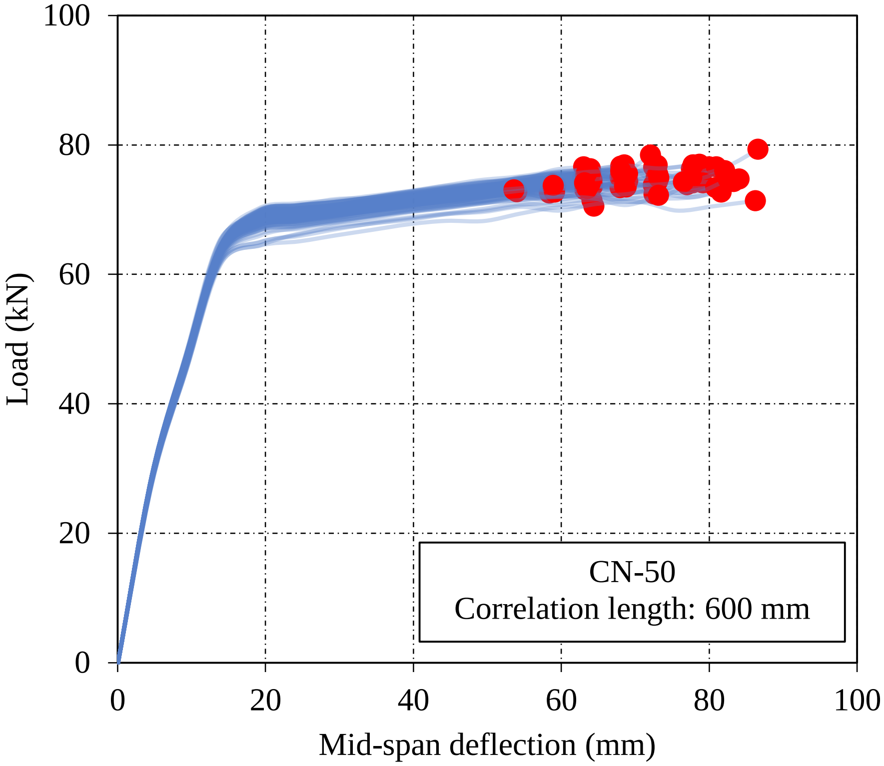
Load (kN)
Mid-span deflection (mm)
0
20
40
60
80
100
CN-50
Correlation length: 600 mm

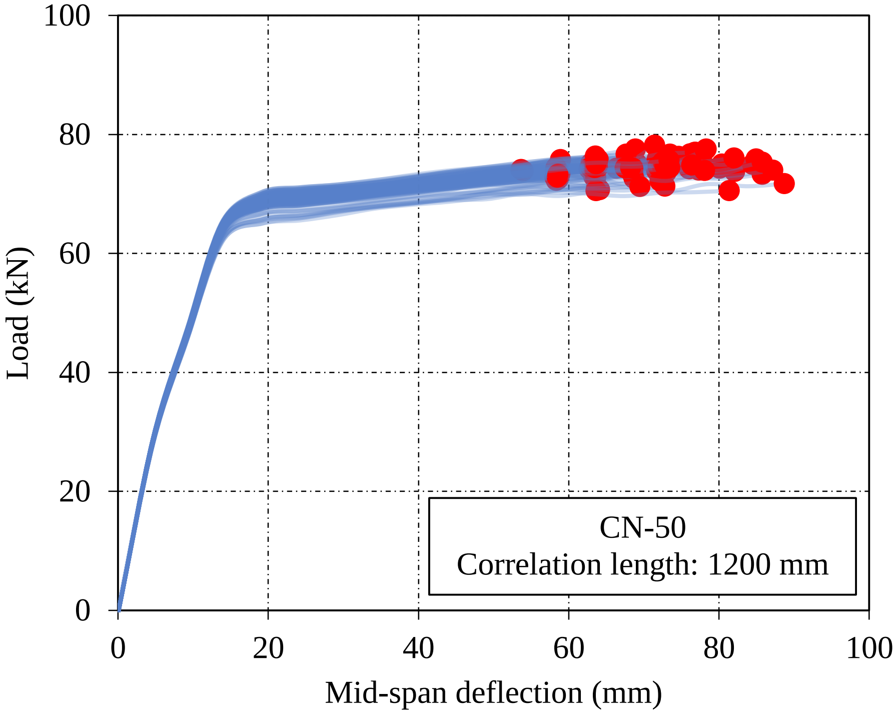
Load (kN)
Mid-span deflection (mm)
0
20
40
60
80
100
CN-50
Correlation length: 1200 mm

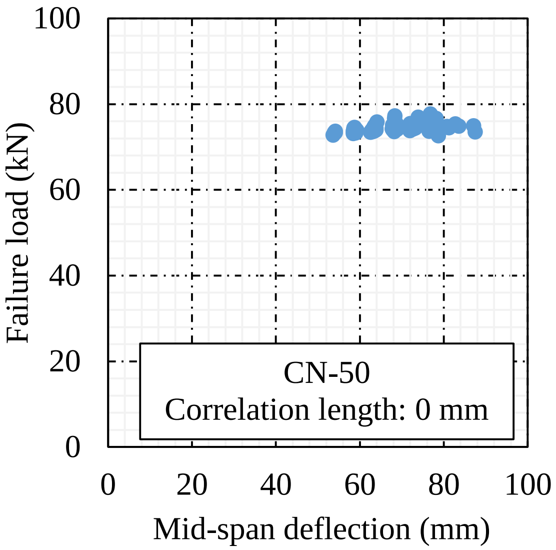
CN-50
Correlation length: 0 mm
Failure load (kN)
Mid-span deflection (mm)
0
20
40
60
80
100

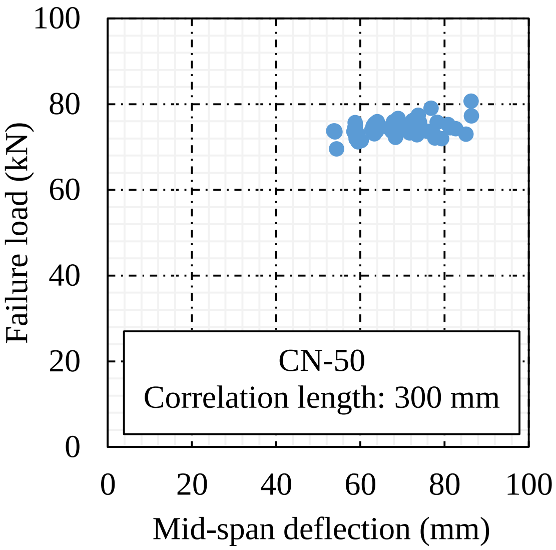
CN-50
Correlation length: 300 mm
Failure load (kN)
Mid-span deflection (mm)
0
20
40
60
80
100

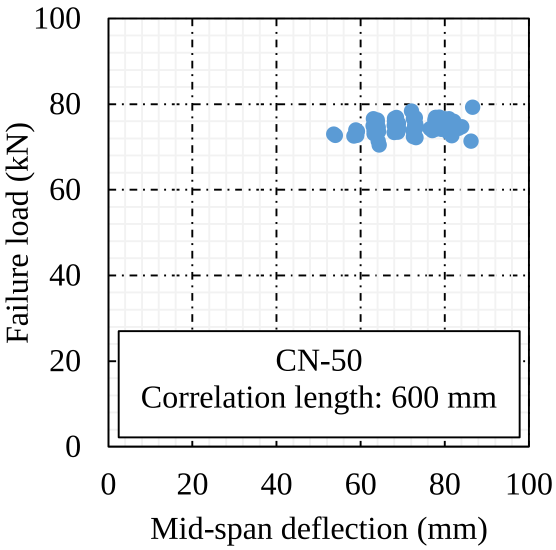
CN-50
Correlation length: 600 mm
Failure load (kN)
Mid-span deflection (mm)
0
20
40
60
80
100

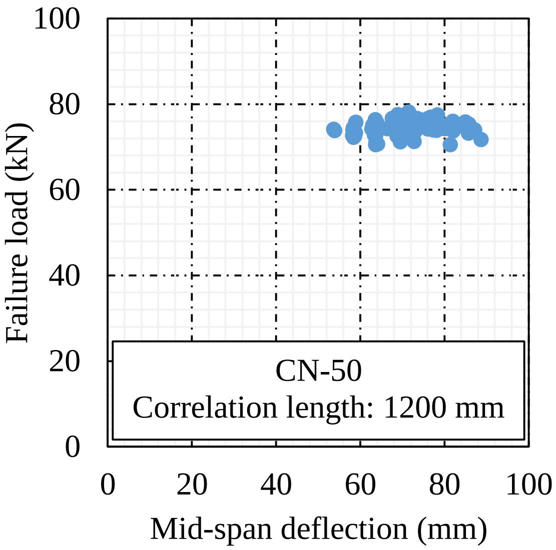
CN-50
Correlation length: 1200 mm
Failure load (kN)
Mid-span deflection (mm)
0
20
40
60
80
100

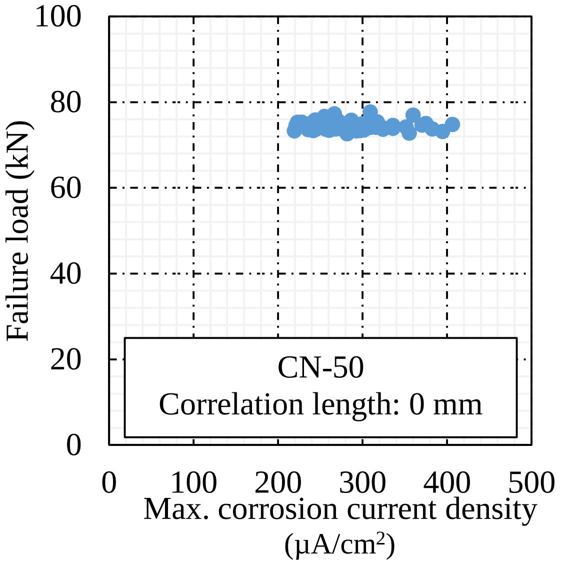
100
80
60
40
20
0
Failure load (kN)
0
100
200
300
400
500
Max. corrosion current density
(μA/cm²)
CN-50
Correlation length: 0 mm

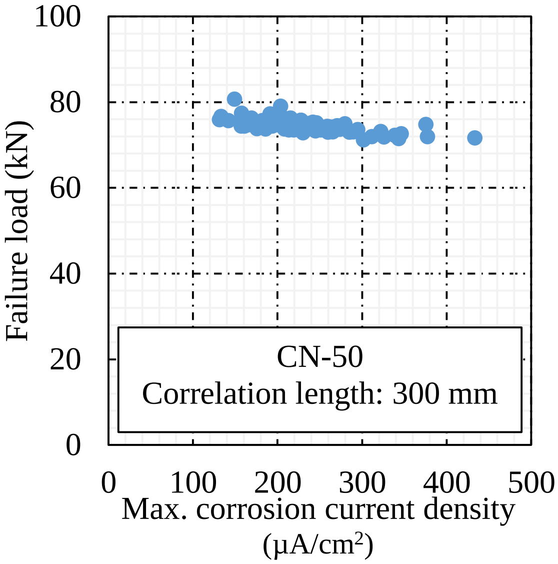
100
80
60
40
20
0
Failure load (kN)
0
100
200
300
400
500
Max. corrosion current density
(μA/cm²)
CN-50
Correlation length: 300 mm

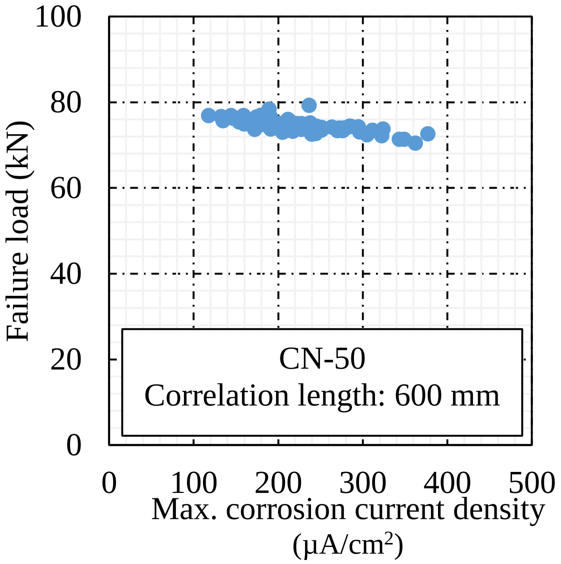
100
80
60
40
20
0
Failure load (kN)
0
100
200
300
400
500
Max. corrosion current density
(μA/cm²)
CN-50
Correlation length: 600 mm

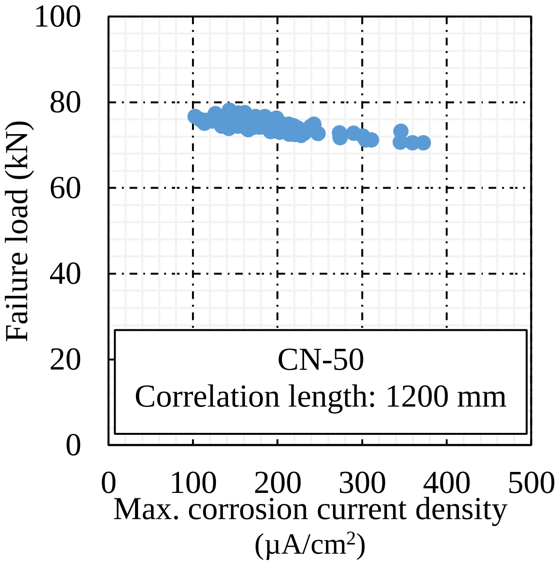
100
80
60
40
20
0
Failure load (kN)
0
100
200
300
400
500
Max. corrosion current density
(μA/cm²)
CN-50
Correlation length: 1200 mm

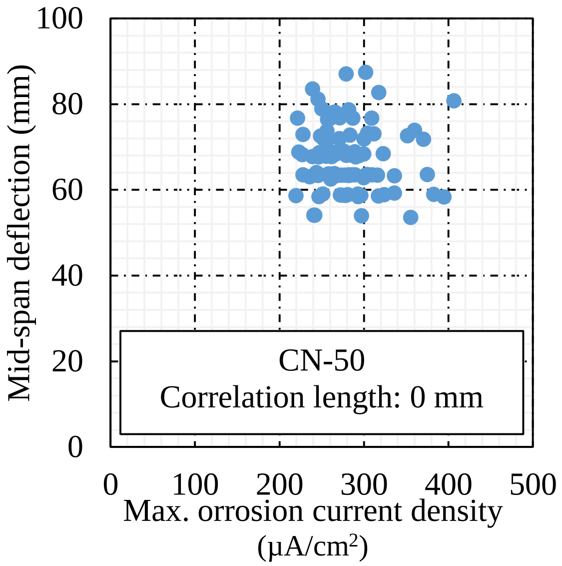
CN-50
Correlation length: 0 mm
Mid-span deflection (mm)
Max. orrosion current density
(μA/cm^2)
0
20
40
60
80
100
0
100
200
300
400
500

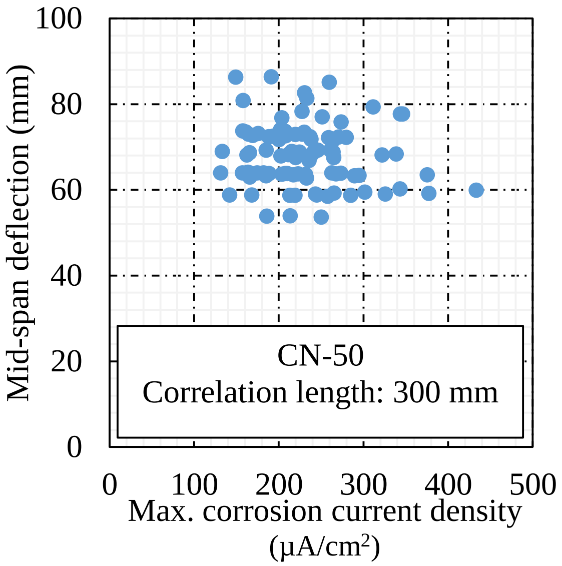
CN-50
Correlation length: 300 mm
Mid-span deflection (mm)
Max. corrosion current density
(μA/cm^2)
0
20
40
60
80
100
0
100
200
300
400
500

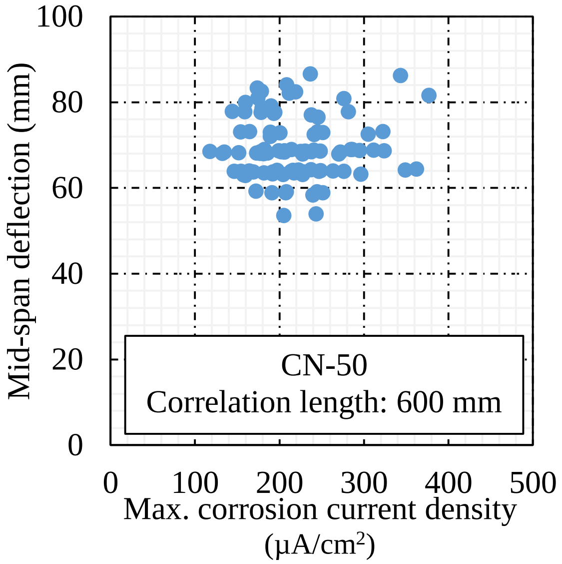
CN-50
Correlation length: 600 mm
Mid-span deflection (mm)
Max. corrosion current density
(μA/cm^2)
0
20
40
60
80
100
0
100
200
300
400
500

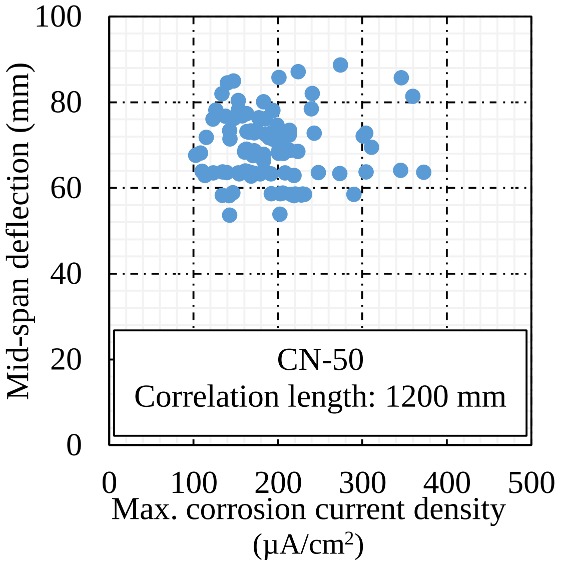
CN-50
Correlation length: 1200 mm
Mid-span deflection (mm)
Max. corrosion current density
(μA/cm^2)
0
20
40
60
80
100
0
100
200
300
400
500

B.3 Stochastic simulations of pitting corrosion

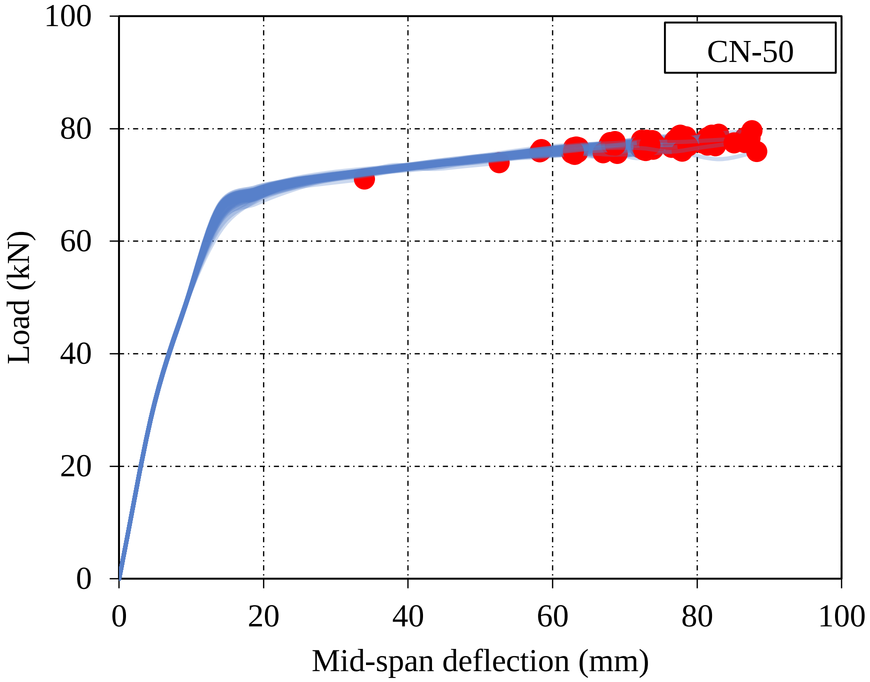

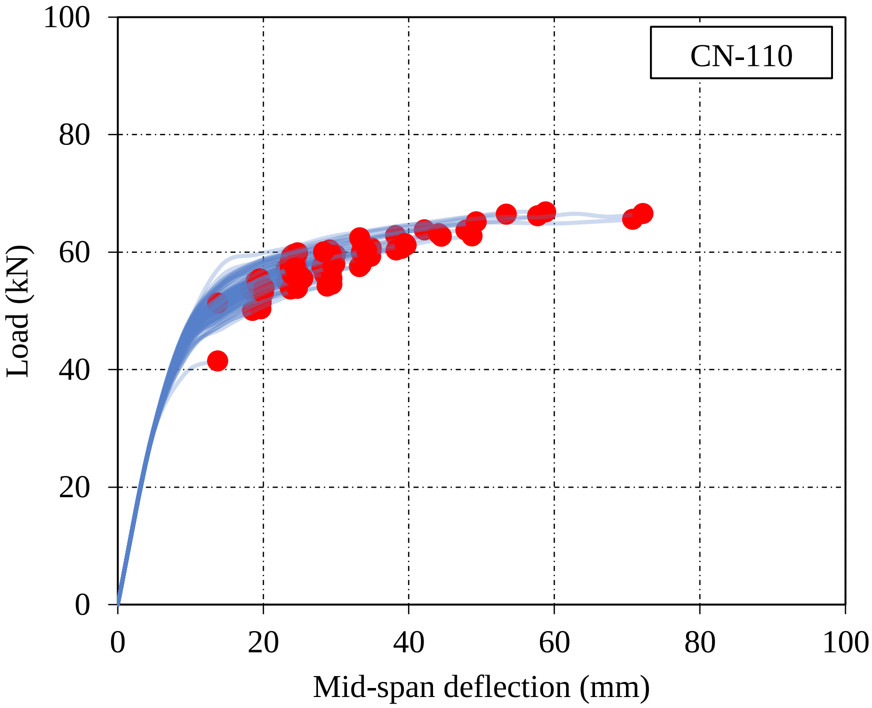

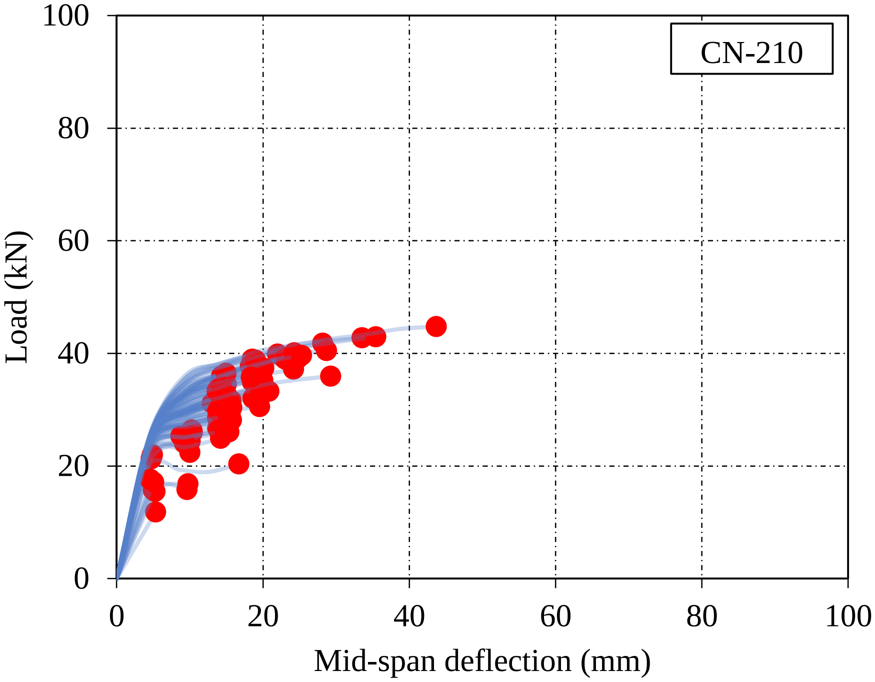
CN-210
Load (kN)
Mid-span deflection (mm)
0
20
40
60
80
100
0
20
40
60
80
100

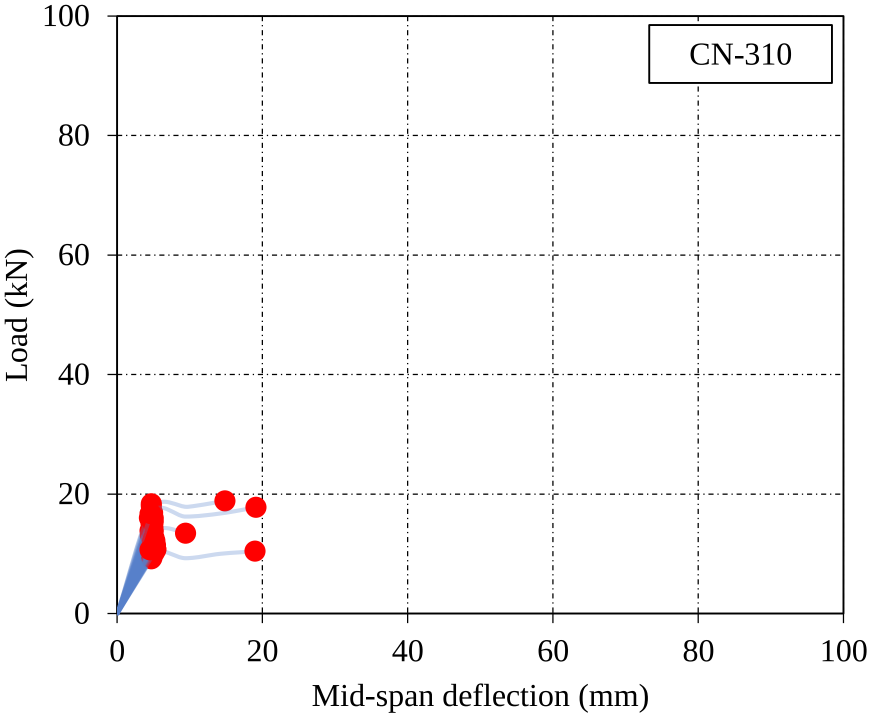
CN-310
Load (kN)
Mid-span deflection (mm)
0
20
40
60
80
100
0
20
40
60
80
100

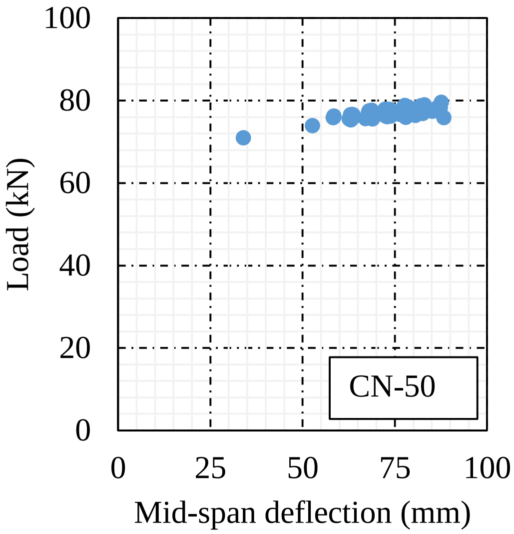
100
80
60
40
20
0
Load (kN)
0
25
50
75
100
Mid-span deflection (mm)
CN-50

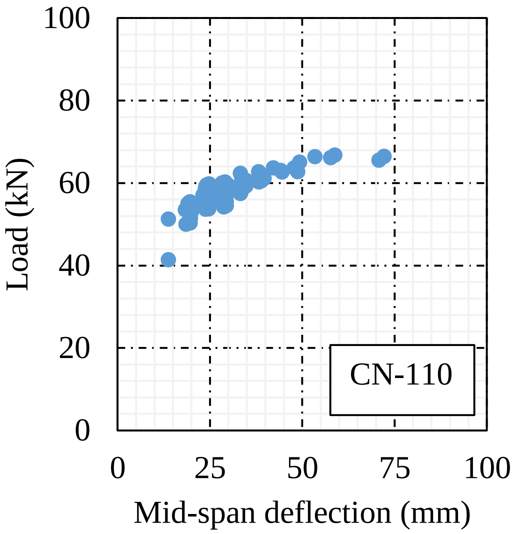
100
80
60
40
20
0
Load (kN)
0
25
50
75
100
Mid-span deflection (mm)
CN-110

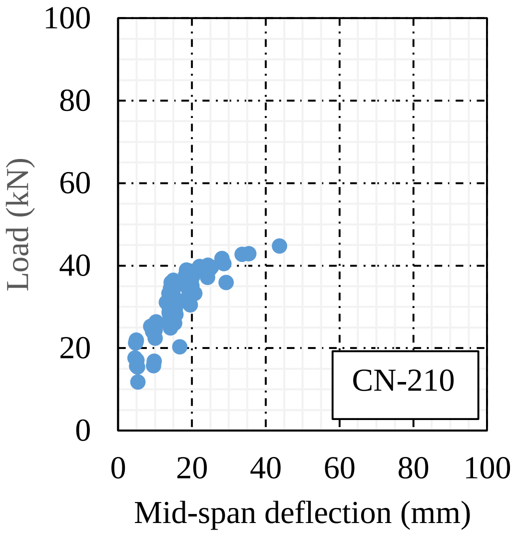
100
80
60
40
20
0
Load (kN)
0
20
40
60
80
100
Mid-span deflection (mm)
CN-210

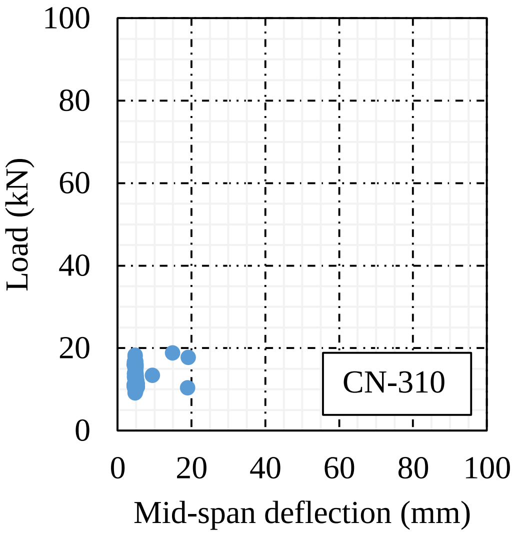
100
80
60
40
20
0
Load (kN)
0
20
40
60
80
100
Mid-span deflection (mm)
CN-310

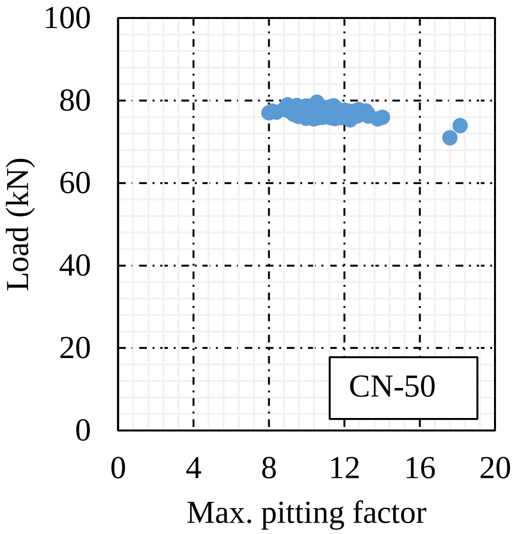
CN-50
Load (kN)
Max. pitting factor
0
20
40
60
80
100
0
4
8
12
16
20

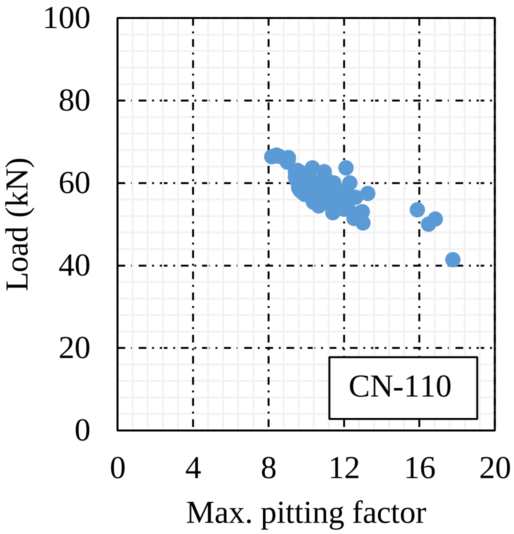
CN-110
Load (kN)
Max. pitting factor
0
20
40
60
80
100
0
4
8
12
16
20

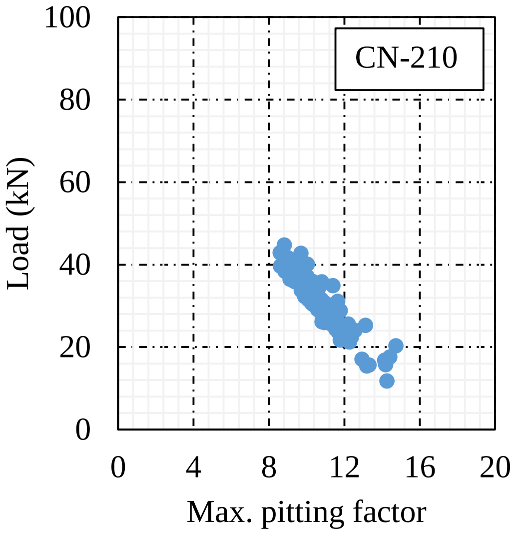
CN-210
Load (kN)
Max. pitting factor
0
20
40
60
80
100
0
4
8
12
16
20

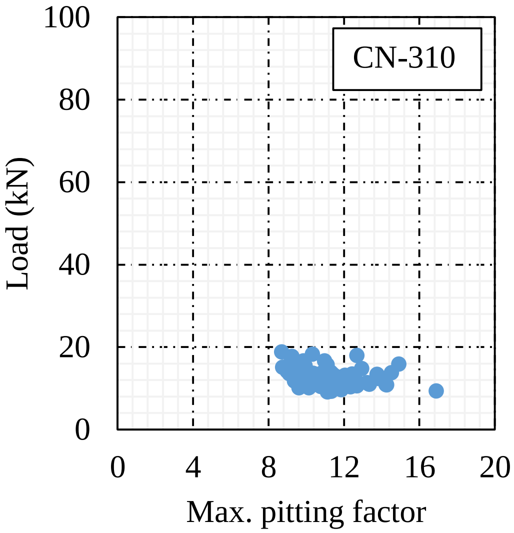
CN-310
Load (kN)
Max. pitting factor
0
20
40
60
80
100
0
4
8
12
16
20

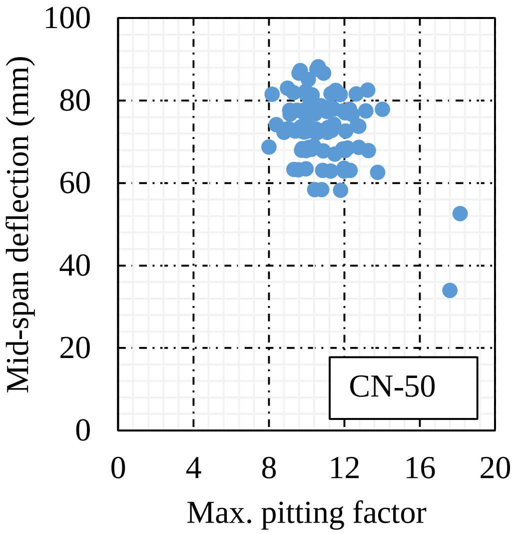
CN-50
Mid-span deflection (mm)
Max. pitting factor
0
20
40
60
80
100
0
4
8
12
16
20

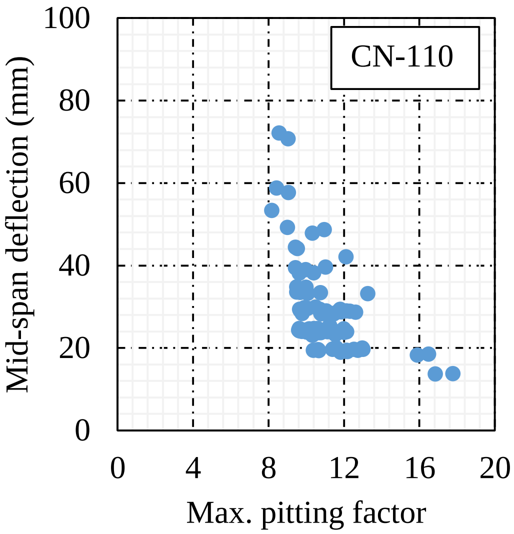
CN-110
Mid-span deflection (mm)
Max. pitting factor
0
20
40
60
80
100
0
4
8
12
16
20

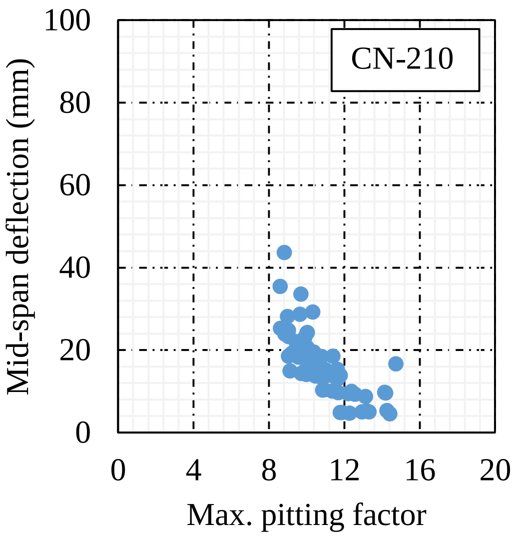
CN-210
Mid-span deflection (mm)
Max. pitting factor
0
20
40
60
80
100
0
4
8
12
16
20

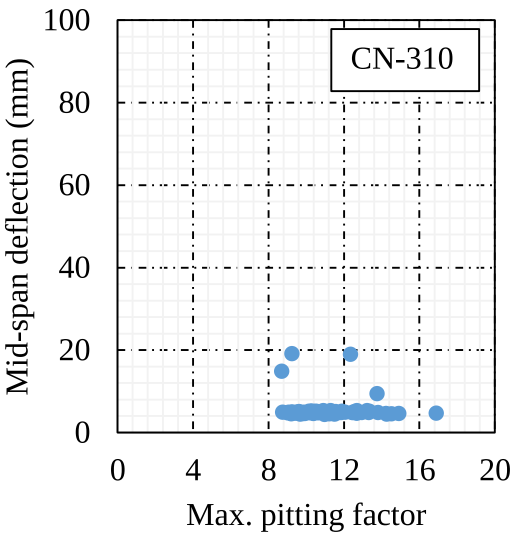
CN-310
Mid-span deflection (mm)
Max. pitting factor
0
20
40
60
80
100
0
4
8
12
16
20

Appendix C: User's Manual

This appendix can be used as a manual for users who want to model reinforced concrete members with corroded reinforcement in VecTor2. The current implementation includes two types of corrosion, namely uniform and pitting corrosion. For more information about the formulation of each type, the reader is referred to Chapter 3. In FormWorks, the pre-processor program of VecTor2, the options related to corrosion are found under *Define Job* menu in the *Special* tab. By default, corrosion is not considered in the analysis unless the user chooses a corrosion type from the drop down menu highlighted in Figure C.1. The corrosion types, listed in the drop down menu, are as follows:

1. Not Considered
2. Uniform
3. Pitting

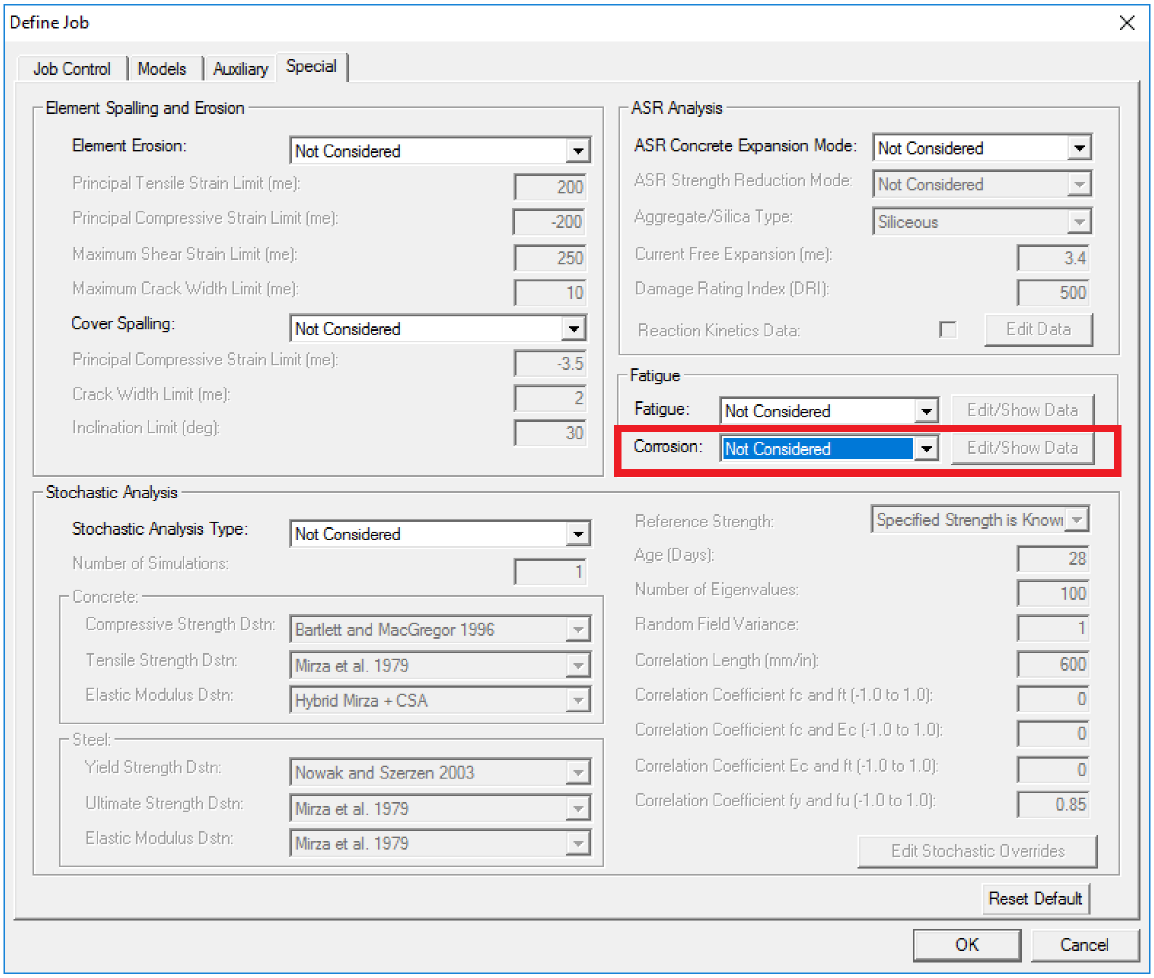

Element Erosion: Not Considered
Principal Tensile Strain Limit (me): 200
Principal Compressive Strain Limit (me): -200
Maximum Shear Strain Limit (me): 250
Maximum Crack Width Limit (me): 10
Cover Spalling: Not Considered
Principal Compressive Strain Limit (me): -3.5
Crack Width Limit (me): 2
Inclination Limit (deg): 30

ASR Concrete Expansion Mode: Not Considered
ASR Strength Reduction Mode: Not Considered
Aggregate/Silica Type: Siliceous
Current Free Expansion (me): 3.4
Damage Rating Index (DRI): 500
Reaction Kinetics Data: ☐

Fatigue: Not Considered
Corrosion: Not Considered

Stochastic Analysis Type: Not Considered
Number of Simulations: 1
Compressive Strength Dstn: Bartlett and MacGregor 1996
Tensile Strength Dstn: Mirza et al. 1979
Elastic Modulus Dstn: Hybrid Mirza + CSA
Yield Strength Dstn: Nowak and Szerzen 2003
Ultimate Strength Dstn: Mirza et al. 1979
Elastic Modulus Dstn: Mirza et al. 1979

Reference Strength: Specified Strength is Know
Age (Days): 28
Number of Eigenvalues: 100
Random Field Variance: 1
Correlation Length (mm/in): 600
Correlation Coefficient fc and ft (-1.0 to 1.0): 0
Correlation Coefficient fc and Ec (-1.0 to 1.0): 0
Correlation Coefficient Ec and ft (-1.0 to 1.0): 0
Correlation Coefficient fy and fu (-1.0 to 1.0): 0.85

Figure C.1: Corrosion analysis options in *Define Job* menu of FormWorks

In order to distinguish a normal (not corroded) reinforcing steel from corroded steel a new reinforcement material has been added to the material library of FormWorks. This material is named *Corroded Steel Reinforcement* and is found in the *Reference Type* drop down list of *Define Reinforcement Properties* menu of FormWorks, shown in Figure C.2. The constitutive model pertaining to the response of *Corroded Steel Reinforcement* is the same as *Ductile Steel Reinforcement*. For more information about the behavioural models for reinforcement materials, the reader is referred to ‘’VecTor2 & FormWorks User’s Manual’’ (Wong et al., 2013).

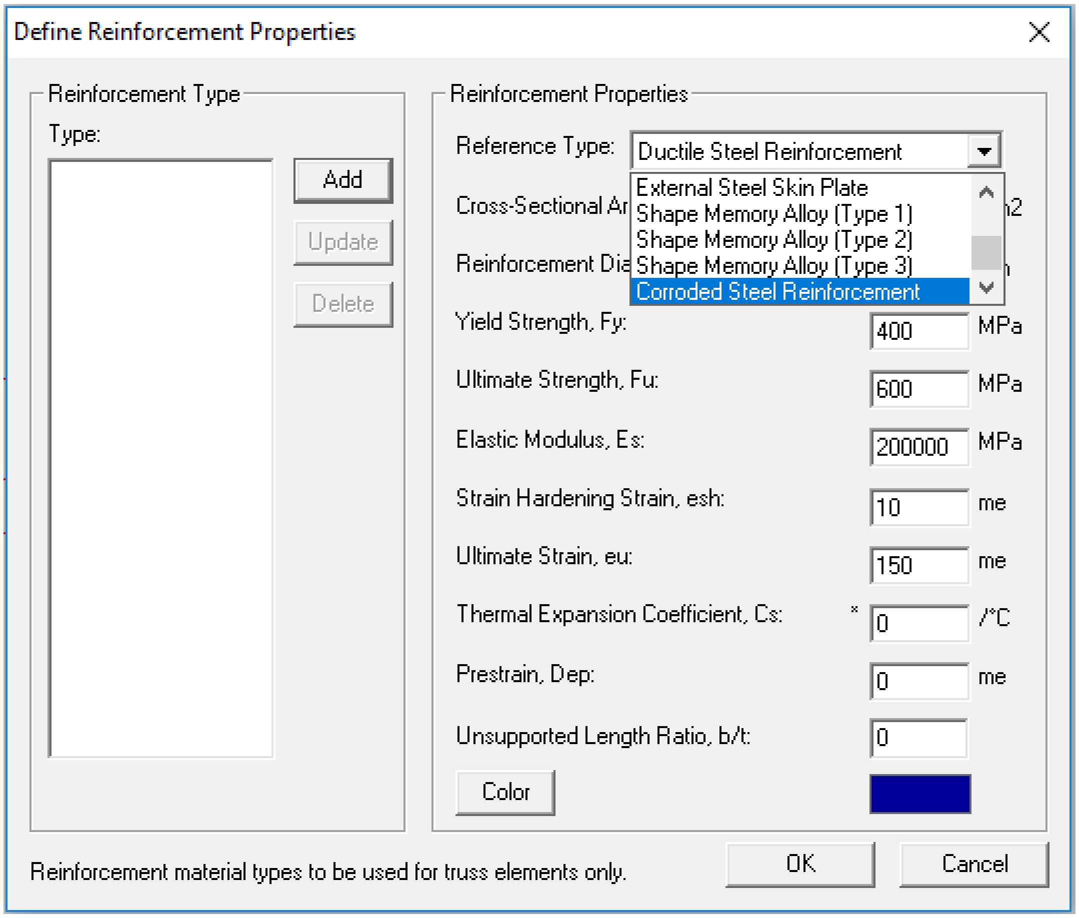

Reference Type: Ductile Steel Reinforcement

Yield Strength, Fy: 400 MPa

Ultimate Strength, Fu: 600 MPa

Elastic Modulus, Es: 200000 MPa

Strain Hardening Strain, esh: 10 me

Ultimate Strain, eu: 150 me

Thermal Expansion Coefficient, Cs: * 0 /°C

Prestrain, Dep: 0 me

Unsupported Length Ratio, b/t: 0

Reinforcement material types to be used for truss elements only.

Figure C.2: *Corroded Steel Reinforcement* material in FormWorks

The input parameters for uniform or pitting corrosion can be found in the *Corrosion Analysis Parameters* menu. This menu can be opened by clicking the *Edit/Show Data* button on the right hand side of *Corrosion* drop down list in the *Special* tab of the *Define Job* menu and is shown in Figure C.3. When *Corrosion Mode* is set to *Uniform*, the parameters *Corrosion Rate* and *Age* should be entered by the user. In this case, the *Cross-Sectional Area* and *Reinforcement Diameter* of truss elements which have the *Corroded Reinforcing Steel* as their material type will be modified based on the formulations presented in Section 3.1. Analogously, When *Corrosion Mode* is set to *Pitting*, the parameters *Corrosion Rate*, *Age*, and *Pitting Factor* should be entered by the user. In this case, in addition to *Cross-Sectional Area* and *Reinforcement Diameter*, the *Yield Strength*, *Ultimate Strength*, and *Ultimate Strain* of the corroded truss elements will also be modified according to the formulation given in Section 3.4. The user is also able to select a model for reduction of bond strength and cracking of the cover concrete from the drop down list related to each. It's recommended that for pitting corrosion, the bond strength and cover cracking be set to *Not Considered* as the type of rust produced as a result of pitting corrosion is less expansive than the product of uniform corrosion and severe cross-sectional loss can occur before any visible cracking signs. When cover cracking is to be modelled, *Expansion Ratio*, that is the ratio of the volume of unit mass of rust to that of iron, denoted by α_1 in Chapter 3, should be entered by the user. This value was given in Table 2.2 for the most common types of rust. A value of 3.75 (corresponding to iron hydroxide $Fe(OH)_2$) is recommended.

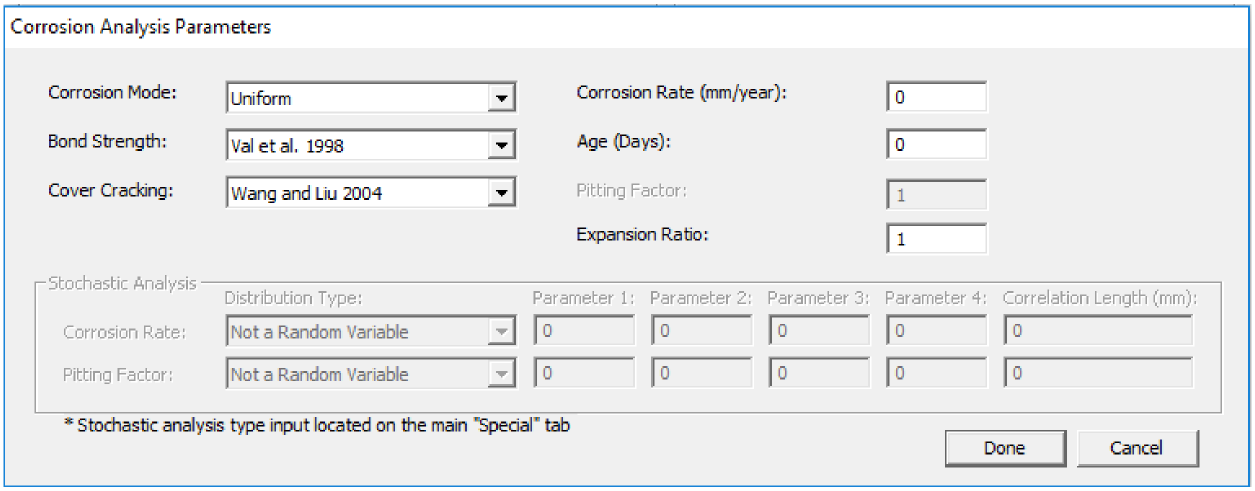

Corrosion Analysis Parameters

Corrosion Mode: Uniform
Bond Strength: Val et al. 1998
Cover Cracking: Wang and Liu 2004
Corrosion Rate (mm/year): 0
Age (Days): 0
Pitting Factor: 1
Expansion Ratio: 1

Stochastic Analysis

	Distribution Type:	Parameter 1:	Parameter 2:	Parameter 3:	Parameter 4:	Correlation Length (mm):
Corrosion Rate:	Not a Random Variable	0	0	0	0	0
Pitting Factor:	Not a Random Variable	0	0	0	0	0

* Stochastic analysis type input located on the main "Special" tab

Figure C.3: *Corrosion Analysis Parameters* menu

In order to perform stochastic simulation, a *Stochastic Analysis Type* from the *Define Job* menu in the *Special* tab should be chosen. For more information about the stochastic simulation tools available in VecTor2, the reader is referred to Hunter (2016). If the *Corrosion Mode* is set to *Uniform*, *Corrosion Rate* will be a random variable. On the other hand, if the *Corrosion Mode* is set to *Pitting*, the *Pitting Factor* will be a random variable and *Corrosion Rate* will have a constant value as entered by the user. The user can select one of the following options from the *Distribution Type* drop down menu for a random variable:

1. Not a random variable
2. Normal
3. Lognormal
4. Beta
5. Gamma
6. Gumbel

The parameters for each distribution type are summarized below.

Distribution Type	Parameter 1	Parameter 2	Parameter 3	Parameter 4
Normal	Mean	Standard Deviation	N/A	N/A
Lognormal	Mean	Standard Deviation	N/A	N/A
Beta	Shape (α)	Scale (β)	Lower Bound	Upper Bound
Gamma	Shape (α)	Scale (β)	N/A	N/A
Gumbel	Location (μ)	Scale (β)	N/A	N/A

Note that if the *Corrosion Rate* or *Pitting Factor* is modelled as a random variable, the mean value will be calculated based on the parameters of the chosen probability distribution. In the case of a random field simulation, a random value for the *Corrosion Rate* or *Pitting Factor* of each corroded truss element will be generated. Thus, in addition to the previous parameters, a *Correlation Length* for the corresponding random variable should be entered by the user. In the current implementation, an exponential autocorrelation function is used for populating the covariance matrix of the random fields.